UNIVERSITY OF BELGRADE

FACULTY OF PHYSICAL CHEMISTRY

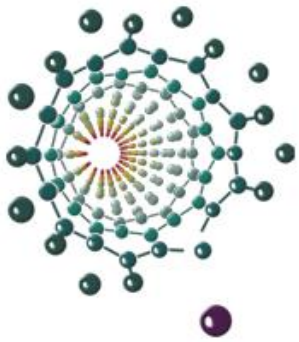

Vedran Milanković

NOVEL CARBON MATERIALS OBTAINED BY THERMOCHEMICAL CONVERSION OF BIOWASTE AS ADSORBENTS FOR THE REMOVAL OF MALATHION AND CHLORPYRIFOS FROM WATER

Doctoral Dissertation

Belgrade, 2024.

UNIVERZITET U BEOGRADU

FAKULTET ZA FIZIČKU HEMIJU

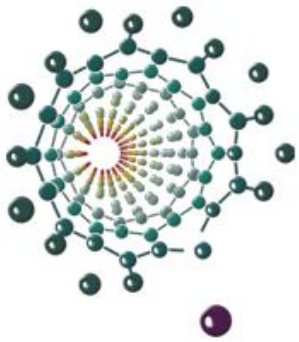

Vedran Milanković

NOVI UGLJENIČNI MATERIJALI DOBIJENI TERMOHEMIJSKOM KONVERZIJOM BIOOTPADA KAO ADSORBENSI ZA UKLANJANJE MALATIONA I HLORPIRIFOSA IZ VODE

doktorska disertacija

Beograd, 2024.

Mentors:

_____

1. **Dr. Igor Pašti, Full Professor,**
   University of Belgrade, Faculty of Physical Chemistry

_____

2. **Dr. Tamara Lazarević-Pašti, Full Research Professor,**
   University of Belgrade, Vinča Institute of Nuclear Sciences,
   National Institute of the Republic of Serbia

Committee members:

_____

1. **Dr. Maja Milojević-Rakić, Associate Professor,**
   University of Belgrade, Faculty of Physical Chemistry

_____

2. **Dr. Nemanja Gavrilov, Associate Professor**
   University of Belgrade, Faculty of Physical Chemistry

_____

3. **Dr. Snežana Brković, Research Associate,**
   University of Belgrade, Vinča Institute of Nuclear Sciences,
   National Institute of the Republic of Serbia

ZAHVALNICA

*Na samom početku, najdublju zahvalnost dugujem svojim dragim mentorima **prof. dr Igoru Paštiju**, redovnom profosoru Fakulteta za Fizičku hemiju, Univerziteta u Beogradu i **dr Tamari Lazarević-Pašti**, naučnom savetniku Instituta za nuklearne nauke „Vinča" – Instituta od nacionalnog značaja za Republiku Srbiju za uključenost i vođenje izrade mog diplomskog rada, master rada i ove doktorske disertacije. Посебно ценим вашу спремност да поделите своје богато искуство и дубоко разумевање научних проблема, као и вашу отвореност за дискусију и критичко разматрање мојих идеја. Без ваше подршке и менторства, мој академски пут не би био ни приближно успешан и испуњен као што је сада. Ваше знање, искуство и мудрост су ме не само обогатили као истраживача, већ су ми пружили и чврсте основе за даљи професионални развој. Хвала вам од срца за све што сте учинили за мене и за сваки тренутак који сте уложили у мој развој. Ваша преданост studentima i prijateljski stav je za mene inspiracija i težnju da i sam u budućnosti budem tako predan i nesebičan mentor.*

*Želio bih da se zahvalim prvoj osobi koja me uvela u problematiku aktivacije ugljeničnih materijala, **dr Danici Bajuk-Bogdanović**, naučnom savetniku Fakulteta za Fizičku hemiju, Univerziteta u Beogradu. Tokom moje treće godine osnovnih studija dr Bajuk-Bogdanović je bila moj mentor na studentskoj praksi u toku koje me naučila najvažnije o procesima aktivacije ugljeničnih materijala i gotovo sve što znam o spektroskopskim metodama. Takođe, želio bih da joj se zahvalim na snimanju ramanskog spektra prikazanog u ovoj disertaciji.*

*Ništa od ovoga ne bi bilo moguće da moja draga koleginica i drugarica, **Tamara Tasić**, nije bila uz mene. Zajedno smo uspješno vodili naše borbe sve do kraja i nadam se da ćemo tako i nastaviti.*

*Želim da se zahvalim **dr Snežani Brković**, naučnom saradniku Instituta za nuklearne nauke „Vinča" – Instituta od nacionalnog značaja za Republiku Srbiju, na svesrdnoj pomoći i uvođenju u problematiku sinteze ugljeničnih materijala termohemijskom konverzijom, kao i prijateljskim savetima i podršci.*

*Veliku zahvalnost dugujem **dr Nebojši Potkonjaku**, naučnom saradniku Instituta za nuklearne nauke „Vinča" – Instituta od nacionalnog značaja za Republiku Srbiju, na snimanju i pomoći prilikom tumačenja rezultata zeta potencijala.*

*Zahvaljujem se **dr Cristoph Unterweger**, Wood K plus – Kompetenzzentrum Holz GmbH, Linz, Austria, na određivanju specifične površine i zapremina pora sintetisanih namterijala BET analizom.*

***Dr Maji Milojević-Rakić** i **dr Nemanji Gavrilovu**, vanrednim profesorima Fakulteta za fizičku hemiju, Univerziteta u Beogradu, se zahvaljujem na upoznavanje sa principima zelene hemije, kao i interesovanju za ovu doktorsku disertaciju.*

Zahvaljujem se mojim prijateljima i porodici koji su mi pružili mnogo ljubavi i podrške, ne samo u toku izrade ove disertacije.

Ovu disertaciju posvećujem:

*Svojim roditeljima, **Dijani i Radoslavu**, koji su nesebično dali sve od sebe da bih ja imao mogućnost da bude ovde gdje sam sada, koji su vjerovali u mene, moje mogućnosti i znanje, bili uvijek uz mene i naučili me pravim ljudskim vrijednostima.*

*Svojoj sestri **Eni**, najboljem prijatelju kroz cijeli život, koja me je mnogo čemu naučila o životu, ali ono najbitnije, kako sve prebroditi i u svemu pronaći sreću.*

*Svojoj voljenoj, **Milici**, koja je prošla sa mnom svaki korak ovog fakulteta, od Opšteg kursa pa do sada, bila uz mene uz sve uspone i padove i voljela me.*

Hvala vam svima!

ABSTRACT

This doctoral dissertation investigates the potential of using thermochemical conversion and activation processes to address the environmental challenge posed by harmful food biowaste, specifically spent coffee grounds (SCG). With coffee being one of the most prevalent waste materials globally, its post-preparation residue, such as grounds, presents a significant environmental issue. This research aims to transform SCG into valuable adsorbents for the effective removal of organothiophosphorus pesticides, namely malathion (MLT) and chlorpyrifos (CHP), from water.

The study explores the influence of various thermochemical conversion temperatures (400°C, 650°C, 900°C) and activation methods (KOH, H_3PO_4, CO_2, KOH/CO_2, H_3PO4/CO_2) on the production of high-quality SCG adsorbents. These materials were characterized using techniques such as scanning electron microscopy (SEM), energy-dispersive X-ray spectroscopy (EDX), Fourier-transform infrared spectroscopy (FTIR), Brunauer-Emmett-Teller (BET) surface area analysis, Raman spectroscopy, Boehm titration, X-ray diffraction (XRD), and zeta potential measurements.

Results demonstrated that the thermochemical conversion and activation processes significantly influence the structural and chemical properties of SCG-derived adsorbents, thereby affecting their adsorption efficiency for MLT and CHP. Materials converted at higher temperatures and activated with KOH exhibited enhanced adsorption capacities and kinetics, driven by increased surface area, porosity, and the introduction of functional groups. The adsorption mechanisms, kinetics, and thermodynamics were thoroughly analyzed, revealing distinct behaviors for MLT and CHP influenced by their molecular structures.

The study further assesses the economic, environmental, and practical implications of SCG material production and application. The findings highlight the potential of SCG-based adsorbents as cost-effective, eco-friendly solutions for pesticide remediation, contributing to environmental sustainability by reducing biowaste and mitigating water pollution. This research provides valuable insights into optimizing synthesis parameters for developing effective adsorbents, emphasizing the transformative potential of SCG in addressing pressing environmental challenges.

This doctoral dissertation supports and advances the UN's sustainable development goals, in particular SDG 6 (Clean Water and Sanitation) by remediation of OPs, SDG 12 (Responsible consumption and production), and SDG 13 (Climate action) by using climate-harmful biowaste (SCG) in production of carbon materials.

Keywords: biowaste, spent coffee grounds carbon materials, organophosphorous pesticides, adsorption

Scientific field: Physical Chemistry

Specialized Scientific Fields: Physical Chemistry – Environmental Control and Protection, Physical Chemistry – Chemical Thermodynamics, Materials

UDC number:

SAŽETAK

Ova doktorska disertacija istražuje mogućnosti korišćenja termohemijske konverzije i aktivacionih procesa za rešavanje ekološkog izazova koji predstavlja štetni prehrambeni biootpad, konkretno iskorišteni taloge kafe (SCG). Kafa je jedan od najrasprostranjenijih otpadnih materijala širom sveta, a njeni ostaci nakon pripreme, poput taloga, predstavljaju značajan ekološki problem. Cilj istraživanja je transformacija SCG u vredne adsorbense koji mogu efikasno uklanjati organotiofosfatne pesticide, malation (MLT) i hlorpirifos (CHP), iz vode.

Istraživanja doktorske diseratcije obuhvataju uticaj različitih temperatura termohemijske konverzije (400°C, 650°C, 900°C) i metoda aktivacije (KOH, H_3PO_4, CO_2, KOH/CO_2, H_3PO_4/CO_2) na proizvodnju visokokvalitetnih adsorbenasa iz SCG. Dobijeni materijali su okarakterisani korišćenjem tehnika kao što su skenirajuća elektronska mikroskopija (SEM), energijski disperzivna rendgenska spektroskopija (EDX), infracrvena spektroskopija sa Furijeovom transformacijom (FTIR), Brunauer-Emmett-Teller (BET) analiza specifične površine i merenje zeta potencijala.

Nadalje, istraživanje uključuje mehanizme adsorpcije MLT i CHP na SCG materijalima kako bi se bolje razumeo način na koji ovi materijali interaguju sa zagađivačima. U početku, dobijeni materijali su testirani za remedijaciju MLT i CHP kroz skrining test, koji je poslužio kao osnova za dalja istraživanja. Materijali koji su pokazali veću efikasnost adsorpcije u poređenju sa SCG pod ekološki relevantnim uslovima su dalje detaljno ispitivani. Kinetičke studije su uključivale eksperimente adsorpcije oba pesticida na odabrane materijale, sa vremenom kontakta od 1 minuta do 24 sata, kako bi se odredilo vreme ravnoteže. Dobijeni podaci su analizirani korišćenjem kinetičkih modela kao što su pseudo-prvi red, pseudo-drugi red, Elovich i intračestični difuzioni model. Vreme ravnoteže određeno iz ovih studija korišćeno je kao vreme kontakta za dalja istraživanja adsorpcionog ponašanja. Izotermne studije su uključivale izvođenje eksperimenata adsorpcije oba pesticida pri koncentracijama u rasponu od 5×10^{-6} mol dm^{-3} do 5×10^{-4} mol dm^{-3} na tri različite temperature (25°C, 30°C, i 35°C). Podaci su evaluirani korištenjem četiri izotermna modela (Freundlich, Langmuir, Temkin i Dubinin-Radushkevich) kako bi se bolje razumeo adsorpcioni proces. Takođe, spontantnost i termalni efekti adsorpcionog procesa su procenjeni kroz termodinamičku analizu.

Najperspektivniji materijali su dodatno okarakterisani korišćenjem rendgenske difrakcione analize (XRD), Raman spektroskopije i Boehm titracije kako bi se dobio bolji uvid u njihovu strukturu i funkcionalne grupe. Opseg adsorpcionih eksperimenata je proširen variranjem koncentracija materijala, testiranjem adsorpcije pod dinamičkim uslovima i ispitivanjem adsorpcije pesticida iz njihovih smeša. Efekti remedijacije MLT i CHP korištenjem ovih materijala na inhibiciju acetilholinesteraze (AChE) testirani su korišćenjem modifikovanog Ellmanovog testa.

Rezultati istraživanja su pokazali da procesi termohemijske konverzije i aktivacije značajno utiču na strukturna i hemijska svojstva adsorbenasa dobijenih iz SCG, što utiče na njihovu efikasnost adsorpcije za MLT i CHP. Posebno, materijali termohemijski konvertovani na višim temperaturama i aktivirani sa KOH pokazali su poboljšane kapacitete adsorpcije i kinetičke parametre, što je rezultat povećane površine, poroznosti i prisustva funkcionalnih grupa. Mehanizmi adsorpcije, kinetika i termodinamika su detaljno analizirani, ukazujući na različita ponašanja za MLT i CHP, zbog razlike u njihovim molekulskim strukturama.

Ekonomski, ekološki i praktični aspekti proizvodnje i primene SCG materijala kao adsorbenasa za MLT i CHP su analizirani u ovoj doktorskoj disetaciji. Ovo uključuje procenu troškova proizvodnje, ekološki uticaj i praktičnu izvodljivost primene ovih materijala u različitim scenarijima remedijacije. Uticaj sinteze i primene ovih materijala na životnu sredinu je veoma pozitivan. Termohemijska konverzija SCG značajno smanjuje negativne ekološke efekte ovog biootpada. Iako proces sinteze nekih materijala uključuje upotrebu KOH, H_3PO_4 i CO_2, što blago umanjuje ekološke benefite valorizacije biootpada, to je nadoknađeno značajnim poboljšanjem adsorpcionih svojstava materijala. Ove hemikalije poboljšavaju efikasnost materijala, osiguravajući adsorpciju i uklanjanje veće količine zagađivača. Sinteza i primena ovih materijala ne samo da efikasno rešava problem biootpadom, već igra ključnu ulogu u remedijaciji životne sredine. Ova dvostruka funkcija naglašava njihov veliki pozitivan uticaj na životnu sredinu. Procenjivanje praktičnosti primene različitih adsorbenasa za uklanjanje MLT i CHP iz vodenih rastvora je obuhvatalo evaluaciju ključnih parametra: cena sinteze po gramu, specifična površina, ukupna zapremina pora, površinsko naelektrisanje na pH=6, vreme postizanja ravnoteže, adsorpcioni kapacitet i energija adsorpcije. Među testiranim materijalima, materijali dobijeni termohemijskom konverzijom na 900°C pokazuju najbolje performanse, ali su i najskuplji. Uprkos visokoj ceni, superiorne performanse čine ih idealnim za primene koje zahtevaju maksimalnu efikasnost. Sa druge strane, materijali dobijeni termohemijskom konverzijom SCG na 400°C pokazuju nešto slabije adsorpcione performanse (duže vreme dostizanja ravnoteže i manji maksimalan adsorpcioni kapacitet), ali su znatno jednostavniji i jeftiniji za proizvodnju, čineći iz povoljnim za upotrebu u remedijaciji pesticida u stacionarnim uslovima.

Ova doktorska disertacija podržava i unapređuje ciljeve održivog razvoja Ujedinjenih nacija, posebno SDG 6 (Clean Water and Sanitation) kroz remedijaciju organo-tiofosfatnih pesticida, SDG 12 (Responsible consumption and production) i SDG 13 (Climate action) korišćenjem klimatski štetnog biootpada, SCG, u proizvodnji ugljeničnih materijala.

Rezultati istraživanja ističu potencijal adsorbenasa dobijenih termohemijskom konverzijom SCG kao ekonomičnih, ekološki prihvatljivih rešenja za remedijaciju pesticida, doprinoseći ekološkoj održivosti smanjenjem biootpada i zagađenja vode. Disertacija pruža uvid u optimizaciju parametara sinteze za razvoj efikasnih adsorbenasa, naglašavajući potencijal konverzije SCG u borbi protiv ekoloških izazova.

Ključne reči: biootpad, iskorišteni talog kafe, organo-tiofosfatni pesticidi, adsorpcija

Naučna oblast: Fizička hemija

Uže naučne oblasti: Fizička hemija – kontrola i zaštita životne sredine, Fizička hemija – hemijska termodinamika, materijali

UDK broj:

TABLE OF CONTENT

1. INTRODUCTION

Biowaste poses a significant challenge globally, driven by its environmental, health, and economic impacts [1]. It comprises organic waste material from food processing, preparation, and consumption, including agricultural by-products and kitchen scraps. Food biowaste is a significant contributor to this problem. As biowaste decomposes, it releases greenhouse gases like CO_2, impacting climate change. Economically, food biowaste represents a loss of valuable food resources, highlighting inefficiencies in resource use that could otherwise support broader societal needs [2, 3].

Pesticides are crucial tools in the fight against food biowaste. They play a critical role in preventing crop loss due to pests and diseases, thereby reducing the volume of food discarded due to damage or spoilage [4]. By enhancing the efficiency of food production, pesticides contribute significantly to minimizing biowaste at the agricultural level, supporting a more sustainable agricultural system [5].

Among the various forms of food biowaste, spent coffee grounds (SCG) present a unique challenge due to their volume and treatment difficulties. Annually, the world produces approximately 10.5 million metric tons of coffee, primarily in countries like Brazil and Vietnam, leading to substantial quantities of SCG [6]. If not managed properly, these by-products can cause severe environmental issues, including air, water, and land pollution. The release of nitrogen and carbon dioxide from SCG contributes to smog, ozone formation, and climate change, underscoring the need for their proper management [7].

Effectively addressing biowaste involves innovative recycling technologies, such as converting biowaste like SCG into high-value products. Thermochemical conversion processes can transform biowaste into activated carbon and biochar [8]. Their additional chemical, physical, and physicochemical activation can enhance surface area and porosity, making them suitable for a range of environmental applications, including water purification [9].

While pesticides are beneficial for reducing crop loss and biowaste, their extensive and improper use and disposal bring significant environmental and health risks. Pesticides like organophosphorus compounds (OPs), such as malathion and chlorpyrifos, are highly toxic and persistent in environments. Traditional water treatment methods struggle with these contaminants, facing issues like high costs, complexity, and the potential to produce more toxic products [10].

The innovative use of biowaste-derived carbon materials does not only race the issue of biowaste accumulation but also addresses the pollution caused by harmful pesticides. These carbon materials have been shown to effectively adsorb toxic OPs from water, demonstrating high adsorption capacities and efficient kinetics [11]. This dual approach—recycling biowaste into functional carbon adsorbents and removing hazardous pollutants from water—illustrates a holistic strategy toward environmental sustainability. It uses the basic properties of biowaste-derived carbons to develop a cost-effective and eco-friendly approach to water purification, therefore addressing the urgent global need for safe water resources and contributing to a circular economy [12].

This doctoral dissertation supports and advances the UN's sustainable development goals, in particular SDG 6 (Clean Water and Sanitation) by remediation of OPs, SDG 12 (Responsible consumption and production), and SDG 13 (Climate action) by using climate-harmful biowaste (SCG) in production of carbon materials [13].

2. THEORETICAL FOUNDATIONS

2.1. The emerging problem of food biowaste

Biowaste is a growing global issue that needs to be addressed, and action must be taken to reduce its environmental, health, and economic impacts. Food biowaste is the organic waste derived from food processing, preparation, and serving activities, including agricultural by-products and food scraps [1]. These materials are all organic, meaning they release carbon dioxide and other greenhouse gases when broken down. In addition to the environmental impacts, food biowaste has an economic impact on the global food system, as it represents an avoidable waste of necessary food resources [2].

One of the largest contributors to food biowaste is from farms and other food production sites, with the majority of it being agricultural residues, such as crop residues, stalks, and husks, and post-harvest food waste, such as damaged fruit and vegetables [14]. Processing plants are also major contributors to food biowaste, originating from losses due to contamination, over-processing, or other production issues. Lastly, food leftovers from restaurants, schools, grocery stores, and households are also major biowaste sources [15].

To effectively reduce the impact of food biowaste, the primary focus needs to be on preventing it in the first place. This means implementing measures to reduce food waste at all stages of the global food system, from farm to fork. Unfortunately, this is a complicated and multifaceted problem that requires cooperation from many different actors.

Improved soil and water management are crucial to reducing food waste for farms and other food production sites [16]. Additionally, the use of pesticides significantly reduces biowaste by effectively controlling pests and diseases that damage crops. When crops are protected from insects, weeds, and fungi, the amount of food lost before it even reaches consumers is drastically decreased. This means that a more significant portion of the harvest is marketable, reducing the need to discard damaged or infested produce. Pesticides minimize post-harvest losses by ensuring healthier and more abundant yields, contributing to less biowaste. Reducing crop loss helps optimize resource use and supports a more sustainable food supply chain [4, 5].

At the processing level, enhancing automation and utilizing advanced technology can significantly reduce food biowaste caused by contamination and over-processing [17]. Additionally, improving storage and transportation systems can minimize food biowaste generated during these stages. Finally, to effectively reduce food biowaste, consumers and food establishments must adopt better practices in purchasing, storing, and preparing food and proper biowaste management programs [18].

Using biowaste materials in environmental protection offers a sustainable solution to managing waste while benefiting the ecosystem [19]. Various treatment processes can convert biowaste into valuable products like biochar, compost, and biogas. These products can help improve environmental health, reduce pollution through adsorption, reduce the need for chemical fertilizers, and generate renewable energy, thereby decreasing greenhouse gas emissions. Moreover, repurposing biowaste resolves the environmental problem of waste disposal and promotes a circular economy by turning waste into resources [20].

Spent coffee grounds (SCG) are the by-product of the production and consumption of coffee, and they are increasingly being recognized as valuable biowaste materials as they are renewable, cost-effective, and safe and can be used in various applications. According to the latest research, approximately 10.5 million metric tons of coffee are produced yearly in about 50 countries, with most of the supply coming from Brazil and Vietnam. The emerging issue of SCG lies in the increasing volume of waste generated and the challenges associated with its disposal. As coffee consumption continues to rise globally, so does the accumulation of SCG, posing environmental and logistical concerns [6].

SCG can have a very negative effect on the environment if disposed of improperly. The three main types of environmental damage caused by coffee grounds are air pollution, water pollution, and land pollution [7]. When exposed to the environment, coffee grounds release two main chemicals into the atmosphere: nitrogen and carbon dioxide. Nitrogen reacts with oxygen to form smog and ozone, both detrimental to the environment. Carbon dioxide is a greenhouse gas, meaning that it traps heat in the atmosphere and leads to climate change. This can lead to issues such as higher temperatures, drought, floods, and species extinctions. When exposed to water, coffee grounds can cause several types of water pollution. They introduce chemicals into water sources, increase the water's acidity level, and can lead to a decrease in oxygenation. These factors can lead to increased algae growth and bacteria, harming aquatic species and leading to water-borne diseases in humans. SCG can also affect the land. They are composed of organic and inorganic compounds, which, when exposed to the environment, can potentially attract pests such as rats and cockroaches. They also contain biodegradable materials, which can disturb the natural growth of plants [21].

To reduce the environmental impact of coffee grounds, they should be composted, reused, or recycled. With the proper disposal methods, it is possible to minimize the environmental harm. SCG can serve as a precursor material for the production of biochar [22, 23]. This is attributed to several properties of SCG, including its porosity, surface area, and rich composition of organic compounds such as cellulose, lignin, and carbohydrates. These characteristics make SCG an excellent candidate for synthesizing adsorbents that are capable of effectively capturing and removing pollutants from various aqueous environments [24]. Furthermore, its abundance and availability as a biowaste product make it a sustainable and cost-effective precursor for adsorbent synthesis. By repurposing SCG into adsorbents, environmental pollutants can be mitigated, and the burden of waste disposal can be reduced, contributing to the principles of circular economy and waste valorization [25].

Overall, the use of SCG as a precursor for adsorbents holds significant promise for environmental remediation. It offers a sustainable and efficient solution for removing pollutants from water resources while resolving the problem of biowaste accumulation.

2.2. Thermochemical conversion and biochar activation methods

2.2.1. Thermochemical conversion

Thermochemical treatment of biowaste involves subjecting organic waste materials to high temperatures in the absence or presence of oxygen, inducing various chemical reactions. This treatment encompasses several techniques, including combustion, pyrolysis, torrefaction, carbonization, gasification, and hydrothermal carbonization, each with distinct objectives and outcomes [26, 27].

Direct biomass combustion occurs at approximately 800°C in the presence of air, either without prior treatment or after forming pellets or briquettes. This process produces hot gases commonly used for heating. Combustion can be complete or incomplete. Complete combustion entirely consumes all fuel components, while incomplete combustion leaves behind unburned fuel or gases due to insufficient oxygen or poor fuel-air mixing [28].

Pyrolysis heats biomass rapidly, breaking organic materials into volatile compounds, gases (such as methane, carbon monoxide, and hydrogen), tar, and biochar. The absence of oxygen prevents complete combustion, allowing the biomass to decompose into valuable products like biochar, which can be used as a soil amendment or for other applications. Low-temperature pyrolysis (300°C to 500°C) primarily produces biochar, with smaller amounts of bio-oil and gas, often used in slow pyrolysis to maximize biochar production for soil improvement and carbon sequestration. Medium-temperature pyrolysis (500°C to 800°C) balances the fast conversion rates of high-temperature pyrolysis and the biochar-focused approach of low-temperature pyrolysis, producing a mixture of biochar, bio-oil, and gas. High-temperature pyrolysis (above 800°C) results in greater thermal decomposition, converting organic compounds into gases such as hydrogen, methane, and carbon monoxide, and is considered promising for converting biomass into biofuels and biochar with high energy efficiency and minimal environmental impact [29].

Though not strictly a form of pyrolysis, torrefaction can be viewed as a low-temperature variant. It occurs at 200 to 300°C under near or atmospheric pressure, without oxygen, with low heating rates. The biomass partially decomposes, releasing CO_2 and CO, but retains most of its hydrogen, as the temperature is too low to release C_xH_y compounds. Torrefaction is commonly used as a pre-treatment method for biomass, ensuring complete drying and degrading of fibrous structures [30].

Carbonization is a slow pyrolysis process converting biomass into a highly carbonaceous, charcoal-like material. During carbonization, complex carbon substances degrade due to heating in an inert atmosphere, eliminating substituent atoms and groups from the organic molecules of the initial materials, resulting in a product with high carbon content. Inert gases, such as nitrogen or argon, are used to remove oxygen [31]. Carbonization, similar to natural coalification but much faster, occurs at high temperatures (up to or above 1000°C) over hours, while coalification takes thousands of years at low temperatures. The main product is activated carbon, which has significantly higher carbon content and aromaticity than the starting precursor. Its characteristics depend on reaction conditions and the raw material used [32].

Gasification converts biomass into a combustible gas mixture called syngas or producer gas under a controlled amount of oxygen and/or steam. Syngas can generate electricity directly in gas engines or turbines or be transformed into liquid fuels or chemicals through further processing. Gasification is noted for its efficiency and ability to process diverse biomass materials [33].

Hydrothermal carbonization involves heating a biomass and water suspension in a sealed reactor (autoclave) at elevated temperatures (180-280°C) and autogenous pressure for several hours. The process converts up to 90% of carbon from plant waste into a solid carbonaceous material called hydrochar without releasing CO_2 or CH_4 into the atmosphere. For this reason, it is considered a promising future technology for converting waste biomass into a coal-like product for a wide range of environmental, electrochemical, catalytic, and other applications [34].

Thermochemical conversion processes can be optimized based on the type of biomass, desired products, and available technology. The choice of process impacts the biomass conversion system's efficiency, environmental footprint, and economic viability. Each method has its challenges and benefits, and choosing a technique is crucial depending on the specific application and desired end products. Thermochemically obtained biochar can be physically and chemically activated to enhance its specific surface area and porosity, enhancing its adsorption or catalytic properties [9].

2.2.2. Physical activation

Physical activation of biochar is a critical process in enhancing its properties for use as an adsorbent or catalyst. This process involves treating biochar with gases, typically at high temperatures, to increase its surface area and develop a porous structure that is more effective for adsorption [35].

After thermochemical conversion, the biochar is exposed to oxidizing agents at high temperatures. Typical gases used for this process include steam and CO_2. This step is critical as it burns off tarry residues and other volatile components, leaving a highly porous structure behind [36].

The activation process is fundamentally aimed at developing the biochar's internal porosity and creating an extensive network of pores within the biochar, which can trap chemical pollutants, heavy metals, or other substances in environmental cleanup applications. The choice of gas and the conditions under which activation occurs determine the nature of the pores formed (micropores, mesopores, or macropores) [36].

The activation temperature is crucial in determining the quality and type of pores developed. Higher temperatures typically enhance the development of a more porous structure. The duration of activation also affects the extent of the development of porosity. Longer activation times allow for more extensive development of the internal structure. The choice between steam, CO_2, or a mix affects the properties of the activated biochar. Steam activation is particularly effective for creating a high volume of micropores [37].

CO_2 is the most commonly used as an activator in this process. When it diffuses into the pores and adsorbs onto the active sites of biochar, it induces partial gasification, enhancing the biochar's porosity. The activation mechanism can be described as follows:

$$C_{biochar} + CO_2 \rightarrow 2CO \qquad \text{Eq. 1}$$

This reaction occurs at high temperatures, typically between 600 and 900°C, where CO_2 reacts with the carbon atoms on the biochar's surface, leading to the formation and expansion of micropores and mesopores, thus significantly improving the biochar's adsorption properties [37].

2.2.3. Chemical activation

Chemical activation of biochar is a process that enhances the adsorptive properties of the material, making it more effective for various applications, particularly in environmental remediation and energy storage. This process involves treating biomass with chemical agents before or during carbonization at high temperatures. The chemical agents not only develop the biochar's internal pore structure but also introduce functional groups that can provide specific chemical properties. Various chemical agents have been employed as activators in the chemical activation process [38]. These activators can be categorized into four types based on the acid-base theory and activation mechanism: alkaline, acidic, neutral, and self-activating agents. These activators interact with cellulose, hemicellulose, lignin, or polysaccharides in the carbon precursor, resulting in diverse activation mechanisms. KOH and H_3PO_4 stand out as commonly studied and utilized among these agents due to their effectiveness and extensively researched and demonstrated to produce activated carbon materials with desirable properties for various applications. KOH and H_3PO_4 offer advantages such as availability, cost-effectiveness, and the ability to generate specific types of pores. Consequently, they are often preferred choices in many studies and industrial applications [39, 40].

Although KOH activation is a widely used method for producing activated carbons due to its effectiveness in generating porosity and increasing the specific surface area, the exact mechanism still needs to be fully understood. This complexity arises mainly from the significant influence of experimental parameters and the varying reactivity of different precursors. The proposed mechanism of activation is as follows [41]:

At around 400 °C, KOH undergoes dehydration to form K_2O:

$$2KOH \rightarrow K_2O + H_2O \quad \text{Eq. 2}$$

This is followed by the water-gas reaction, where carbon reacts with H_2O to produce CO and H_2:

$$C + H_2O \rightarrow CO + H_2 \quad \text{Eq. 3}$$

Subsequently, the CO generated in this reaction participates in the water-gas-shift reaction:

$$CO + H_2O \rightarrow CO_2 + H_2 \quad \text{Eq. 4}$$

K_2CO_3 is produced from the reaction between CO_2 and K_2O formed in the initial dehydration step,

$$CO_2 + K_2O \rightarrow K_2CO_3 \quad \text{Eq. 5}$$

and, finally, metallic K is formed:

$$K_2CO_3 + C \rightarrow 2K + 3CO \quad \text{Eq. 6}$$

Metallic K can enter the inner structure of the carbon lattice, making the aromatic layers expand and distort the carbon layers, resulting in new pores. It also changes how electrons are distributed around carbon atoms in the aromatic layer, creating more active sites for reactions. Additionally, it improves how wet the carbon surface is and reduces surface tension, making it easier to form pores [42].

The activation mechanism and the transformations undergone by H_3PO_4 at specific temperature ranges are detailed through equations below [42]:

$$2H_3PO_4 \rightarrow H_4P_2O_7 + H_2O \quad \text{Eq. 7}$$

$$3H_3PO_4 \rightarrow H_5P_3O_{10} + 2H_2O \quad \text{Eq. 8}$$

$$nH_3PO_4 \rightarrow H_{n+2}P_nO_{3n+1} + (n-1)H_2O \quad \text{Eq. 9}$$

During this phase, adsorbed water is released, and phosphoric acid becomes anhydrous. Consequently, the breakdown of functional groups yields CO_2 and CO.

At temperatures ranging from 400 to 700 °C:

$$H_{n+2}P_nO_{3n+1} \rightarrow P_4O_{10} + H_2O \quad \text{Eq. 10}$$

$$P_4O_{10} + 2C \rightarrow P_4O_6 + 2CO_2 \quad \text{Eq. 11}$$

Here, the dehydration of phosphoric acid leads to the release of water. Subsequently, P_4O_{10}, serving as a potent oxidant, reacts with carbon, creating new and expanding existing pores while producing CO_2. Additionally, the breakdown of surface functional groups generates carbon monoxide.

At temperatures ranging from 700 to 800 °C:

$$P_4O_{10} \text{ or } P_4O_6 + CH_x \rightarrow PH_3 + CO_2 \text{ or } CO \quad \text{Eq. 12}$$

This equation illustrates the formation of PH_3 along with CO_2 and CO as byproducts of reactions and the disintegration of functional groups. Consequently, the resulting reaction products facilitate the surface's pore formation and expansion [43].

2.2.4. Physicochemical activation

Physicochemical activation is a process that enhances the properties of materials, particularly in the production of activated carbons and other porous substances, by combining physical and chemical methods [44].

Physical activation involves treating carbon-rich precursors, such as biomass or coal, with oxidizing gases like steam or carbon dioxide at high temperatures, creating a highly porous structure by selectively burning away portions of the material. Chemical activation, on the other hand, involves impregnating the precursor with chemical agents, such as KOH or H_3PO_4, followed by thermochemical conversion, which promotes pore formation through dehydration and structural breakdown.

This dual approach combines the benefits of both techniques to achieve materials with superior surface areas, tailored porosity, and enhanced chemical functionalities. Due to their optimized structural and chemical characteristics, the resultant materials are highly effective for applications in adsorption, catalysis, energy storage, and environmental remediation [44].

2.3. Organophosphorous pesticides

Pesticides are commonly used for pest control and can be classified in various ways, often based on their chemical structure. Well-known groups include organochlorines, organophosphorus compounds, carbamates, pyrethroids, amides, anilines, and nitrogenous heterocyclic compounds. Among these, organophosphorous pesticides (OPs) are notable for their toxic effects and widespread use [45].

The general structure of OPs is given in Figure 1. R_1 and R_2 are aryl or alkyl groups attached to the phosphorus atom either directly, forming phosphinates, or through an oxygen or sulfur atom, forming phosphates or phosphothioates. In some instances, R_1 is directly bonded to the phosphorus atom, while R_2 is connected via an oxygen or sulfur atom, creating phosphonates or thiophosphonates. For phosphoramidates, at least one of these groups is $–NH_2$ (which can be unsubstituted, mono-substituted, or bi-substituted), and the atom double-bonded to phosphorus can be either oxygen or sulfur. The –X group, which also binds to the phosphorus atom through an oxygen or sulfur atom, can be a halogen, aliphatic, aromatic, or heterocyclic group. This "leaving group" detaches from the phosphorus atom when phosphotriesterases interact with protein targets to hydrolyze the organophosphorus compound [46].

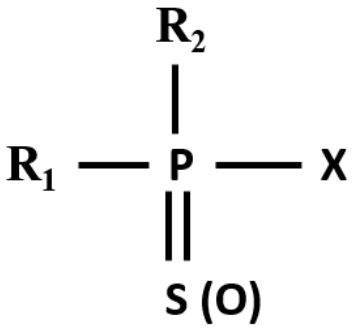

Figure 1. General structure of organophosphate pesticides

OPs are extensively used in agricultural, commercial, and residential settings, making exposure common for the general population. OPs can be absorbed through inhalation, ingestion, and dermal contact. These compounds are toxic to humans and most animals because they inhibit the enzyme acetylcholinesterase (AChE). Since AChE is responsible for terminating impulse transmission by rapidly hydrolyzing the neurotransmitter acetylcholine, its inhibition results in the accumulation of acetylcholine. This leads to the hyperstimulation of nicotinic and muscarinic receptors, disrupting normal neurotransmission [47]. Their toxicity extends beyond the immediate acute phase, with chronic effects being well-documented. Prolonged or repeated exposure to OPs can result in the same adverse effects as acute exposure, including delayed symptoms. Workers who are repeatedly exposed to OPs have reported a range of symptoms such as impaired memory and concentration, disorientation, severe depression, irritability, confusion, headaches, speech difficulties, delayed reaction times, nightmares, sleepwalking, drowsiness, and insomnia. An influenza-like condition characterized by headaches, nausea, weakness, loss of appetite, and malaise has also been observed [48].

The most commonly used OPs include malathion, parathion, chlorpyrifos, diazinon, dimethoate, and phorate [49].

2.3.1. Malathion

Malathion (O,O-dimethyl-S-(1,2-dicarbethoxyethyl) phosphorodithioate; MLT) is an organophosphate insecticide with the molecular formula $C_{10}H_{19}O_6PS_2$ and a molar mass of 330.36 g mol^{-1}. It appears as a yellow-to-brown liquid with a characteristic odor and a density of 1.23 g cm^{-3} at 25 °C. MLT is soluble in alcohol, benzene, and acetone but only slightly soluble in water [50]. The structural formula of MLT is shown in Figure 2.

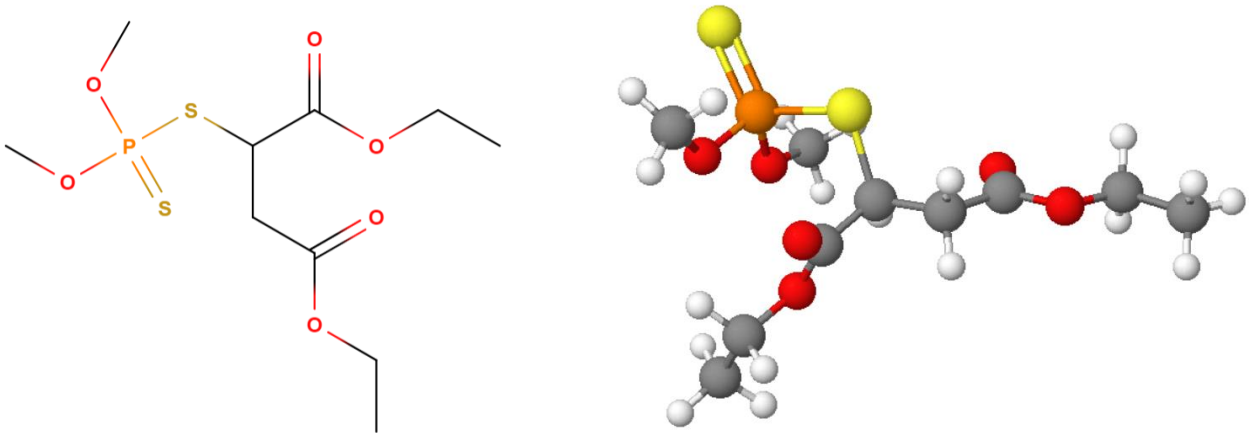

Figure 2. Structure of malathion

MLT is classified as a moderately toxic pesticide. Public health pest control programs often use it to eliminate mosquitoes and other insects. It can be biotransformed into its more toxic form, malaoxon. Malaoxon exhibits toxicity that is significantly higher than that of MLT. The lethal dose (LD50) for MLT in rats is approximately 1000 mg kg^{-1} [51].

It is widely employed as an insecticide, acaricide, and pediculicide. In agriculture, it controls various pests on fruits, vegetables, and ornamental plants. It is also used in public health programs for mosquito control and in veterinary medicine to manage ectoparasites on livestock. Similar to other OPs, MLT exerts its insecticidal activity by inhibiting the enzyme AChE, leading to the accumulation of the neurotransmitter acetylcholine at nerve endings [52].

Although effective in pest control, malathion poses health risks to humans and animals. Its toxicity is associated with various neurological, respiratory, and reproductive problems following exposure. MLT exposure can cause acute symptoms such as headaches, dizziness, and nausea, as well as chronic effects, including endocrine disruption and immunotoxicity [53]. Studies have shown that continuous exposure to this OP can lead to elevated levels of specific antibodies, indicative of autoimmune responses [54].

2.3.2. Chlorpyrifos

Chlorpyrifos (O,O-diethyl-O-(3,5,6-trichloro-2-pyridyl) phosphorothioate; CHP) is an organophosphate insecticide with the molecular formula $C_9H_{11}Cl_3NO_3PS$ and a molar mass of 350.59 g mol^{-1}. It appears as colorless crystals with a density of 1.39 g cm^{-3} at 43.5 °C and is generally soluble in ethanol, methanol, xylene, and benzene [55]. The structural formula of CHP is shown in Figure 3.

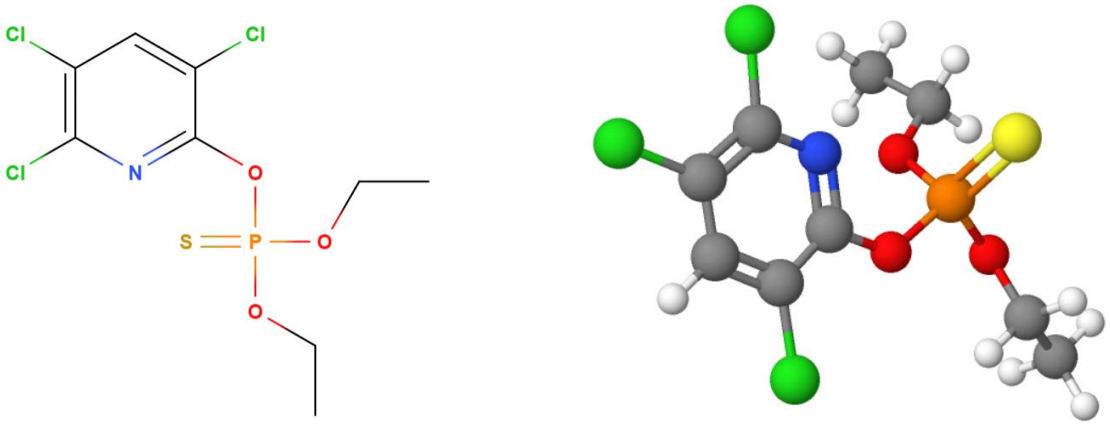

Figure 3. Structure of chlorpyrifos

CHP is classified as a highly toxic pesticide. It can be biotransformed into its oxo form, chlorpyrifos-oxon, via cytochrome P450 monooxygenase in the liver. Chlorpyrifos-oxon is up to 180 times more toxic than chlorpyrifos itself. The lethal dose that causes death in 50% of tested rats (LD50) is 95-270 mg/kg [56].

It is widely used as a potent insecticide, nematicide, and acaricide. In households, it is employed to control pests like cockroaches, fleas, and termites. On farms, it protects cattle from ticks and is used as a spray to control pests attacking crops [57]. Like other organophosphates, it exhibits its insecticidal activity by inhibiting the enzyme AChE, resulting in the accumulation of the neurotransmitter acetylcholine at nerve endings [58].

Although highly effective in pest control and crop growth promotion, CHP poses risks to human and animal health due to its toxicity, which is linked to various psychological, endocrine, hematological, respiratory, and reproductive problems following exposure. Harmful effects on humans include neurological impacts on fetuses and children at very low exposure levels, as well as acute poisoning from high exposure. Research on individuals continuously exposed to chlorpyrifos indicates elevated levels of specific antibodies characteristic of autoimmune diseases. There is a strong association between chronic illnesses related to autoimmune disorders and chlorpyrifos exposure [59, 60].

2.3.3. Organothiophosphorous pesticides' remediation

While effective in pest management, OPs pose significant risks to human health and the environment due to their toxicity and persistence. Therefore, developing methods to remove OP residues from water sources is crucial for mitigating these risks. Several techniques for removing OPs from water have been developed, including degradation, microbiological, and adsorption methods.

Degradation methods involve breaking down OP molecules into non-toxic byproducts through oxidation, photochemistry, and electrochemistry processes. Enhanced oxidation processes, like the Fenton reaction, have shown promise in efficiently degrading OPs in water [61, 62].

Microbiological methods utilize microorganisms like bacteria to metabolize OPs, converting them into harmless substances. These cost-effective and environmentally friendly methods make them attractive for remediation efforts [63, 64].

Adsorption methods rely on materials with high surface area and porosity, such as activated carbon and clay, to adsorb OP molecules from water physically. Carbon-based materials, especially biomass-derived, have shown particular effectiveness in adsorbing OPs due to their strong affinity for organic compounds [65, 66].

While degradation methods and microbiological approaches offer promising avenues for removing OPs from water, they also have drawbacks. Degradation methods may produce toxic byproducts, and microbiological approaches can be slow and require specific environmental conditions. In contrast, adsorption methods present several advantages, including simplicity, cost-effectiveness, and high efficiency in removing OP residues from water. Therefore, adsorption stands out as the method of choice for OP removal, offering a reliable and environmentally friendly solution to mitigate the risks associated with OP contamination in water sources [67].

Efforts are underway to optimize these removal methods to enhance their efficiency and applicability across various water sources contaminated with OP residues. We can minimize the health and environmental risks associated with these hazardous compounds by implementing effective OP removal strategies.

2.4. Theoretical aspects of adsorption

2.4.1. Adsorption on a solid surface

Adsorption is a process defined as the increase in concentration of one or more chemical species (atoms, molecules, or ions) at the interface between two phases, most commonly solid and liquid or gas. Adsorption occurs due to the attractive forces of surface atoms, molecules, or ions of the solid phase, which are unbalanced and strive to achieve equilibrium by attracting and retaining components from the adjacent phase with which they are in contact. This leads to a reduction in the free energy of the surface of the solid phase. The component that accumulates on the solid phase is called the adsorbate, while the surface on which the adsorption occurs is called the adsorbent. Adsorption can be interpreted through a series of steps: transport of the adsorbate through the solution, diffusion of the adsorbate across the liquid film surrounding the adsorbent particles, diffusion of the adsorbate to and through the pores of the adsorbent (intraparticle diffusion), and finally, adsorption and desorption of the adsorbate on the adsorbent surface [68].

Adsorption can be categorized into two types based on the nature of the bond between the adsorbate and the adsorbent: physical adsorption (physisorption) and chemical adsorption (chemisorption). In the case of physisorption, the adsorbate is bound to the surface of the solid adsorbent by weak Van der Waals forces (dispersive or dipolar). Conversely, chemisorption involves stronger chemical bonds, such as covalent bonds. Besides the nature of the bonding, physisorption, and chemisorption differ in their adsorption enthalpies, temperatures at which the adsorption process occurs, reversibility, and dependence on the characteristics of the adsorbent and adsorbate (specific surface area of the adsorbent). In many instances, adsorption exhibits mixed characteristics, partly physisorption and partly chemisorption [68, 69].

Weak Van der Waals forces characterize physisorption, which typically occurs at lower temperatures and decreases with temperature rise. It involves low adsorption enthalpy and is reversible, with adsorption increasing with pressure. Conversely, chemisorption involves strong chemical bonds, often forming a monolayer on the adsorbent's surface. It occurs at higher temperatures and increases with temperature rise, with higher adsorption enthalpies and generally irreversible processes. Chemisorption depends on the characteristics of both the adsorbate and the adsorbent and may require activation energy [68, 70].

Kinetics, isotherm, and thermodynamic behavior must be investigated to fully describe the adsorption process.

2.4.2. Adsorption kinetics

Adsorption in porous adsorbents takes time to reach equilibrium due to mass transfer resistance. The process involves: external mass transfer across the boundary layer or diffusion film between the liquid phase and the adsorbent's surface; diffusion within the adsorbent particles, allowing the adsorbate to enter the pores; and the formation of physical or chemical bonds at the active sites within the adsorbent's pores. The slowest step dictates the adsorption rate, which may depend on either film or intraparticle diffusion [71].

Kinetic adsorption curves (q_t=f(t)) are analyzed to monitor adsorbate concentration changes over time, helping to identify the controlling kinetic mechanism. Models such as the pseudo-first-order, pseudo-second-order kinetics, Elovich, and intraparticle diffusion model are often used to describe the adsorption kinetics of organic compounds [72].

The Lagergren pseudo-first-order (PFO) model assumes that the rate of adsorbate uptake over time is directly proportional to the difference between the saturation concentration and the amount of adsorbate adsorbed over time. This model is generally applicable during the initial stage of the adsorption process. It is often observed that adsorption kinetics follow this PFO equation when the process involves diffusion through the interface. The equation representing this model is:

$$q_t = q_e(1 - e^{-k_1 t}) \quad \text{Eq. 13}$$

, where q_t is the amount of adsorbate at the time (mg g^{-1}), q_e is the equilibrium adsorption capacity (mg g^{-1}), and k_1 is the rate constant of PFO (min^{-1}).

The pseudo-second-order (PSO) kinetic model extends this analysis to systems involving the assumption that the adsorption rate is dependent on concentrations of both adsorbate and adsorbent. The equation representing this model is:

$$q_t = \frac{q_e^2 k_2 t}{1 + q_e k_2 t} \quad \text{Eq. 14}$$

, where k_2 is the adsorption rate of PSO (g mg^{-1} min^{-1})

The Elovich kinetic model is an empirical model frequently used to analyze adsorption kinetics and effectively describes second-order kinetics based on the assumption that the surface has energetic heterogeneity. The equation representing this model is:

$$q_t = \frac{1}{\beta}(1 + \alpha\beta t) \quad \text{Eq. 15}$$

, where α is the initial adsorption rate (mg g^{-1} min^{-1}), and β is the desorption constant (g mg^{-1}).

The intraparticle diffusion (IPD) kinetic model is fundamental for understanding the adsorption process within porous materials. It provides insights into how adsorbate molecules diffuse into the interior of adsorbent particles and interact with the surface sites. By considering diffusion mechanisms such as pore diffusion and surface diffusion, this model clarifies the rates at which adsorption occurs within the particle. The equation representing this model is:

$$q_t = k_{id} t^{0.5} + C \quad \text{Eq. 16}$$

, where k_{id} is the adsorption rate constant of the IPD model (mg g^{-1} $min^{-0.5}$), C is a boundary layer (mg g^{-1}) [72].

2.4.3. Adsorption isotherms

An adsorption isotherm ($q_e=f(C_e)$; T=const.) represents the relationship between the concentration of adsorbate on the surface of the adsorbent (q_e (mg g^{-1})) and the equilibrium concentration of adsorbate in the solution (C_e (mg dm^{-3})) at a constant temperature and under given conditions.

Adsorption isotherms provide insights into the mechanisms of adsorption and help estimate adsorption capacity. Numerous theoretical and empirical isotherm models have been developed. The most frequently used isotherm models for the description of adsorption are the Freundlich, Langmuir, Temkin, and Dubinin-Radushkevich isotherm models [73].

The Freundlich adsorption isotherm (Eq. 17) describes the relationship between the adsorbed amount of a substance and the equilibrium pressure or concentration of the adsorbate. The equation is used to model the relationship between adsorption and the available surface area of materials. Freundlich isotherm model states that adsorption increases exponentially with equilibrium concentration until the adsorption sites have all been saturated and the concentration of the adsorbent has been maximized. Freundlich's isotherm model predicts adsorption on an energetically heterogeneous surface, and adsorbed molecules interact with each other. If the value n > 1, adsorption is favored; if n<1, it is not favored; and if n=1, adsorption follows a linear function. K_F is the Freundlich adsorption coefficient ((mg g^{-1})(dm^3 g^{-1})$^{1/n}$), representing the quantity of adsorbate adsorbed onto the adsorbent for a unit concentration of adsorbate in solution. It provides a measure of how well the adsorbent can adsorb the adsorbate at lower concentrations [73].

$$q_e = K_F C_e^{\frac{1}{n}} \qquad \text{Eq. 17}$$

The Langmuir adsorption isotherm (Eq. 18) describes the relationship between the adsorbed amount of a substance and the equilibrium concentration of the adsorbate. This equation is used to model the adsorption process and to quantify the adsorption potential of a substance. The Langmuir isotherm states that adsorption increases linearly with equilibrium pressure until the adsorption sites have been saturated and the adsorption capacity of the material has been reached. Langumir's isotherm model proposes that adsorbate molecules are adsorbed on an energetically homogenous surface without the interaction between adsorbed molecules. It indicates that all active sites are energetically equivalent and that adsorption is reached when a monolayer is formed. K_L (dm^3 mg^{-1}) value indicates the affinity of the adsorbate molecules towards the adsorbent, and q_{max} (mg g^{-1}) value implies the maximum adsorption capacity of the monolayer [73].

$$q_e = \frac{q_{max} K_L C_e}{1 + K_L C_e} \qquad \text{Eq. 18}$$

The Temkin isotherm model (Eq. 19) assumes that the adsorption heat of all molecules decreases linearly with the increase in coverage of the adsorbent surface and that adsorption is characterized by a uniform distribution of binding energies up to a maximum binding energy. This isotherm model includes Temkin's isotherm constant b_T (J g mol^{-1} mg^{-1}) which is related to the adsorption energy of the system. The higher the adsorption energy, the higher the b_T value, and the more readily adsorbed the material is onto the surface of the solid. K_T (dm^3 mg^{-1}) reflects the equilibrium binding constant, indicating the affinity of the adsorbate towards the adsorbent [73].

$$q_e = \frac{RT}{b_T} \ln K_T C_e \qquad \text{Eq. 19}$$

The Dubinin-Radushkevich adsorption isotherm (Eq. 20) is an empirical adsorption isotherm model used to describe the relationship between adsorptive material and equilibrium adsorption pressure. It accounts for adsorption in both open and closed environments and for systems in which non-ideality of the adsorptive media is present. This isotherm gives the parameters q_{DR}, which is a theoretical isotherm saturation capacity (mg g^{-1}), and $K_{DR,}$ which is the Dubinin-Radushkevich isotherm constant (mol^2 J^{-2}). Polanyi potential (ε=RTln(1+1/Ce)) helps to describe the energy involved in the adsorption process [73].

$$q_e = q_{DR} e^{-K_{DR}\varepsilon^2} \quad \text{Eq. 20}$$

Adsorption mean free energy E (J mol^{-1}) can be calculated from the Dubinin-Radushkevich adsorption isotherm model using the following equation:

$$E = \frac{1}{\sqrt{2K_{DR}}} \quad \text{Eq. 21}$$

If the value of E > 8000 J mol^{-1}, the preferred adsorption mechanism is chemisorption, and if E< 8000 J $mol^{-1,}$ physisorption is the probable process of adsorption [73, 74].

2.4.4. Thermodynamics of adsorption

The thermodynamics of adsorption studies the thermal processes, including changes in enthalpy(ΔH), entropy(ΔS), and Gibbs free energy (ΔG) during the interaction between the adsorbate and the adsorbent. Thermodynamic parameters provide insights into the nature of adsorption and the spontaneity of the process. If $\Delta H>0$, the process is endothermic, while if $\Delta H<0$, the process is exothermic. If ΔS is negative, the randomness of the system decreases, and if it is positive, the randomness of the system increases after the interaction. ΔG is linked with the spontaneity of the process; if $\Delta G<0$, the process is spontaneous, while if $\Delta G>0$, the process is not likely to happen [75].

The thermodynamic parameters of the adsorption process can be calculated using experimental data obtained at different temperatures with the following equations:

$$\ln K_{dist}^0 = -\frac{\Delta H^0}{RT} + \frac{\Delta S^0}{R} \quad \text{Eq. 22}$$

$$K_{dist}^0 = \frac{q_e}{C_e} \times \frac{C^0}{q^0} \quad \text{Eq. 23}$$

The values of ΔH^0 and ΔS^0 can be determined as the intercept and the slope of the plot of Van't Hoff equation, respectively (Eq. 22), where $\Delta G^0 = -RT\ln K_{dist}^0$. The standard distribution coefficient was calculated using equation (Eq. 23). To make it dimensionless, $\frac{q_e}{C_e}$ is multiplied with C^0 and q^0 values, which represent the standard state for the contaminant in the solution (1 mol dm^{-3}) and in the adsorbed state (1 mol kg^{-1}). Gibbs free energy was then calculated using the Gibbs- Helmholtz equation (Eq. 24) [75].

$$\Delta G^0 = \Delta H^0 - T\Delta S^0 \quad \text{Eq. 24}$$

2.5. Carbon materials derived from biowaste as adsorbents for MLT and CHP

The use of carbon materials derived from biomass is primarily based on their availability and environmental benefits through waste recycling. These materials exhibit unique morphologies and adjustable porosity, which are advantageous for their intended applications. Biomass naturally provides various macrostructures, making it suitable for preparing carbon materials with specific structures [76]. The microstructures inherited or developed during their formation include 0D spherical structures, 1D fibrous structures, 2D layered structures, and 3D skeletal structures [77]. These carbon materials are produced through processes such as pyrolysis, activation, or hydrothermal carbonization of plants, animals, household waste, and biomacromolecules [78].

Biowaste-derived carbon materials have found extensive applications in environmental protection due to their large specific surface area and high porosity, enabling the adsorption of harmful molecules from air and water [79]. It has been demonstrated that carbon materials with varying physical and chemical properties can be obtained depending on the initial biomass. Materials with higher lignin content, such as grape seeds and cherry pits, result in macroporous structures, whereas materials with high cellulose content, like almond shells, produce microporous structures. Bio-waste-derived materials have been successfully used to remove heavy chromium ions from water, showing higher adsorption capacity than commercial activated carbon. Additionally, these materials can exhibit selective adsorption, capturing pollutant molecules while leaving water molecules unaffected [80, 81].

Few biomass-derived carbon materials have been explored for the remediation of CHP from the environment. Various carbonization temperatures and activation processes have been utilized to synthesize these carbon materials, each yielding different adsorption capacities. For instance, Jacob et al. achieved an adsorption capacity of 3.20 mg g^{-1} for CHP removal using sugarcane bagasse that was merely carbonized at 450°C [82]. This straightforward carbonization process demonstrates that even simple thermal treatments can produce effective adsorbents, although the capacity might be limited compared to more complex treatments. Gonçalves et al. studied tobacco-derived carbon materials, exploring the effects of carbonization at 750°C and subsequent chemical activation using $ZnCl_2$ and NaOH. Their results revealed adsorption capacities of 0.683 mg g^{-1}, 1.602 mg g^{-1}, and 0.463 mg g^{-1}, respectively. This variation suggests that while chemical activation can influence adsorption efficiency, it does not always guarantee better performance. Their findings align with the conclusions of this study, highlighting that chemical activation does not necessarily enhance the adsorption efficiency of carbon materials [83]. Thuy et al. examined carbon materials derived from bamboo and coconut shells, which were carbonized at 600°C and then activated with steam at temperatures ranging from 800 to 1000°C for two hours. The resulting adsorption capacities were 0.588 mg g^{-1} for bamboo and 0.500 mg g^{-1} for coconut shell-derived activated carbon. These results indicate that steam activation, while effective, provides moderate adsorption capacities for CHP [84]. Katnić et al. investigated the potential of materials derived from fig pomace [85] and plum pomace [86], which were carbonized at 500°C and activated using gamma irradiation. The q_{max} values reported for CHP adsorption were both 0.495 mg g^{-1}, and for MLT 0.625 mg g^{-1} and 1.067 mg g^{-1}, respectively, demonstrating that gamma irradiation can be a useful activation method, though it might not significantly outperform other activation techniques in terms of capacity. In contrast to the aforementioned studies, Ettish et al. reported a substantially higher adsorption capacity of 12.37 mg g^{-1} for CHP using biowaste material derived from cinnamon sticks. This material was carbonized at 900°C and physically activated with CO_2, indicating that higher carbonization temperatures and physical activation methods can significantly enhance the adsorption performance of carbon materials [87].

3. AIM OF THE DOCTORAL DISSERTATION

This doctoral dissertation aims to explore the possibilities of using thermochemical conversion and activation processes to address the issue of harmful food biowaste, particularly SCG. Coffee is one of the most common waste materials worldwide, and its post-preparation residue, such as grounds, poses a significant environmental problem. By employing thermochemical conversion, SCG can be transformed into valuable materials, such as activated carbon, which can be used for various purposes, including the adsorption of pesticides like MLT and CHP.

The specific objectives of this doctoral dissertation are diverse. Firstly, different thermochemical conversion temperatures (400°C, 650°C, 900°C) and activation methods (KOH, H_3PO_4, CO_2, KOH/CO_2, H_3PO4/CO_2) will be explored to determine the most effective production of high-quality SCG adsorbents. Additionally, a detailed characterization of the obtained materials will be conducted using various analytical techniques such as scanning electron microscopy (SEM), energy-dispersive X-ray spectroscopy (EDX), Fourier-transform infrared spectroscopy (FTIR), and Brunauer-Emmett-Teller (BET) surface area analysis.

Furthermore, the mechanisms of MLT and CHP adsorption on SCG materials will be investigated to better understand how these materials interact with pollutants. Initially, the obtained materials will be tested for the remediation of MLT and CHP through a screening test, which will serve as the basis for further research. Materials exhibiting higher adsorption efficiency compared to SCG under environmentally relevant conditions will undergo detailed kinetic, isotherm, and thermodynamic studies. Kinetic studies will involve adsorption experiments of both OPs onto the selected materials, with contact times ranging from 1 min to 24 h, to determine the equilibrium time. The data obtained will be analyzed using kinetic models such as pseudo-first-order, pseudo-second-order, Elovich, and intraparticle diffusion models. The equilibrium time identified from these studies will be used as the contact time for further investigations of adsorption behavior. Isotherm studies will involve performing adsorption experiments of both OPs at concentrations ranging from 5×10^{-6} mol dm^{-3} to 5×10^{-4} mol dm^{-3} at three different temperatures (25°C, 30°C, and 35°C). The data will be evaluated against four isotherm models (Freundlich, Langmuir, Temkin, and Dubinin-Radushkevich) to understand the adsorption behavior. Additionally, the spontaneity and thermal effects of the adsorption process will be assessed through thermodynamic analysis.

The most promising materials will be further characterized using X-ray diffraction analysis (XRD), Raman spectroscopy, and Boehm titration to gain more insights into their structure and functional groups. The scope of adsorption experiments will be expanded by varying the materials' concentrations, testing adsorption under dynamic conditions, and examining the adsorption of OPs from their mixtures. The effects of MLT and CHP remediation using these materials on AChE inhibition will be tested using a modified Ellman's assay.

Finally, this dissertation will analyze the economic, environmental, and practical aspects of SCG material production and application as adsorbents for MLT and CHP. This includes assessing production costs, environmental impact, and the practical feasibility of applying these materials in various remediation scenarios. Combining these specific aims will provide deeper insights into the potential of SCG materials as adsorbents for harmful pollutants while providing important insights into thermochemical conversion and activation processes.

4. EXPERIMENTAL

4.1. Materials

4.1.1. Adsorbents

Coffee (purchased from the local market (80% Arabica and 20% Robusta) was brewed (treated with boiling water) and left for 2 h at room temperature until it became cooled. Next, the coffee grounds were separated with filtration and left to dry at room temperature for 24 h. Then, in order to release the leftover moisture, the obtained spent coffee grounds were dried in the oven at 80 °C for 1 h.

Table 1. Process of materials synthesis

Material	T_1 (°C)	Y_1 (%)	Grinding (min)	Chemical activation	T_2 (°C)	Physical Activation	Y_2 (%)	Grinding (min)	Y (%) ($Y_1 \times Y_2$)
SCG	/	/	15	/	/	/	/	/	/
K	/	/	/	KOH	/	/	/	15	/
400	400	21	15	/	/	/	/	/	21
400K	400	21	15	KOH	400	/	84	15	17.6
400P	400	21	15	H_3PO_4	400	/	80	15	16.8
400C	400	19	15	/	/	CO_2	/	/	19
400KC	400	21	15	KOH	400	CO_2	91	15	19.1
400PC	400	21	15	H_3PO_4	400	CO_2	92	15	19.3
K400	/	/	/	KOH	400	/	5.8	15	5.8
650	650	18	15	/	/	/	/	/	18
650K	650	18	15	KOH	650	/	86	15	15.5
650P	650	18	15	H_3PO_4	650	/	86	15	15.5
650C	650	17	15	/	/	CO_2	/	/	17
650KC	650	18	15	KOH	650	CO_2	82	15	14.8
650PC	650	18	15	H_3PO_4	650	CO_2	85	15	15.3
900	900	15	15	/	/	/	/	/	15
900K	900	15	15	KOH	900	/	81	15	12.2
900P	900	15	15	H_3PO_4	900	/	70	15	10.5
900C	900	14	15	/	/	CO_2	/	/	14
900KC	900	15	15	KOH	400	CO_2	84	15	12.6
900PC	900	15	15	H_3PO_4	900	CO_2	14	15	2.1

The temperatures for thermochemical conversion are chosen based on thermogravimetric analysis of SCG. The temperature of 400°C was chosen as the temperature during the carbonization process, aiming for less CO_2 release, less electricity consumption, and higher yield. A temperature of 650°C was chosen as the beginning of the third stage of mass loss, while the yield is still close to the yield at 400°C. The highest temperature, 900°C, was chosen as the maximum carbonization temperature in the carbonization furnace used. Carbonization at higher temperatures would not be of great importance in terms of economic profitability, as well as the yield itself. As carbonization temperatures were determined, materials syntheses proceeded as indicated in Table 1. The samples were heated under a nitrogen atmosphere flow of 100 L h^{-1} with a heat rate of 5°C min^{-1} using Protherm Electrical Tube

Furnace obtained from Protherm Furnaces, Turkey. Samples were chemically activated by mixing in a 1:2 mass ratio with 1 mol dm^{-3} KOH and 1 mol dm^{-3} H_3PO_4. Physical activation was performed in 100 L h^{-1} flow of CO_2 gas for one hour at the reached carbonization temperature for a specific sample. Each sample was ground in an agate mortar with a pestle for 15 min. The table also shows the corresponding yields for each stage of thermochemical conversion of the samples (Y_1 and Y_2) and the total yield in percent of the initial mass (Y).

After the synthesis, 200 mg of the material was weighed, washed with 50 mL of 0.1 mol dm^{-3} NaOH, 50 mL of 0.1 mol dm^{-3} HCl, and 50 mL of deionized water, and finally suspended in 50 mL of 50% ethanol to obtain a stock suspension with a mass concentration of 2 mg mL^{-1}.

4.1.2. Chemicals

In this doctoral dissertation, the adsorbates used were organothiophosphate pesticides: malathion (diethyl (dimethoxythiophosphorylthio) succinate), and chlorpyrifos (O,O-diethyl-O-(3,5,6-trichlor-2-pyridinyl) phosphorothioate), with a purity of >98%, obtained from Pestinal, Sigma-Aldrich. Stock solutions of the pesticides, at a concentration of 1×10^{-1} mol dm^{-3}, were prepared by dissolving the appropriate amount of pesticide standards in ethanol and stored at low temperatures. Working solutions of the pesticides were prepared daily by diluting the stock ethanol solutions in deionized water.

Other chemicals used in the experimental work included: ethanol (C_2H_5OH) and acetonitrile (CH_3CN) of HPLC grade from J.T. Baker, phosphoric acid (H_3PO_4), sodium hydrogen carbonate ($NaHCO_3$), sodium carbonate (Na_2CO_3), and sodium hydroxide (NaOH), purchased from Fluka Biochemika, Germany acetylcholinesterase (AChE) from electric eel with a specific activity of 288 IU mg^{-1}, acetylcholine iodide (AChI), 5,5'-dithio-bis-(2-nitrobenzoic) acid (DTNB), and sodium dodecyl sulfate ($NaC_{12}H_{25}SO_4$) from Sigma Aldrich, helium (He) and carbon dioxide (CO_2) gasses from Messer.

4.2. Methods

4.2.1. Physicochemical characterization of synthesized materials

Thermogravimetric analysis (TGA) was performed using a TA Instruments SDT 2960 thermoanalytical device (TA Instruments, Inc., New Castle, DE, USA). The analysis was conducted at a heating rate of 10 °C per minute, with the temperature increasing up to 900 °C under a continuous flow of helium gas provided by Messer, Belgrade, Serbia. TGA allowed the precise determination of the thermal stability and processes of the initial material.

The morphology and elemental composition of the samples were examined using a PhenomProX scanning electron microscope (SEM) obtained from Thermo Fisher Scientific, Waltham, MA, USA. This analysis was further enhanced by incorporating Energy-Dispersive X-ray Analysis (EDX), providing detailed insights into the elemental distribution and structural characteristics of the samples at the microscale.

Crystal phase identification was conducted using a Rigaku Ultima IV diffractometer equipped with a Ni-filtered Cu Kα radiation source. The crystallographic data were collected in Bragg-Brentano

mode, scanning over a 2θ range from 10 to 90 degrees at a rate of 0.2 degrees per minute. This technique enabled the determination of the crystal structures present in the samples.

Fourier-transform infrared (FTIR) spectra were obtained using a Nicolet iS20 FT-IR spectrophotometer (Thermo Fisher Scientific, Waltham, MA, USA). Spectral data were acquired over a range of wavenumbers from 4000 to 400 cm^{-1}, with each measurement comprising 64 scans at a resolution of 4 cm^{-1}. This analysis provided comprehensive information about the functional groups and molecular bonds within the samples.

Raman spectra of the samples were recorded using a DXR Raman microscope (Thermo Fisher Scientific, USA). The samples were excited using a 532 nm diode laser, with 2 mW of power focused on a 2.1 μm spot on the sample surface. The spectra were obtained as an average of four measurements taken at different spots on each sample, with each measurement consisting of 10 exposures of 10 seconds each. This method allowed for the detailed characterization of the vibrational modes of the sample materials.

To determine the amount of oxygen functional groups on the surface of the materials, Boehm titrations were performed. A 10 mL suspension of the material at a concentration of 1 mg mL^{-1} was titrated by adding 10 μL of 0.01 mol dm^{-3} solutions of $NaHCO_3$, Na_2CO_3, and NaOH. $NaHCO_3$ neutralizes carboxyl groups, Na_2CO_3 neutralizes both carboxyl and lactone groups, and NaOH neutralizes carboxyl, lactone, and phenol groups. The amounts of these functional groups were calculated based on the differences in the volume of titrant used. pH measurements were conducted using a Metrohm 713 pH meter equipped with a combined electrode to ensure accuracy.

Zeta potential measurements were carried out using a Nano ZS zetasizer system from Malvern Instruments, UK, which is equipped with a 633 nm He-Ne laser. Specifically, 1 mL of a 0.5 mg mL^{-1} concentration of the materials was titrated using HCl and NaOH to cover a pH range from 1 to 14, and the zeta potential of the suspension was measured. These measurements provided valuable information on the stability of samples in suspension, as well as their surface charge.

The specific surface area and total pore volume of the materials were examined using an Autosorb-iQ gas sorption system (Anton Paar QuantaTec Inc., Graz, Austria). Nitrogen adsorption was conducted at an isothermal temperature of −196.15 °C. Prior to the analysis, the samples were outgassed for 5 hours at 300 °C under vacuum to ensure the removal of any adsorbed contaminants. This analysis allowed a comprehensive assessment of the textural properties of the materials.

4.2.2. Adsorption experiments

4.2.2.1. Adsorption in batch (stationary conditions)

The efficiency of the materials for the removal of selected organophosphate pesticides from aqueous solutions was investigated. The adsorbents were synthesized, and their suspensions were prepared as described in Section 4.1.1. Stock solutions of MLT and CHP were prepared at concentrations ranging from 1×10^{-5} to 1×10^{-3} mol dm^{-3}. The resulting pesticide solutions and material suspensions were mixed in a 1:1 ratio, thereby further diluting them to final adsorbent concentrations of 0.1 to 1 g dm^{-3} and pesticide concentrations ranging from 5×10^{-6} mol dm^{-3} to 5×10^{-4} mol dm^{-3}. The mixtures were left to stir in an orbital shaker (Orbital Shaker Incubator Grant-bio ES-20) for the desired period at the

appropriate temperature. After the incubation period, the suspensions were filtered through a nylon filter (pore size 0.22 μm, diameter 13 mm, KX Syringe Filter, Kinesis) and prepared for chromatographic analysis. The concentration of adsorbed pesticide was determined from the difference between the initial concentration and the concentration of the remaining pesticide after adsorption. Control experiments were conducted in the same manner but without the carbon adsorbents to avoid the influence of potential pesticide degradation within the timeframe of the described experiments. To examine the influence of different working parameters and to find the optimal conditions for the adsorption process, the mass of the adsorbent, the initial concentration of the pesticide, and the contact time were varied.

To investigate the kinetic parameters of the adsorption process, a suspension of the adsorbents at a final concentration of 1 mg mL^{-1} was incubated with MLT and CHP at a final concentration of 5×10^{-5} mol dm^{-3} for various time intervals ranging from 1 minute to 24 hours at 25 °C. The obtained experimental data of CHP and MLT adsorption onto the investigated adsorbents were used to determine the equilibrium time and were analyzed using nonlinear models: PFO, PSO, Elovich, and IPD kinetic model.

Additionally, to further examine the adsorption process, 1 mg mL^{-1} of the adsorbents was incubated with MLT and CHP in a final concentration range of 5×10^{-6} to 5×10^{-4} mol dm^{-3} at temperatures of 25, 30, and 35°C for the time determined to be the equilibrium time. The resulting data were fitted to nonlinear isotherm models, including Freundlich, Langmuir, Temkin, and Dubinin–Radushkevich.

4.2.2.2. Adsorption under dynamic conditions, regeneration, and reuse of adsorbents

To investigate adsorption under dynamic conditions, a commercial nylon membrane filter (pore size 0.22 μm, diameter 13 mm, KX Syringe Filter, Kinesis) was modified to contain a layer of adsorbent. This modification involved injecting 0.5 mL of the materials stock suspension into the commercial filter. The solvent was then removed from the filter using compressed air. The pesticide solution was injected through the modified filter at a rate of 1 cm^3 per minute. The filtrate was subjected to UPLC analysis to determine the pesticide concentration. A control experiment was conducted using an unmodified filter.

In order to investigate the adsorbent regeneration and reuse, the filter was washed using 5 mL of 25 % ethanol solution and reused as the adsorbent for the same pesticide.

4.2.2.3. Determining the concentration of OPs using Ultra Performance Liquid Chromatography

The concentration of organothiophosphorus pesticides was determined using Ultra Performance Liquid Chromatography (UPLC). A Waters ACQUITY UPLC with a PDA detector was used to determine the pesticide concentration. BEH C18 column was used under isocratic conditions: mobile phase A - 10% acetonitrile in water and B - pure acetonitrile. The injected volume was 5 μL, while the flow rate was 0.2 mL min^{-1} in all cases. The mobile phase in the case of the MLT consisted of 40%A and 60%B, while in the case of CHP, it consisted of 20% A and 80% B for individual detection. The retention time for MLT under these conditions was 2.5 min, while it was 2.7 min for chlorpyrifos. Investigation of the mixtures was performed using a mobile phase consisting of 30% A and 70% B, and the retention times were 1.7 min for MLT and 4.4 min for CHP. Both pesticides were detected at a wavelength of 200 nm. The UV/VIS spectra and chromatograms of MLT and CHP are given in Figure 4. Control experiments were performed in an identical manner but without the presence of the material.

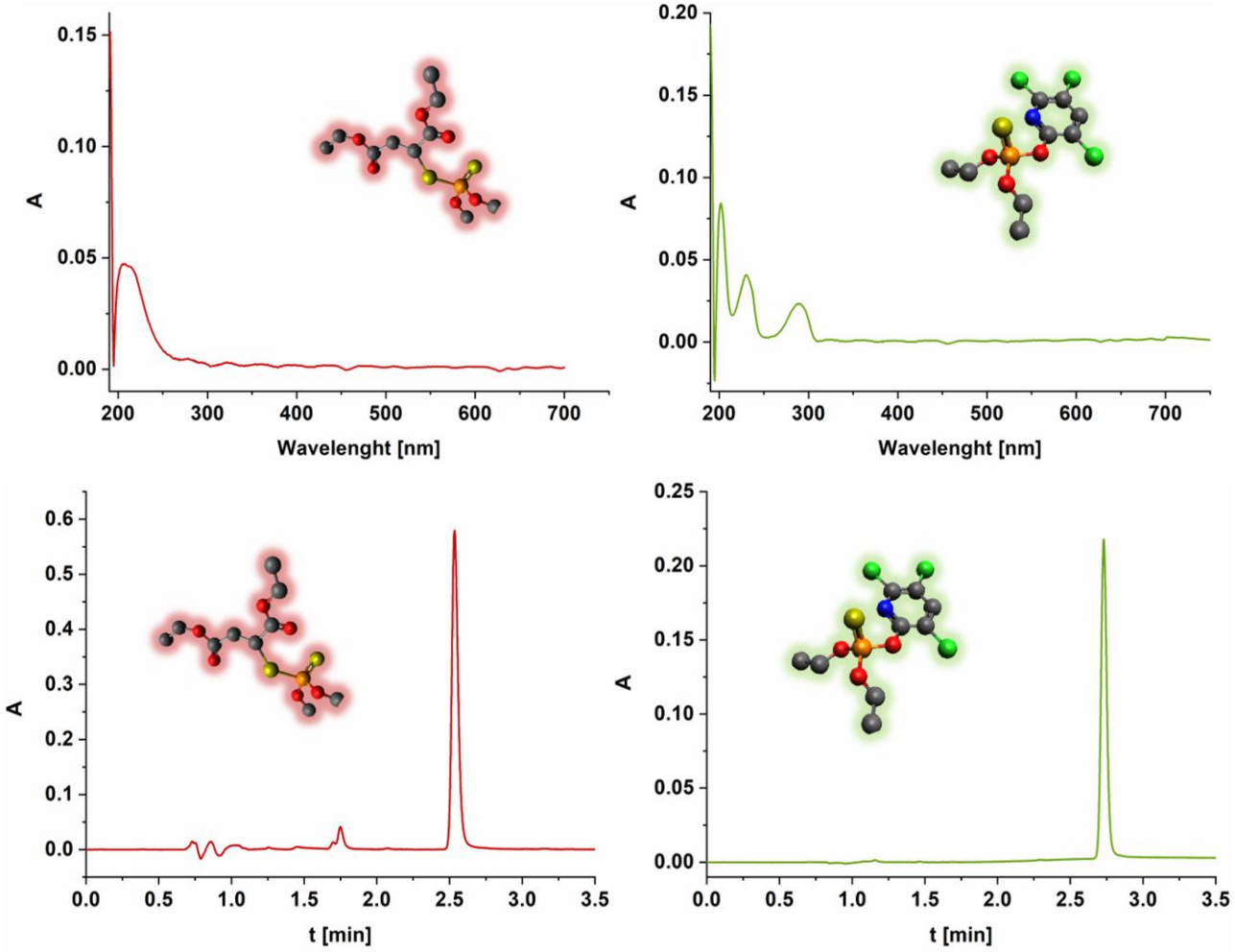

Figure 4. UV-VIS spectra (top row) and chromatograms (bottom row) of MLT (left) and CHP (right)

4.2.2.4. Assessment of AChE activity inhibition

The physiological effects of the treated solutions were analyzed through measurements of AChE inhibition using a modified Ellman's procedure. 2.5 IU of commercially purified AChE from an electric eel was exposed to the organophosphate solutions in a 50 mM phosphate buffer at pH 8.0 and 37 °C in a final volume of 0.650 mL. The enzymatic reaction was initiated by combining AChI with DTNB as the chromogenic reagent. The reaction was allowed to proceed for 8 minutes before being stopped with 10% sodium dodecyl sulfate (SDS). Thiocholine, the reaction product, reacts with DTNB to form 5-thio-2-nitrobenzoate, whose optical absorption was measured at 412 nm using UV-VIS Perkin Elmer, Lambda 35 spectrophotometer. The enzyme concentration was maintained at a level that produced an optimal spectrophotometric signal. The physiological effects were quantified as AChE inhibition, calculated as follows:

$$I = 100 \times \frac{A_0 - A}{A_0} \qquad \text{Eq. 25}$$

where A_0 and A stand for the AChE activity in the absence of OP and the one measured after exposure to a given OP.

5. RESULTS AND DISCUSSION

5.1. Screening test

Before the start of the experiments, a screening test was performed, which involved determining the percentage of adsorption of MLT and CHP with an initial concentration of 5×10^{-5} mol dm^{-3} on all the synthesized material within 1 hour. The results of the screening test are shown in Table 2.

Table 2. Percent of adsorbed MLT and CHP (5×10^{-5} mol dm^{-3}) after 1h

Material	MLT	CHP
SCG	6.7±0.3	3.7±0.2
K	32±1	34±1
400	21±1	32±2
400K	24±1	0.22±0.01
400P	13.9±0.7	1.44±0.07
400C	25±2	28±2
400KC	12.9±0.6	0.42±0.02
400PC	11.2±0.6	6.32±0.03
K400	45±2	18.2±0.9
650	0.46±0.02	9.5±0.5
650K	0	0
650P	0	8.2±0.4
650C	1.72±0.09	11.0±0.6
650KC	0	5.7±0.3
650PC	1.98±0.09	14.2±0.7
900	8.7±0.4	30±1
900K	42±2	42±2
900P	6.8±0.3	12.0±0.6
900C	22±1	21±1
900KC	42±2	43±2
900PC	96±5	96±5

Significant differences in the adsorption of these two pesticides on the same materials can already be observed in the screening test. With the increasing temperature of thermochemical conversion and activations, these differences decrease, and the percentages of both adsorbed pesticides become almost the same, as can be seen in the examples of 900K, 900C, 900KC, and 900PC. It was shown that 19 out of 20 synthesized materials showed higher adsorption of CHP than SCG, while in the case of MLT adsorption, that number was 10. Interestingly, the entire series of materials carbonized at 650°C shows a much lower percentage of MLT adsorption compared to SCG. At the same time, samples 650K, 650P, and 650KC do not adsorb MLT under these experimental conditions. Sample 650K also does not adsorb CHP under the given experimental conditions.

In the continuation of the research within this doctoral dissertation, attention will be paid to investigating the adsorption of MLT and CHP onto SCG as the baseline material and samples that showed a higher percentage of adsorption than SCG on the screening test. The adsorbents will be divided into 6 sections: SCG-baseline material, K, materials carbonized at 400 (SCG 400), materials carbonized at 650 (SCG 650), materials carbonized at 900 (without 900PC; SCG 900), while the special attention will be paid to 900PC, as the most promising material.

5.2. Spent coffee grounds (SCG) – baseline material

5.2.1. Characterization of SCG

To investigate the morphology and the chemical composition of SCG, SEM, and EDX were used. The results are presented in Figure 5. SEM micrograph showed that SCG has a sponge-like, highly porous, heterogeneous structure. It can be seen that the cavities are randomly distributed on the surfaces of the materials with openings of different sizes. EDX analysis showed that C, O, and N are present in high percentages in SCG, namely 64.85 at.%, 27.57 at.%, and 6.83 at.%, respectively, as could be expected. Besides these, EDX analysis revealed the presence of K, Mg, S, Ca, and P in traces, with combined at.% less than 1.

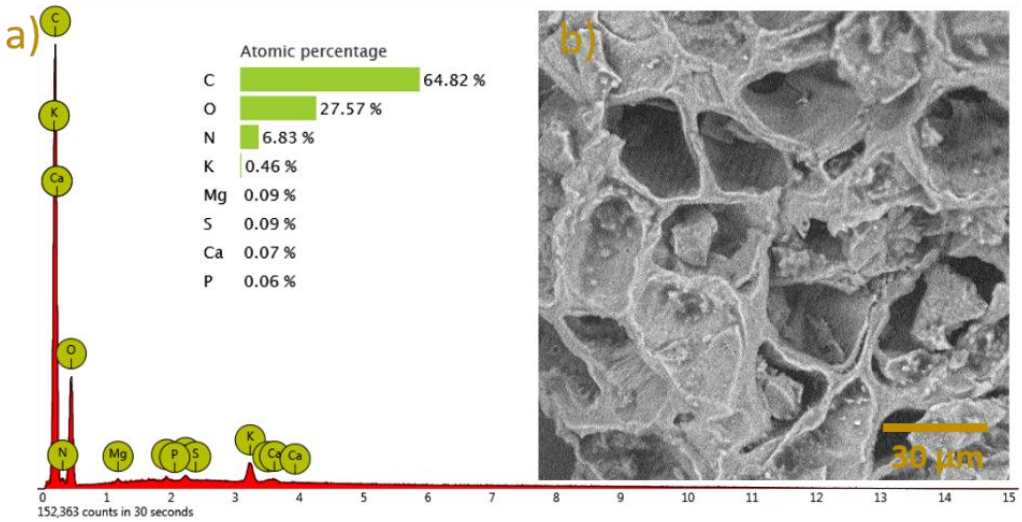

Figure 5. a) EDX spectrum and elemental composition in at.% of SCG; b) SEM micrograph of SCG (magnification 2000×)

The FTIR spectrum of SCG (Figure 6) provides detailed insights into the material's chemical structure through various characteristic bands corresponding to specific molecular vibrations. The broad band at 3307 cm^{-1} is assigned to the stretching vibrations of O-H groups, which arise due to hydrogen bonding. This broad band indicates the presence of hydroxyl groups, suggesting significant moisture or alcohol content in the material. The bands at 3010 cm^{-1} and 2924 cm^{-1} are indicative of C-H bond stretching. Specifically, the band at 3010 cm^{-1} corresponds to sp^2 hybridized carbon atoms, typically found in alkenes and aromatic rings, while the band at 2924 cm^{-1} is associated with sp^3 hybridized carbon atoms, found in alkanes [88]. These bands highlight the presence of both aliphatic and aromatic C-H bonds within the SCG structure. A sharp band at 1745 cm^{-1} is attributed to the C=O stretching vibration, indicative of carbonyl groups such as those found in carboxylic acids, esters, or aldehydes. This band suggests the presence of oxidized carbon structures or organic acids in the SCG [89]. The band at 1635 cm^{-1} corresponds to the C=N stretching vibration, which indicates the presence of nitrogen-containing groups such as imines or amides. The bands at 1521 cm^{-1} and 1441 cm^{-1} are indicative of aromatic skeletal stretching and aromatic C-H in-plane vibrations, respectively. The band at 1521 cm^{-1} represents the stretching of the aromatic ring itself, while the band at 1441 cm^{-1} represents vibrations coupled with the aromatic C-H bonds [90]. These features point to the presence of condensed aromatic systems within the SCG, contributing to its stability and potential reactivity [91].

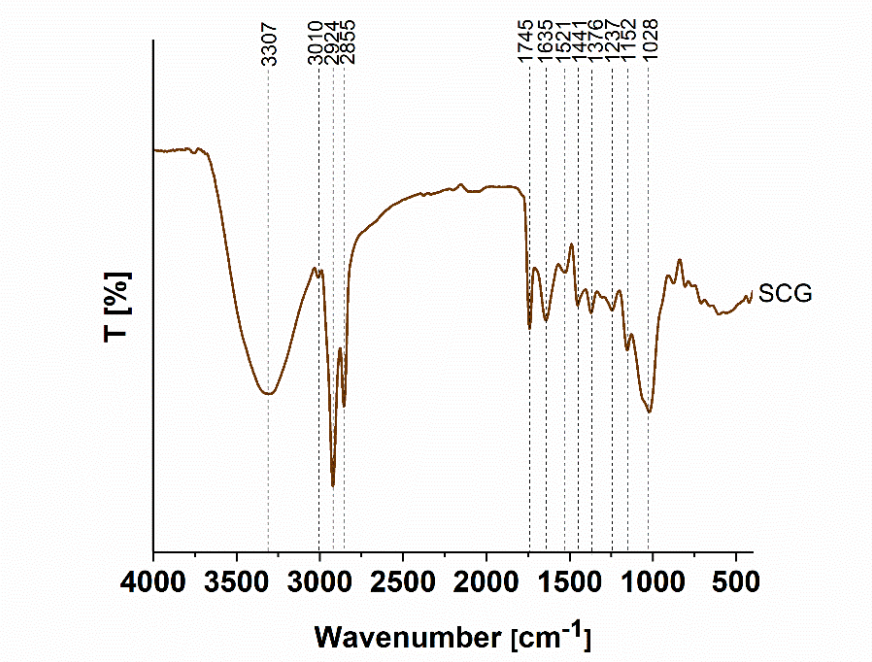

Figure 6. FTIR spectrum of SCG

In order to determine the temperatures at which the thermochemical conversion of this biowaste will be performed, a thermogravimetric analysis of the baseline material was performed. The resulting TGA curve is shown in Figure 7. The TGA curve shows that by increasing the temperature from 20 to 900°C in a helium atmosphere, SCG has three significant mass losses. In the first stage, from 20 to 85°C, SCG loses 15% of its initial mass. The second stage, carbonization, starts at 200°C and ends at 500°C, and during this stage, SCG loses 48% of its initial mass. In the last, third stage, from 670 to 900°C, SCG loses an additional 15% of its initial mass. After heating SCG up to 900°C, 12% of the initial mass remains.

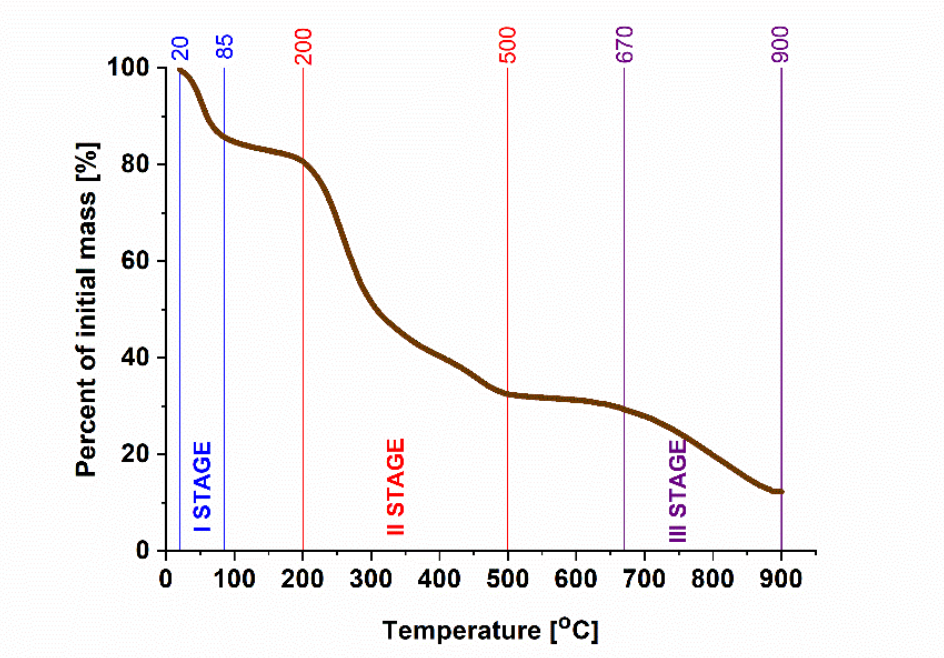

Figure 7. TGA curve of SCG under He atmosphere

5.2.2. Adsorption of MLT and CHP onto SCG

5.2.2.1. Kinetics of MLT and CHP adsorption onto SCG

The graphical representations of investigated kinetic models are given in Figure 8, while the obtained parameters are given in Table 3. By examining the results shown in Figure, it can be concluded that adsorption equilibrium is achieved after 10 minutes for MLT and 1440 minutes for CHP. As the equilibrium between both pesticides and SCG is achieved after 1440 min, this time will be further used as the contact time in the experiments. Additionally, it appears that the PFO kinetic model aligns better with the experimental data for both MLT and CHP adsorption compared to the PSO model, based on the R^2 and χ^2 values. Under the experimental conditions, the calculated equilibrium adsorption capacities of SCG are 3.31 mg g^{-1} for MLT and 2.26 mg g^{-1} for CHP. A higher k_1 value for MLT adsorption indicates a faster adsorption rate than that for CHP. The initial adsorption rate and the desorption constant, obtained from the Elovich model, also indicate that CHP adsorption is significantly slower than MLT adsorption on SCG, as the α value is lower than the β value for CHP adsorption. When plotting q_t against $t^{0.5}$, three linear stages for MLT and two linear stages for CHP are clearly visible in the IPD kinetic model. It can be concluded that three processes influence the rate of MLT adsorption, whereas two processes control CHP adsorption, with one process dominating the adsorption kinetics at each time range. The k_{id} values decrease by an order of magnitude after the breakpoints, indicating slower adsorption in each subsequent stage. The C value increases, suggesting that the boundary layer plays a significant role in the adsorption of MLT and CHP onto SCG. The differences in the molecular structure of MLT and CHP, with MLT being aliphatic and CHP containing an aromatic moiety, result in significantly different adsorption kinetics.

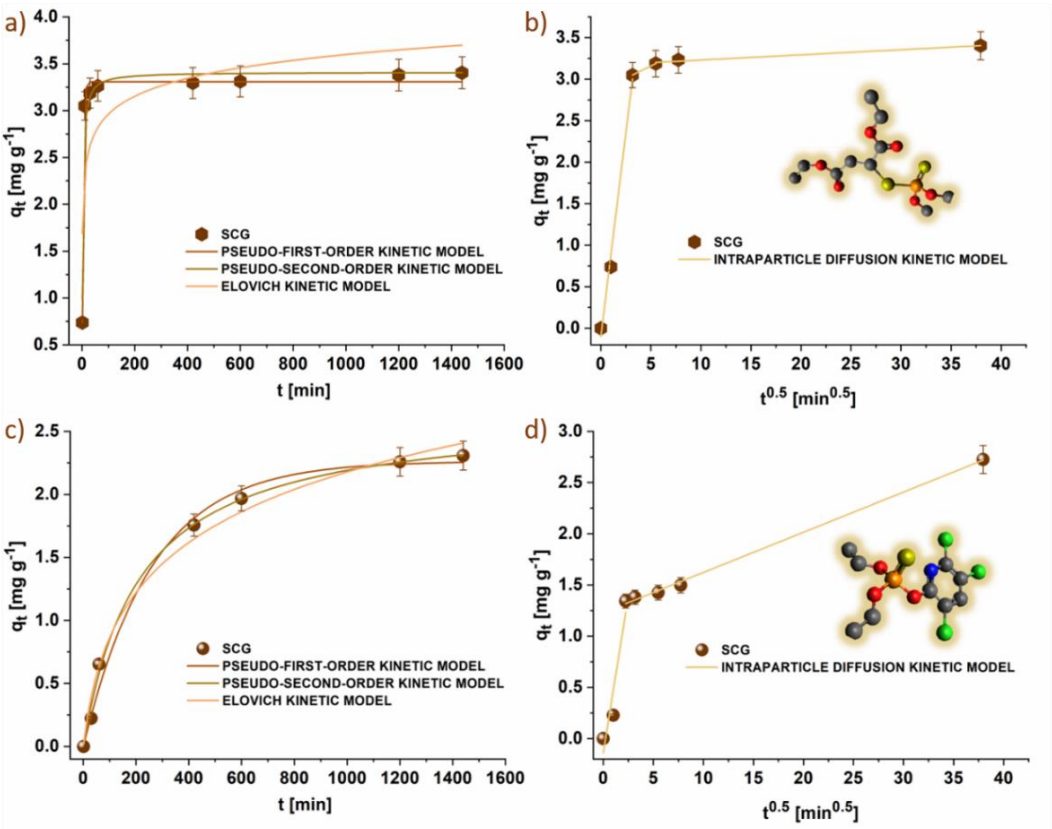

Figure 8. Graphical representations of kinetic models for MLT (a,b) and CHP (c,d) adsorption onto SCG

Table 3. Kinetic parameters of MLT and CHP (5×10^{-5} mol dm^{-3}) adsorption on SCG (1 mg mL^{-1}) at 25°C

OP→	MLT	CHP
Pseudo-first-order kinetic model		
q_e ($mg\ g^{-1}$)	3.31 ±0.03	2.26 ±0.07
$k_1 \times 10^2$ (min^{-1})	25.0 ±0.2	0.381 ±0.005
χ^2	0.004	0.006
R^2	0.997	0.994
Pseudo-second-order kinetic model		
q_e ($mg\ g^{-1}$)	3.41 ±0.08	2.66 ±0.08
$k_2 \times 10^2$ ($mg\ min^{-1}\ g^{-1}$)	12.2 ±0.3	0.181 ±0.003
χ^2	0.037	0.008
R^2	0.970	0.993
Elovich kinetic model		
α ($mg\ g^{-1}\ min^{-1}$)	3.0 ±0.3	0.018 ±0.005
β ($g\ mg^{-1}$)	1.5 ±0.2	1.55 ±0.08
χ^2	0.215	0.011
R^2	0.859	0.990
Intraparticle diffusion model		
I part		
C ($mg\ g^{-1}$)	0.000	0.000
k_{id} ($mg\ g^{-1}\ min^{-0.5}$)	0.982	0.613
R^2	0.987	0.921
II part		
C ($mg\ g^{-1}$)	2.861	1.234
k_{id} ($mg\ g^{-1}\ min^{-1}$)	0.060	0.039
R^2	–	0.997
III part		
C ($mg\ g^{-1}$)	3.172	–
k_{id} ($mg\ g^{-1}\ min^{-0.5}$)	0.0062	–
R^2	0.963	–

5.2.2.2. Isotherm studies of MLT and CHP adsorption onto SCG at 25, 30, and 35°C

The graphical representations of the experimental data for MLT and CHP adsorption onto SCG, along with the corresponding isotherm model fits, are shown in Figure 9, and the calculated parameters, including R^2 and χ^2, are provided in Table 4.

The n-value from the Freundlich isotherm model for MLT adsorption being greater than 1 suggests that the adsorption process is favorable. However, as the temperature increases, the n-value decreases, indicating that the adsorbent's affinity for MLT diminishes with higher temperatures. The Langmuir model showed the best fit with the experimental data, suggesting that MLT is adsorbed as a monolayer on an energetically homogeneous surface, with no interactions between the adsorbed molecules. This implies that all active sites on the adsorbent are energetically equivalent, and equilibrium is achieved when a monolayer forms. Despite the maximum adsorption capacity (q_{max} = 7.16 mg g^{-1}) remaining relatively unaffected by temperature changes, the decrease in the K_L value indicates weakened interactions between MLT and SCG. This is further supported by the decrease in the E value from the Dubinin–Radushkevich isotherm model, suggesting that the adsorption mechanism is likely physisorption since E << 8 kJ mol^{-1}. The Temkin isotherm model showed that b_T values, related to adsorption heat, increased with temperature, suggesting easier adsorption of MLT onto SCGs. However, the higher χ^2 values for the Temkin model compared to other models indicate less reliable findings.

For CHP adsorption, the Freundlich isotherm model also showed n-values above 1, indicating a favorable adsorption process. Similar to MLT, the n-value for CHP decreases with rising temperature, suggesting reduced adsorbent affinity at higher temperatures. However, due to not-high R^2 values for all temperatures, these n-values should be interpreted cautiously. The Langmuir isotherm model again provided the best fit for CHP adsorption across all temperatures, indicating that CHP is adsorbed as a monolayer on an energetically homogeneous surface without interactions between the adsorbed molecules. At 25 °C, CHP adsorption onto SCG had the highest K_L value (K_L = 9.23 dm^3 mg^{-1}), consistent with the Freundlich n-values. The q_{max} values for CHP increased with temperature, with a maximum adsorption capacity of 7.00 mg g^{-1}. The energy of adsorption from the DR isotherm model suggests that the primary mechanism is physisorption, although, at 25 °C, there is strong evidence for some chemisorption. The Temkin isotherm model indicated that b_T values decreased with rising temperatures, aligning with other parameters showing a reduced readiness of CHP molecules for adsorption on SCG at higher temperatures.

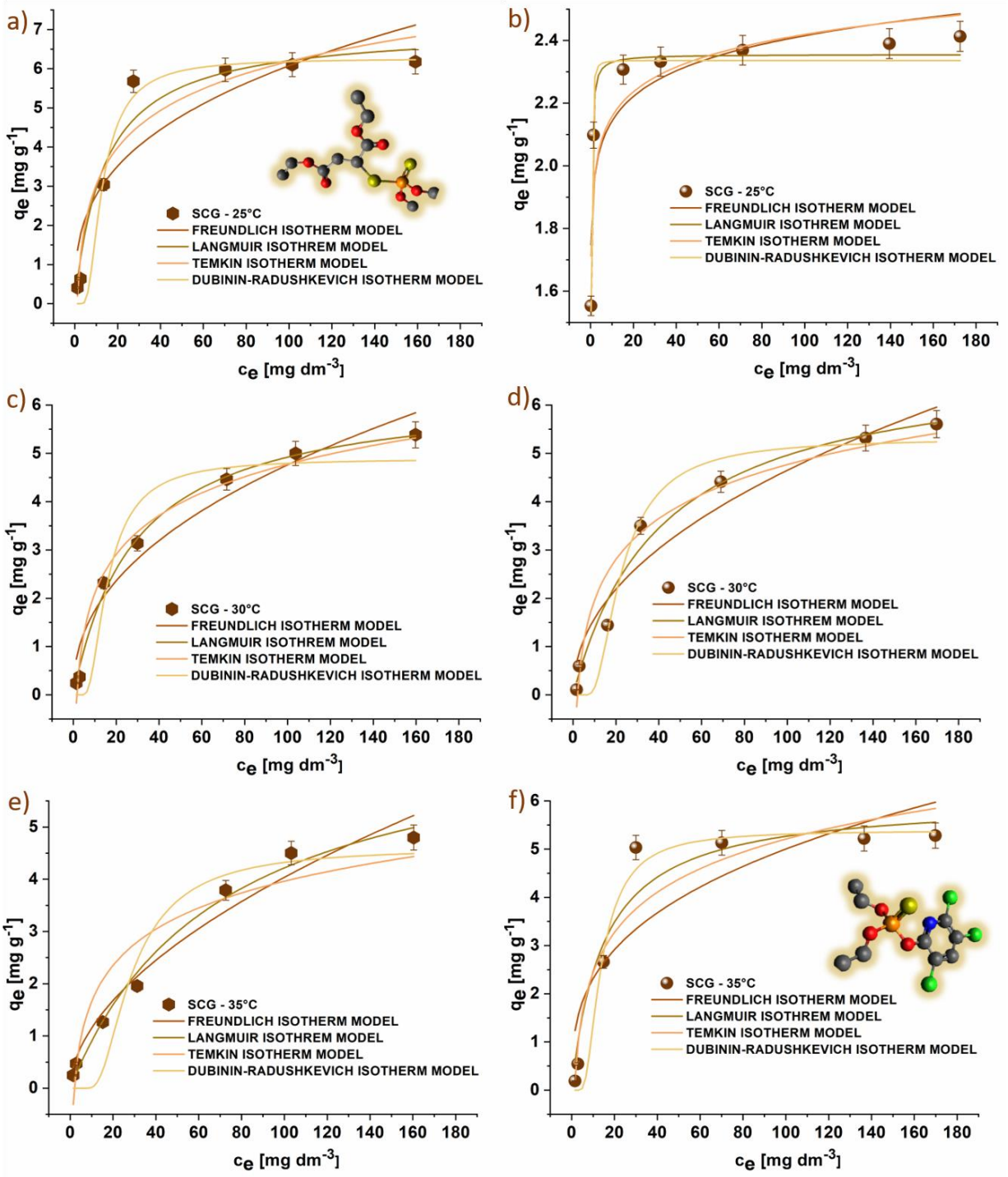

Figure 9. Graphical representations of isotherm models for MLT (a,c,e) and CHP (b,d,f) adsorption onto SCG (1 mg mL^{-1}) at 25°C (a,b), 30°C (c,d), and 35°C (e,f)

Table 4. Isotherm adsorption parameters of MLT and CHP adsorption onto SCG (1 mg mL^{-1}) at 25°C, 30°C, and 35°C

	MLT			CHP		
T[°C]	**25**	**30**	**35**	**25**	**30**	**35**
Freundlich isotherm						
K_F ($(dm^3 mg^{-1})^{1/n}$)	1.3 ±0.1	0.642 ±0.002	0.333 ±0.003	1.9 ±0.1	0.544 ±0.005	1.1 ±0.4
n	2.9 ±0.8	2.29 ±0.04	1.83 ±0.02	19 ±4	2.13 ±0.04	3 ±1
χ^2	1.312	0.242	0.119	0.018	0.341	1.203
R^2	0.808	0.946	0.967	0.808	0.934	0.771
Langmuir isotherm						
$K_L \times 10^2$ ($dm^3 mg^{-1}$)	7.22 ±0.02	3.52 ±0.04	1.41 ±0.02	923 ±9	2.44 ±0.06	7.05 ±0.03
q_{max} (mg g^{-1})	7.06 ±0.05	6.33 ±0.02	7.16 ±0.06	2.36 ±0.03	7.00 ±0.05	6.04 ±0.05
χ^2	0.316	0.022	0.045	0.003	0.108	0.323
R^2	0.954	0.995	0.988	0.968	0.979	0.938
Temkin isotherm						
K_T ($dm^3 mg^{-1}$)	0.919 ±0.003	0.611 ±0.001	0.52 ±0.03	360000 ±10000	0.505 ±0.005	0.76 ±0.01
b_T (J g mol^{-1} mg^{-1})	1800 ±210	2170 ±120	2600 ±370	16700 ±240	2070 ±210	2130 ±280
χ^2	0.532	0.080	0.420	0.015	0.288	0.487
R^2	0.922	0.982	0.885	0.845	0.944	0.907
D-R isotherm						
$K_{DR} \times 10^6$ ($mol^2 J^{-2}$)	21.3 ±0.4	31.5 ±0.9	97 ±1	0.021 ±0.002	62.0 ±0.2	23.1 ±0.4
q_{DR} (mg g^{-1})	6.26 ±0.02	4.89 ±0.03	4.60 ±0.04	2.34 ±0.04	5.31 ±0.03	5.39 ±0.02
E (J mol^{-1})	153 ±5	126 ±9	72 ±8	4850 ±30	89.8 ±0.9	147 ±5
χ^2	0.155	0.273	0.313	0.007	0.158	0.120
R^2	0.977	0.939	0.914	0.928	0.969	0.977

5.2.2.3. Thermodynamic analysis of MLT and SCG adsorption onto SCG

To get insight into the thermodynamics of the process, Van't Hoff plots were constructed and analyzed (Figure 10). The obtained thermodynamic parameters, presented in Table 5, provide insights into the adsorption behavior of MLT and CHP onto SCG. The adsorption of MLT is characterized as an exothermic process accompanied by a small negative change in entropy. This suggests that MLT adsorption on SCG is driven by enthalpy, which compensates for the entropy reduction, resulting in a negative ΔG^0 that increases with temperature.

Conversely, CHP adsorption onto SCG is an endothermic process associated with a significant positive change in entropy. This indicates that CHP adsorption is driven by entropy. The Gibbs free energy change for CHP adsorption is also negative, and it becomes more negative compared to MLT, decreasing with temperature. This implies spontaneous adsorption, consistent with experimental observations.

The differences in the thermodynamic parameters for MLT and CHP adsorption can be attributed to the distinct types of interactions between SCG and these pesticides, as MLT is an aliphatic molecule and CHP contains aromatic moiety.

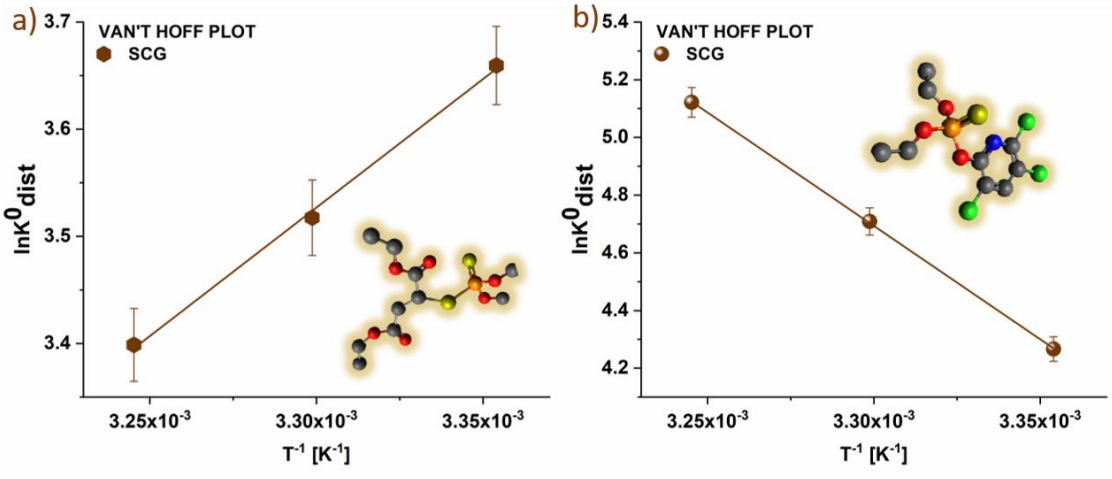

Figure 10. Van't Hoff plots for adsorption of MLT (a) and CHP (b) onto SCG

Table 5. Thermodynamic parameters for MLT and CHP adsorption onto SCG (1 mg mL^{-1})

	ΔH^0 [kJ mol^{-1}]	ΔS^0 [J $mol^{-1}K^{-1}$]	ΔG^0 [kJ mol^{-1}]			R^2
T [°C] →			25	30	35	
MLT	− 19.9 ±0.5	− 36.5 ±0.8	−9.12 ±0.03	− 8.78 ±0.03	− 8.7 ±0.03	0.996
CHP	65.3 ±0.7	254 ±2	−10.6 ±0.3	− 11.9 ±0.3	−13.1 ±0.3	0.9997

5.2.2.4. Assessment of AChE activity inhibition after MLT and CHP remediation using SCG

The neurotoxicological assessment was performed as described in Section 4.2.2.4, and the histogram showing the difference in the activity of AChE before and after the adsorption of MLT and CHP is shown in Figure 11.

It can be seen that the AChE inhibition due to the contact with samples was reduced after the adsorption in all cases, indicating that no more toxic products, such as OPs' oxo-forms, were formed during this process.

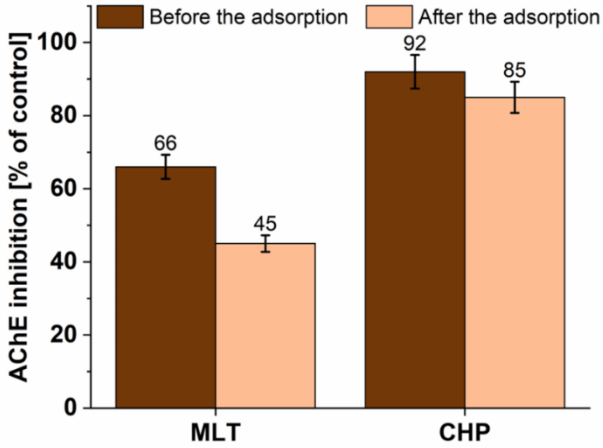

Figure 11. Histogram of inhibition of AChE activity before and after the adsorption of MLT and CHP using SCG

5.2.3. Discussion on MLT and CHP adsoprion onto SCG

The adsorption of MLT and CHP onto SCG reveals distinct differences in their behavior, reflecting the impact of their molecular structures on the adsorption processes. The kinetic studies demonstrated that MLT reaches adsorption equilibrium much faster (10 min) compared to CHP (1440 min). This rapid equilibrium for MLT can be attributed to its aliphatic nature, which likely facilitates easier interaction with the SCG surface. In contrast, the aromatic moiety of CHP may lead to stronger and more complex interactions, resulting in slower adsorption kinetics. The PFO kinetic model aligned better with the experimental data for both MLT and CHP, indicating a surface adsorption mechanism predominantly influenced by the adsorbate concentration. The Elovich model suggested that CHP adsorption was significantly slower than MLT, reinforcing the kinetic differences observed. Both MLT and CHP adsorption followed the Langmuir isotherm model, indicating monolayer adsorption on an energetically homogeneous surface. The maximum adsorption capacities (q_{max}) were relatively high for both pesticides, with temperature showing minimal impact on these values, and the Freundlich isotherm model showed n-values greater than 1, suggesting favorable adsorption but with a decreasing trend with increasing temperature. This implies reduced adsorbent affinity at higher temperatures, possibly due to weakened interactions or desorption effects. The thermodynamic analysis revealed contrasting behaviors for MLT and CHP adsorption. MLT adsorption was exothermic with a slight negative entropy change, suggesting that it is driven by enthalpic interactions, which become less favorable at higher temperatures. On the other hand, CHP adsorption was endothermic, with a significant positive entropy change, indicating an entropy-driven process that becomes more favorable at higher temperatures. MLT, being aliphatic, likely forms weaker, more easily disrupted bonds, while the aromatic structure of CHP leads to stronger, possibly π-π interactions. The reduction in AChE inhibition after adsorption indicates that SCG effectively removes MLT and CHP from the solution without forming more toxic by-products.

5.3. Material obtained by chemical activation of SCG with KOH – SCG material K

5.3.1. Characterization of SCG material K

SEM micrography of SCG material K (Figure 12a)) revealed that the activation using KOH transformed the previously spongy structure of SCG into a more plate-like form, yet it retained prominently heterogeneous pore distribution. Elemental analysis using EDX (Figure 12b)) revealed a dominant presence of C, O, and N, with 51.99 at.%, 35.87 at.%, and 7.35 at.%, respectively. In addition to these elements, as expected, K was also detected, constituting 4.26 at.% of the material.

The significant presence of K is attributed to the activation process with KOH, which introduces potassium ions into the carbon structure. The heterogeneous pore distribution observed post-activation can be linked to the effect of KOH, which not only increases the surface area but also creates a variety of pore sizes. The transformation from a spongy to a plate-like structure indicates a reorganization of the carbon matrix, likely enhancing the material's mechanical stability and adsorption properties.

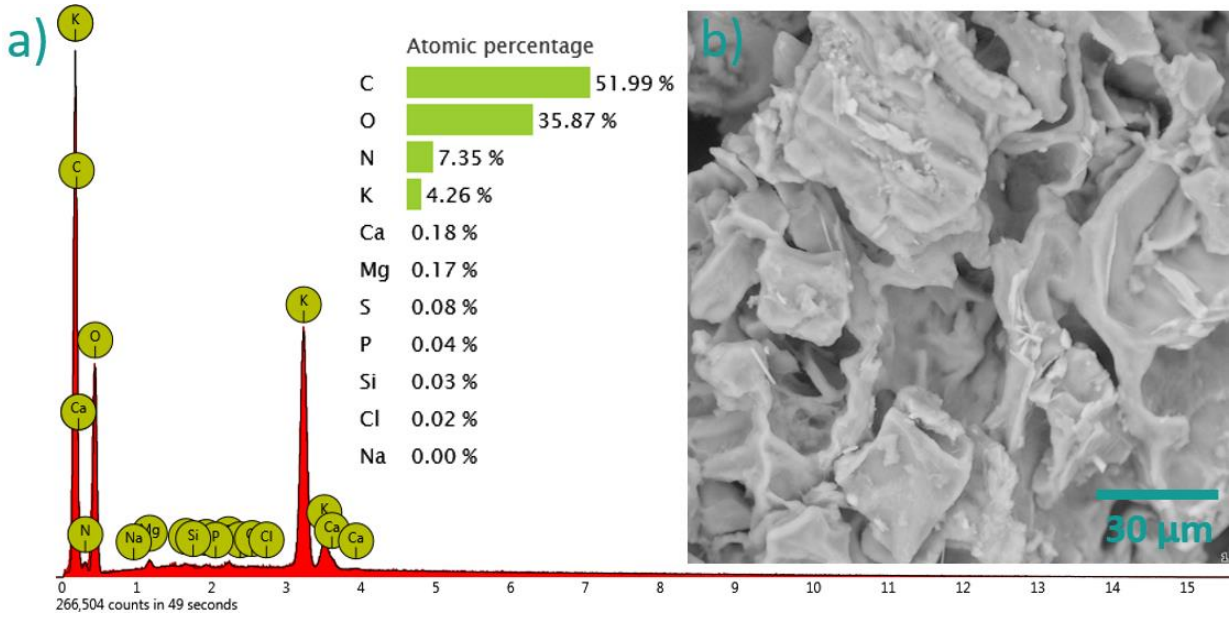

Figure 12. a) EDX spectrum and elemental composition in at.% of K b) SEM micrograph of K (magnification 2000×)

The FTIR spectrum of SCG material K (Figure 13) shows almost identical vibrations as a precursor, with some bands moving towards the lower wavenumber, indicating the chemical interaction between KOH and SCG, and a low-intensity band at 865 cm^{-1} appearing. The broad band at 3276 cm^{-1} is attributed to the stretching of O-H groups due to hydrogen bonding. The bands at 3010 cm^{-1}, 2924 cm^{-1}, and 2855 cm^{-1} indicate the presence of C-H bonds with carbon being sp^2 and sp^3 hybridized, respectively [88]. The sharp band at 1740 cm^{-1} corresponds to C=O stretch vibration, while the band at 1635 cm^{-1} is attributed to C=N stretch vibration [89]. The presence of a condensed aromatic system is assumed as the bands at 1558 cm^{-1} and 1452 cm^{-1} represent aromatic skeletal stretching and aromatic vibrations coupled with aromatic C-H in-plane vibrations, respectively. The band at 1376 cm^{-1} is assigned to aliphatic C-H stretch vibration. Deformation vibrations of C-N and C-O in secondary alcohols and C-

N are indicated by the bands at 1153 cm^{-1} and 1025 cm^{-1} [90]. Finally, the band at 1025 cm^{-1} is attributed to the coupling of aromatic C-H in-plane deformation vibrations and C-O stretch vibrations in primary alcohols [91]. The new band at 865 cm^{-1} is attributed to β-linkage in cellulose [92]. This band indicates that the activation process has introduced or preserved certain structural features of cellulose, which could impact the material's mechanical properties and interaction with various adsorbates.

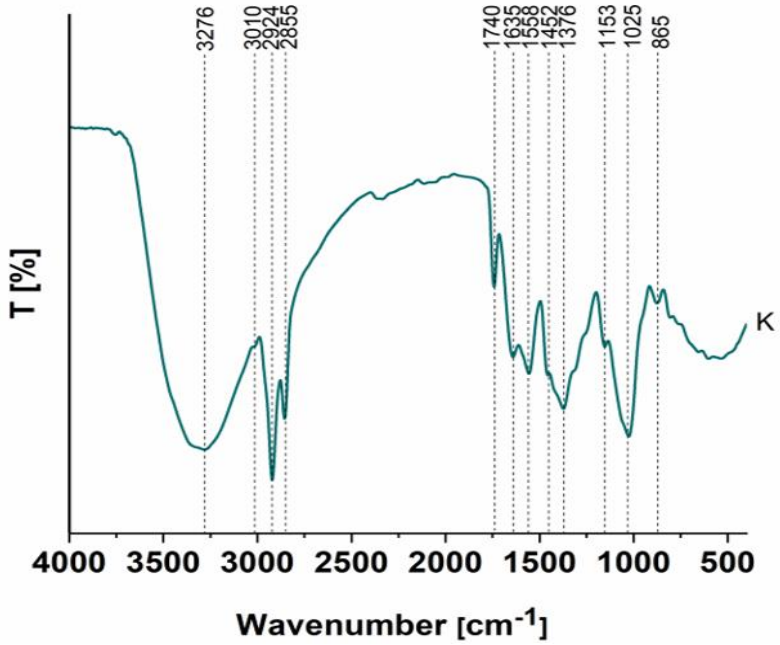

Figure 13. FTIR spectrum of SCG material K

Specific surface area and total pore volume of SCG are determined using BET. S_{BET} and V_{tot} were determined to be 1.532 $m^2\ g^{-1}$ and $1.695\times10^{-3}\ cm^3\ g^{-1}$.

5.3.2. Adsorption of MLT and CHP onto SCG material K

5.3.2.1. Kinetic studies of MLT and CHP adsorption onto SCG material K

Equilibrium between SCG material K and MLT is achieved after 90 minutes, while equilibrium for the adsorption of CHP is reached only after 400 minutes, which can clearly be seen in the graphical representations in Figure 14. The obtained parameters are given in Table 6. Both the PFO and PSO kinetic models fail to adequately describe the adsorption of these pesticides onto material K, as evidenced by the very low R^2 values obtained for both OPs. Although the rate constants k_1 and k_2 are higher for the adsorption of CHP, this does not align with experimental observations, and therefore these results will not be further considered. The Elovich kinetic model, on the other hand, provided a good fit with the experimental data and indicated a high initial adsorption rate of pesticides onto SCG material K, particularly for CHP, and very low desorption rates. This suggests that the initial adsorption process is rapid and efficient, but once adsorbed, the OPs are not easily desorbed. IPD kinetic model showed that the adsorption of MLT proceeds through two distinct stages, while the adsorption of CHP occurs through three separate stages. Throughout these stages, a gradual decrease in the k_{id} values is observed, while the C value increases until equilibrium of the adsorption process is reached. This indicates a complex adsorption mechanism involving multiple steps, likely including surface adsorption and pore diffusion.

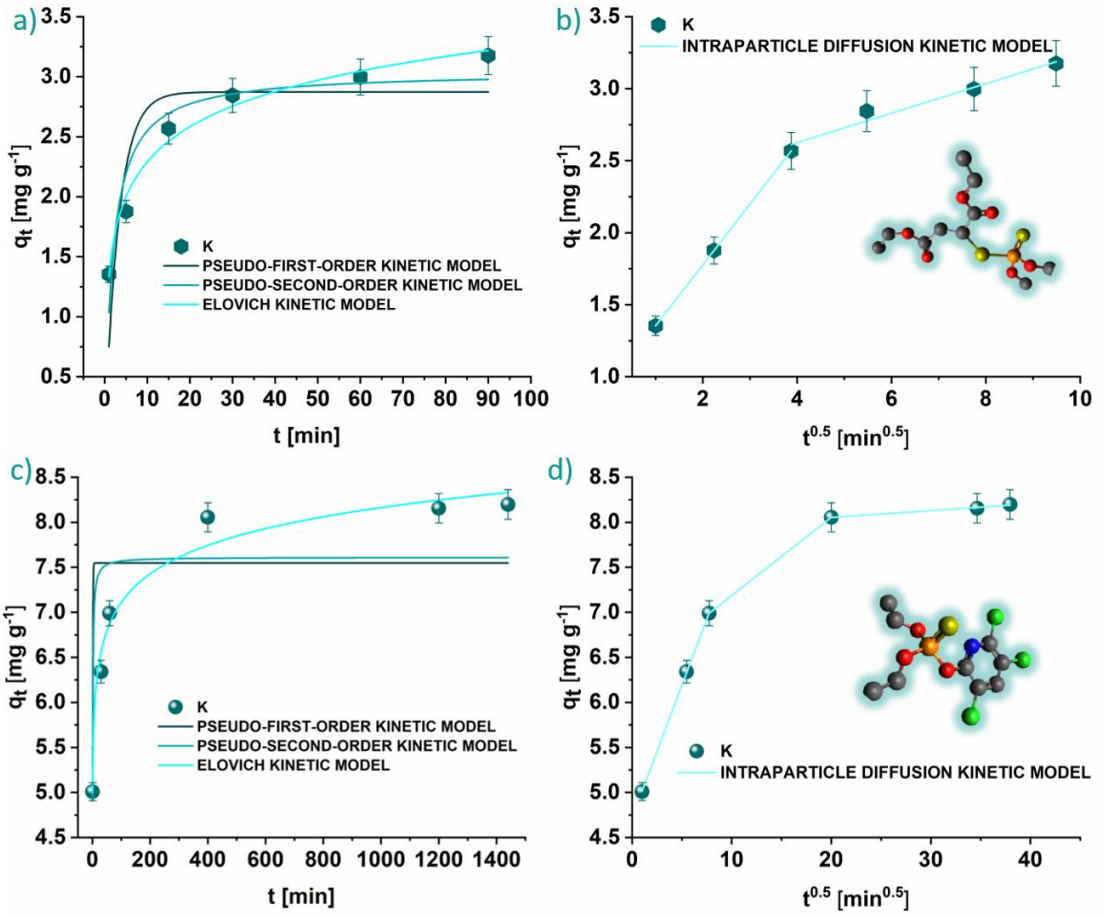

Figure 14. Graphical representations of kinetic models for MLT (a,b) and CHP (c,d) adsorption onto K

Table 6. Kinetic parameters of contaminants adsorption on K (1 mg mL^{-1}) at 25°C

OP→	**MLT**	**CHP**
	Pseudo-first-order kinetic model	
q_e ($mg\ g^{-1}$)	2.9 ±0.9	7 ±1
$k_1 \times 10^2$ (min^{-1})	0.30 ±0.08	1.1 ±0.7
χ^2	0.169	0.703
R^2	0.663	0.570
	Pseudo-second-order kinetic model	
q_e ($mg\ g^{-1}$)	3.0 ±0.5	7.6 ±0.8
$k_2 \times 10^2$ ($mg\ min^{-1}\ g^{-1}$)	17± 4	23 ±7
χ^2	0.064	0.612
R^2	0.871	0.625
	Elovich kinetic model	
α ($mg\ g^{-1}\ min^{-1}$)	9.48 ±0.03	25200 ±400
β ($g\ mg^{-1}$)	2.36 ±0.02	2.18 ±0.03
χ^2	0.010	0.045
R^2	0.981	0.972
	Intraparticle diffusion model	
I part		
C ($mg\ g^{-1}$)	0.931	4.719
k_{id} ($mg\ g^{-1}\ min^{-0.5}$)	0.422	0.294
R^2	1.000	0.999
II part		
C ($mg\ g^{-1}$)	2.216	6.320
k_{id} ($mg\ g^{-1}\ min^{-1}$)	0.102	0.086
R^2	0.948	--
III part		
C ($mg\ g^{-1}$)	--	7.900
k_{id} ($mg\ g^{-1}\ min^{-0.5}$)	--	0.008
R^2	--	0.968

5.3.2.2. Isotherm studies for MLT and CHP adsorption onto SCG material K

The graphical representations of the experimental data for MLT and CHP adsorption onto K, along with the corresponding isotherm model fits, are shown in Figure 15, and the calculated parameters, including R^2 and χ^2, are provided in Table 7.

The Freundlich isotherm shows that the adsorption processes are favorable. This is indicated by the Freundlich constant n, which is above 1 for both OPs, suggesting beneficial adsorption conditions. Notably, the n values indicate a more favorable adsorption scenario for CHP, implying a higher affinity of this OP towards the material K compared to MLT. Values of q_{max} values obtained from the Langmuir isotherm model supported this, as the values for CHP adsorption are higher than MLT adsorption. q_{max} gradually increases for MLT and decreases for CHP adsorption onto K. Therefore, the highest adsorption capacity for MLT obtained is at 35°C (15.0±0.1 mg g^{-1}), while for the CHP it is at 25°C (22.3±0.1 mg g^{-1}). The Temkin isotherm indicated a significantly stronger binding affinity of CHP to the material K compared to MLT. The Temkin constant K_T values were up to ten times greater for CHP, highlighting its stronger interaction with the adsorbent surface. Further supporting these findings, the Dubinin-Radushkevich isotherm model, which is used to distinguish between physisorption and chemisorption, revealed that the mean free energy of adsorption for CHP is consistently higher than that for MLT across all examined temperatures. However, since all the derived values are below 8 kJ mol^{-1}, the adsorption processes are classified as physisorption for both pesticides. This classification into physisorption indicates that the adsorption involves weak van der Waals forces, suggesting that no strong chemical bonds are formed during the adsorption of MLT and CHP onto material K.

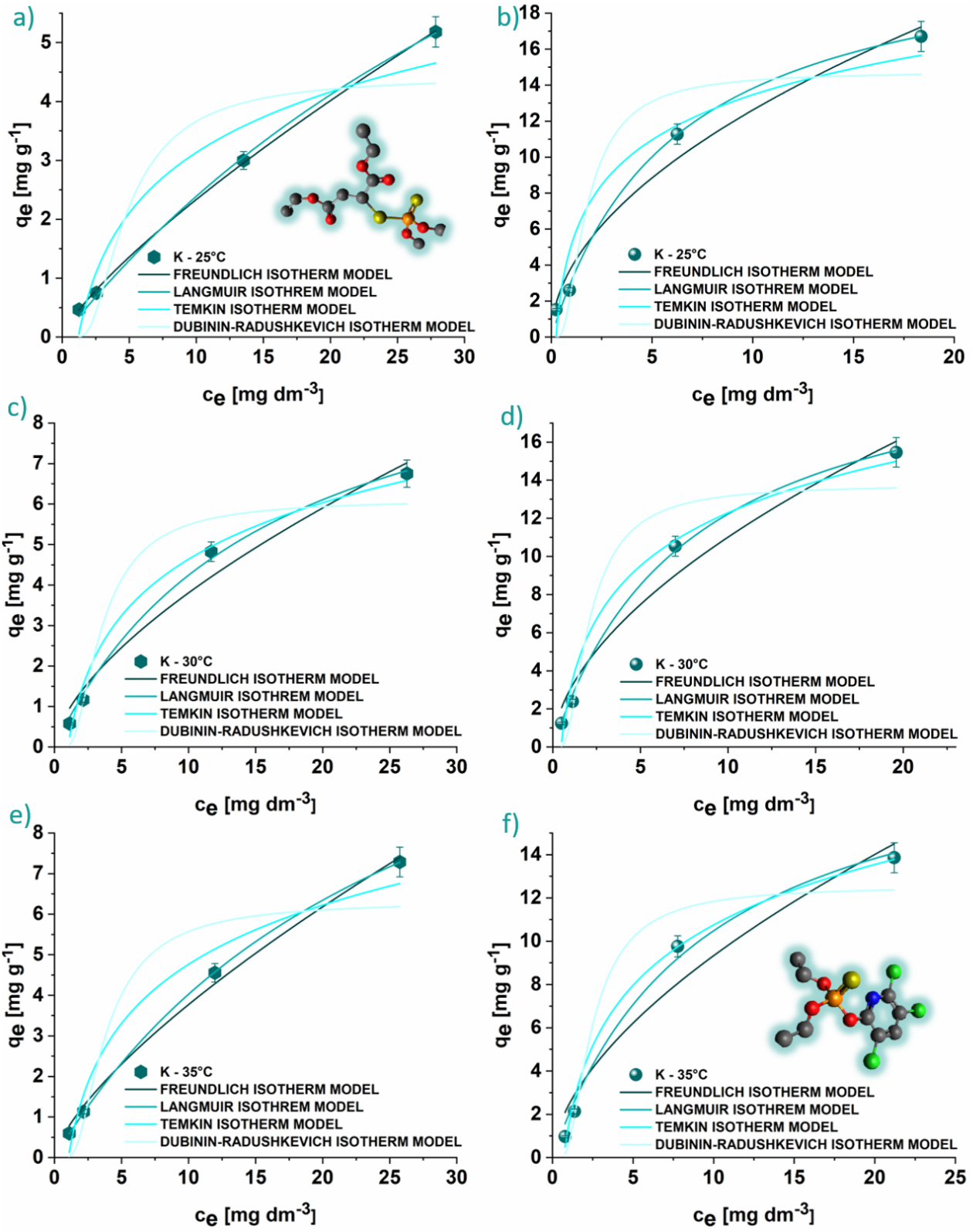

Figure 15. Graphical representations of isotherm models for MLT (a,c,e) and CHP (b,d,f) adsorption onto K (1 mg mL^{-1}) at 25°C (a,b), 30°C (c,d), and 35°C (e,f)

Table 7. Isotherm adsorption parameters of pesticides adsorption onto K (1 mg mL^{-1}) at 25°C, 30°C, and 35°C

	MLT			CHP		
T[°C]	**25**	**30**	**35**	**25**	**30**	**35**
Freundlich isotherm						
K_F $((dm^3\ mg^{-1})^{1/n})$	0.384 ±0.001	0.462 ±0.001	0.786 ±0.002	3.87 ±0.03	3.04 ±0.03	2.41 ±0.05
n	1.28 ±0.01	1.34 ±0.01	1.45 ±0.03	1.95 ±0.05	1.79 ±.04	1.70 ±0.05
χ^2	0.005	0.004	0.096	1.705	2.032	2.607
R^2	0.999	0.999	0.990	0.968	0.956	0.932
Langmuir isotherm						
$K_L \times 10^2$ $(dm^3\ mg^{-1})$	1.82 ±0.01	2.31 ±0.02	3.73 ±0.01	0.163 ±0.02	0.128 ±0.01	0.107 ±0.002
q_{max} $(mg\ g^{-1})$	13.5 ±0.1	14.0 ±0.1	15.0 ±0.1	22.3 ±0.1	21.7 ±0.1	20.3 ±0.1
χ^2	0.006	0.016	0.001	0.280	0.101	0.461
R^2	0.999	0.997	1.000	0.995	0.998	0.988
Temkin isotherm						
K_T $(dm^3\ mg^{-1})$	0.546 ±0.009	0.600 ±0.008	0.688 ±0.005	4.13 ±0.07	2.13 ±0.03	1.44 ±0.01
b_T $(J\ g\ mol^{-1}\ mg^{-1})$	1430 ±60	1400 ±60	1050 ±50	697 ±8	627 ±4	625 ±2
χ^2	0.451	0.450	0.429	4.367	1.238	0.300
R^2	0.908	0.914	0.955	0.917	0.973	0.992
D-R isotherm						
$K_{DR} \times 10^6$ $(mol^2\ J^{-2})$	3.4 ±0.7	2.7 ±0.6	2.2 ±0.4	0.56 ±0.03	0.76 ±0.01	0.994 ±0.006
q_{DR} $(mg\ g^{-1})$	4.4 ±0.9	4.6 ±0.9	6.3 ±0.7	14 ±1	13 ±1	12.5 ±0.7
E $(J\ mol^{-1})$	380 ±80	430 ±90	470 ±60	940 ±30	810 ±10	709 ±7
χ^2	1.807	1.913	2.757	6.286	4.739	2.846
R^2	0.632	0.636	0.710	0.880	0.897	0.925

5.3.2.3. Thermodynamic analysis of MLT and CHP adsorption onto SCG material K

To get insight into the thermodynamics of the process, Van't Hoff plots were constructed and analyzed (Figure 16). The obtained thermodynamic parameters are presented in Table 8. The thermodynamic analysis of OP adsorption onto SCG material K revealed behavior opposite to that observed with SCG. The adsorption of MLT onto SCG material K is characterized by an increase in system disorder and the positive enthalpy change, which indicates that the adsorption process is endothermic, requiring the input of heat from the surroundings. The spontaneity of this process is, therefore, driven by the increase in entropy, making the Gibbs free energy change negative. Conversely, the adsorption of CHP onto SCG material K is marked by a decrease in both entropy and enthalpy. The negative entropy change implies that the system becomes more ordered upon adsorption, and the negative enthalpy change indicates that the adsorption process is exothermic, releasing heat into the surroundings. The spontaneity of this adsorption is, therefore, driven by the enthalpic contribution, resulting in a negative Gibbs free energy change, thus making the process spontaneous.

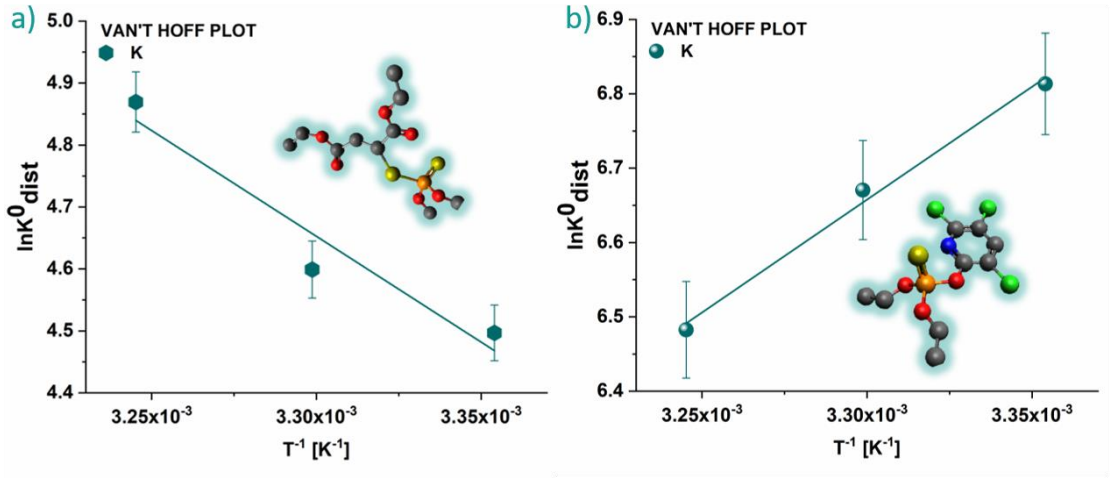

Figure 16. Van't Hoff plots for adsorption of MLT (a) and CHP (b) onto K

Table 8. Thermodynamic parameters for contaminants adsorption onto K (1 mg mL^{-1})

	ΔH^0 [kJ mol^{-1}]	ΔS^0 [J $mol^{-1}K^{-1}$]	ΔG^0 [kJ mol^{-1}]			R^2
T [°C] →			25	30	35	
MLT	28 ±2	130 ±10	-11 ±1	-12 ±1	-13 ±1	0.863
CHP	-25.2 ±0.03	-28.0 ±0.04	-17.0 ±0.3	-16.8 ±0.3	-16.6 ±0.3	0.985

5.3.3. Discussion on MLT and CHP adsorption onto SCG material K

The adsorption characteristics of MLT and CHP onto SCG material K, which was activated using KOH, reveal significant insights into the effects of chemical activation on adsorption properties and mechanisms. SEM micrography of SCG material K demonstrated a transformation from a spongy to a plate-like structure with heterogeneous pore distribution. This structural reorganization likely enhances mechanical stability and provides a diverse array of adsorption sites. EDX analysis confirmed a significant presence of C, O, and N, along with K, which was introduced during the KOH activation process. The presence of K is particularly notable as it suggests the incorporation of its ions into the carbon matrix, potentially influencing the adsorption sites and overall material properties. The FTIR spectrum of SCG material K showed similar vibrations to the precursor SCG, with some bands shifting to lower wavenumbers, indicating chemical interactions between KOH and SCG. The appearance of a low-intensity band at 865 cm^{-1}, attributed to β-linkage in cellulose, suggests that the activation process has preserved or introduced certain structural features of cellulose. This could impact the material's mechanical properties and interaction with various adsorbates. The presence of broad O-H stretching, C=O, C=N, and aromatic C-H vibrations indicate a complex chemical composition conducive to multiple adsorption interactions. The specific surface area and total pore volume of SCG material K were determined to be relatively low, indicating that despite the activation process, the material's surface area remains limited. However, the heterogeneous pore distribution could still provide a variety of adsorption sites critical for the adsorption process.

The adsorption equilibrium times for MLT and CHP onto SCG material K were markedly different, with MLT achieving equilibrium in 90 minutes and CHP in 400 minutes. The kinetic models revealed that both the PFO and PSO models failed to adequately describe the adsorption kinetics, likely due to the complex nature of the adsorption process. The Elovich model, however, provided a good fit, indicating a high initial adsorption rate and very low desorption rates, especially for CHP. This suggests that the initial adsorption is rapid and efficient, but the adsorbates are not easily desorbed once attached to the SCG material K.

The Freundlich isotherm model indicated favorable adsorption conditions for both MLT and CHP, with n-values greater than 1. The adsorption of CHP appeared more favorable than MLT, suggesting a higher affinity of SCG material K for CHP. The Langmuir isotherm model supported these findings, showing higher q_{max} values for CHP adsorption compared to MLT. The highest adsorption capacity for MLT was at 35°C (15.0 mg g^{-1}), while for CHP, it was at 25°C (22.3 mg g^{-1}), indicating temperature-dependent adsorption behaviors. The Temkin isotherm further highlighted the stronger binding affinity of CHP to SCG material K, with significantly higher K_T values compared to MLT. The Dubinin-Radushkevich isotherm model revealed that the mean free energy of adsorption for CHP was consistently higher than for MLT, although both remained below 8 kJ mol^{-1}, classifying the adsorption processes as physisorption. This suggests that weak van der Waals forces dominate the adsorption without the formation of strong chemical bonds.

5.4. Materials obtained by thermochemical conversion of SCG at 400°C – SCG 400 materials

5.4.1. Characterization of SCG 400 materials

The SEM micrographs in Figure 17 display the morphology of the materials. Even after the activation processes, the materials treated post-carbonization retained their porous, spongy-like structure, with pores unevenly distributed across the surfaces of all samples. This indicates that the original morphology of the raw SCG was preserved. In contrast, the material activated with KOH prior to carbonization showed a combination of the raw SCG morphology and needle-like structures, indicating that SCG reacted with KOH after elevating the temperature, as the material K did not exhibit visible differences.

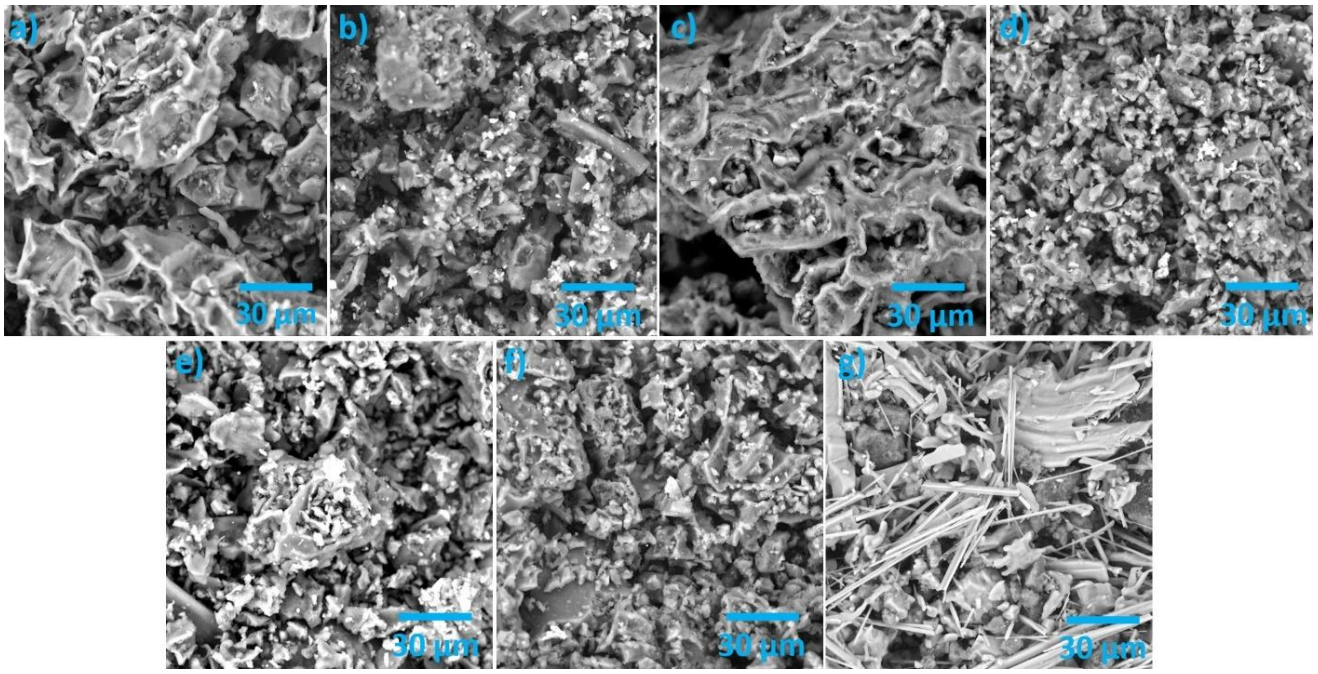

Figure 17. SEM micrographs of: a) 400; b) 400K; c) 400P; d) 400C; e) 400KC; f) 400PC; g) K400 (magnification 2000×)

The analysis of elemental compositions (Table 9) revealed varying atomic percentages of different elements in the carbon materials derived from SCG, indicating that the activation process significantly influenced the material's surface chemistry. All samples displayed high proportions of C, O, and N, consistent with the organic nature of the precursor. Carbon was the dominant element in all materials, accounting for over 65 at.% except in the case of K400, where it was nearly 40%. Notably, the oxygen at.% increased with activation, particularly in the material treated with KOH before carbonization. This suggests that the activation process primarily impacted the presence of surface oxygen functional groups. Materials activated with KOH and H_3PO_4 consistently showed the presence of K and P, respectively. Additionally, minor elements such as Mg and calcium Ca contributed to the elemental profile in varying but relatively small quantities.

Table 9. Elemental composition of the SCG materials thermochemically treated at 400°C

(at%)→	C	O	N	K	P	Mg	Ca	Na	Cl	S	Si
400	75.38	13.34	10.29	0.46	0.10	0.18	0.21	0.02	0.00		
400K	69.17	19.38	8.93	2.14	0.07	0.14	0.13	0.02	0.01		
400P	68.75	19.21	8.91	0.44	2.32	0.16	0.21	0.00	0.00		
400C	73.86	13.56	11.56	0.55	0.08	0.16	0.24	0.00	0.00		
400KC	70.50	17.52	9.02	2.44	0.11	0.14	0.19	0.02	0.02	0.11	0.01
400PC	65.12	22.56	9.92	0.28	1.63	0.16	0.15	0.05	0.01	0.03	0.05
K400	39.73	41.76	5.00	13.22	0.07	0.08	0.00	0.04	0.02	0.03	0.05

The FTIR spectra of all materials are shown in Figure 18. It is evident that the thermochemical conversion of SCG greatly influenced the surface chemistry, as the obtained spectra differ from the SCG FTIR spectrum presented in Figure. Physical activation did not further alter the functional groups on the material's surface, as the FTIR spectra of physically activated and non-activated materials are predominantly identical. However, introducing chemical activation with KOH and H_3PO_4 induced noticeable changes.

The bands present in the spectra correspond to specific vibrations. The vibrations at 1574 cm^{-1} and 1372 cm^{-1}, which appear in all material spectra, are attributed to the stretching of the C=C bonds in aromatic rings and C-H in-plane deformation vibrations, respectively. In addition to these, chemical activation with either KOH or H_3PO_4 introduces bands at 1391 cm^{-1} and 970 cm^{-1}, corresponding to the stretching and in-plane vibrations of the acetate group and C-O bending vibrations, respectively [93]. Moreover, KOH chemical activation results in the presence of more functional groups on the material's surface. KOH-activated materials display additional bands at 1623 cm^{-1}, 1004 cm^{-1}, 825 cm^{-1}, and 696 cm^{-1}. The vibration at 1623 cm^{-1} is assigned to asymmetric stretches of carboxylate anions, while the band at 1004 cm^{-1} signifies C-OH bending vibrations [90]. The C-H bending vibrations in the aromatic ring are observed at 825 cm^{-1} and 696 cm^{-1}. Materials activated with H_3PO_4 show an additional band at 1075 cm^{-1}, attributed to the coupling of aromatic C-H in-plane deformation vibrations and C-O stretch vibrations in primary alcohols [94].

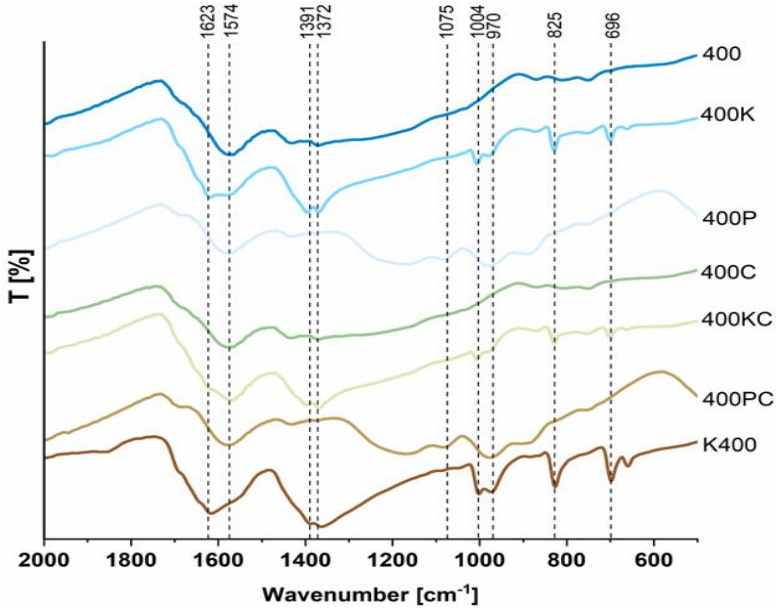

Figure 18. FTIR spectra of the SCG materials thermochemically treated at 400°C

Zeta potential measurements were carried out to evaluate the charge characteristics of the materials and determine their respective isoelectric points (Figure 19). The isoelectric points for 400, 400K, 400P, 400C, 400KC, 400PC, and K400 were determined to be 3.57, 1.87, 3.87, 5.36, 3.48, 3.67, and 3.99, respectively. Considering that the initial pH value of all materials suspended in 50% ethanol was 6, it can be concluded that all materials exhibited a negatively charged surface under the experimental conditions applied for the adsorption measurements.

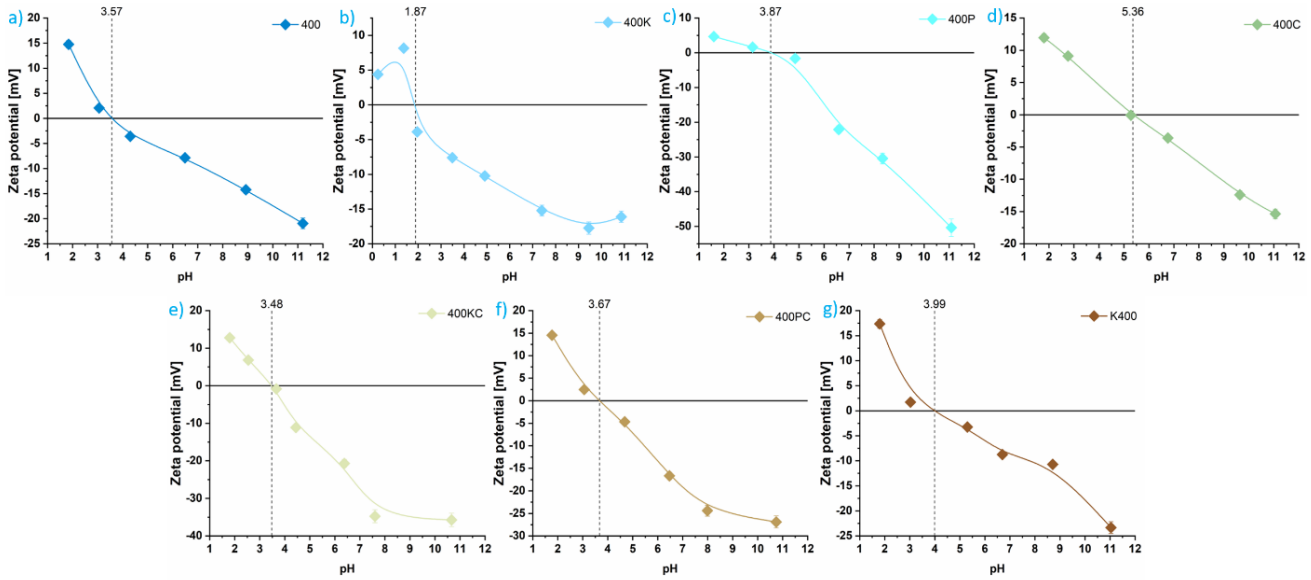

Figure 19. Dependence of zeta potential of pH value of the suspension with indicated IEP for materials: a) 400; b) 400K; c) 400P; d) 400C; e) 400KC; f) 400PC; g) K400

The results of BET measurements and total pore volume determination, as summarized in Table 10, reveal that all the samples have relatively small specific surface areas (S_{BET}) and total pore volumes (V_{tot}). This outcome is expected, given that the carbonization was performed at low temperatures, which typically does not facilitate the development of a well-defined pore system. Notably, the K400 sample exhibits the largest S_{BET} and V_{tot} values among the series. However, there is no straightforward correlation between the specific surface area and the pore volume across the different samples. This indicates that factors other than the pore volume, such as the distribution and size of the pores, may also play significant roles in determining the specific surface area. According to this analysis, it can be assumed that activation with KOH and CO_2 enhances the specific surface area through enlargement of the pores, while the activation with H_3PO_4 infected the development of smaller pores.

Table 10. Specific surface areas by BET method (S_{BET}) and total pore volumes (V_{tot}) of the SCG materials thermochemically treated at 400°C

Sample	S_{BET} [$m^2\ g^{-1}$]	$V_{tot} \times 10^3$ [$cm^3\ g^{-1}$]
400	2.38	3.1
400K	3.52	8.6
400P	4.28	2.4
400C	6.50	7.9
400KC	3.96	4.9
400PC	5.63	6.7
K400	9.38	25.4

5.4.2. Adsorption of MLT and CHP onto SCG 400 materials

5.4.2.1. Kinetic studies of MLT and CHP adsorption onto SCG 400 materials

The equilibrium between MLT and the materials is reached after 90 minutes, as demonstrated by graphical representations of kinetic models (Figure 20). The obtained parameters are given in Table 11. In the case of MLT adsorption onto materials 400, 400C, and K400, the experimental data fit better with the PSO kinetic model, suggesting that the rate of adsorption is influenced by the concentration of both the material and the pesticide. Values of q_e obtained from PSO are similar for all three materials and are 5.1±0.2 mg g^{-1}, 4.6±0.4 mg g^{-1}, and 5.31±0.08 mg g^{-1}, for 400, 400C, and K400, respectively. On the other hand, k_2 values differ and indicate that the adsorption of MLT is the fastest onto material 400. The Elovich kinetic parameters reveal that for MLT adsorption, the initial rate of adsorption is larger than the desorption rate, which explains the rapid achievement of equilibrium. The IPD kinetic model shows three stages of adsorption for MLT onto investigated materials, with a noticeable decrease in k_{id} values through stages, indicating a slowing down of the adsorption process and eventually reaching the equilibrium.

From graphical representations of kinetic models for CHP adsorption onto materials, it is observed that the equilibrium is achieved after 1440 minutes (Figure 21). The obtained parameters are given in Table 12. The adsorption of CHP fits well with both the PFO and PSO kinetic models as indicated by R^2 values greater than 0.9 and low χ^2 values, suggesting that the adsorption process can be complex and might consist of multiple steps, where different steps dominate under different conditions. The good fit for both models indicates the complexity of the adsorption process, which involves multiple steps where different steps may dominate under different conditions. Particularly for CHP adsorption onto K400, the experimental data fit better to the PSO kinetic model, indicating that the adsorption rate depends on the concentrations of both the material and the pesticide. The qe values obtained using both kinetic models are similar, with PFO providing slightly lower values in all cases. K400 exhibited the highest equilibrium concentration for CHP adsorption, at 11.2±0.07 mg g^{-1}. The k_1 and k_2 values suggest that the adsorption rate increases with the level of activation. 400 has the lowest values of k_1 and k_2, increasing with the level of activation, reaching the highest values for combined activation, especially 400PC. The Elovich kinetic parameters indicated that the adsorption of CHP continues for an extended period after the initial adsorption as the parameter β is higher than, suggesting simultaneous adsorption and desorption of CHP molecules, thus extending the time required to reach equilibrium. The IPD kinetic model reveals three stages (external diffusion, intraparticle diffusion, and equilibrium stage) for CHP adsorption onto 400K, 400C, and 400PC, unlike other cases, which show two stages (rapid initial adsorption and slower equilibrium stage).

The obtained results cannot be correlated with the BET analysis of the materials, indicating that the porosity of the materials is not the main factor for the adsorption of these pesticides.

For consistency, further adsorption experiments will be performed with the equilibrium time of 1440 min, as the adsorption of both pesticides reaches equilibrium in that time.

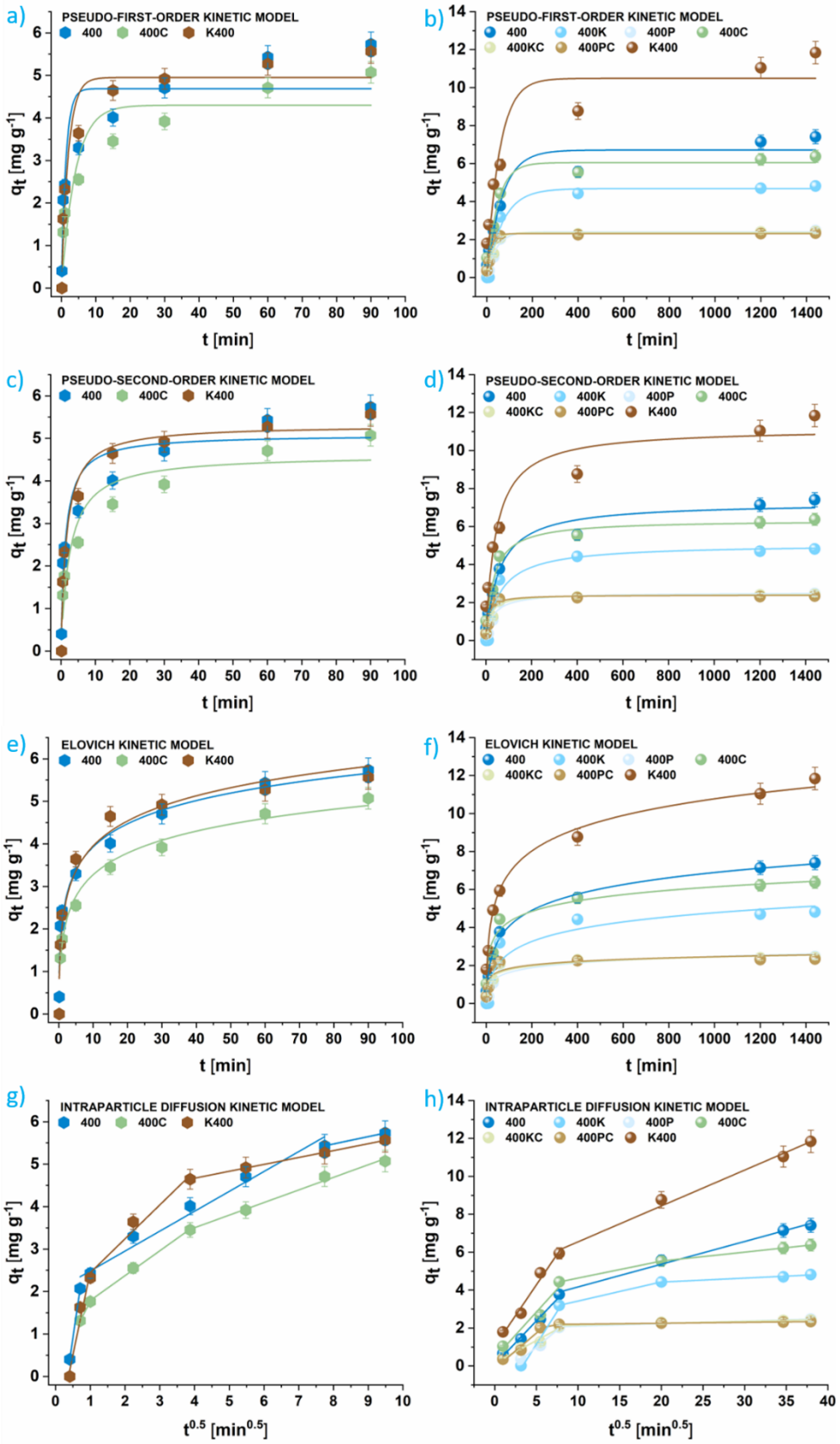

Figure 20. Graphical representation of kinetic models for MLT (left) and CHP (right) adsorption onto SCG materials thermochemically treated at 400°C: PFO (a,b), PSO (c,d), Elovich (e,f) and IPD (g,h)

Table 11. Kinetic parameters of MLT (5×10^{-5} mol dm^{-3}) adsorption onto SCG 400 materials (1 mg mL^{-1})

Material →	400	400C	K400
Pseudo-first order			
q_e ($mg\ g^{-1}$)	4.7 ±0.6	4.3 ±0.8	4.95 ±0.06
$k_1 \times10^2$ (min^{-1})	77 ±7	25 ±6	50.0 ±0.5
χ^2	0.688	0.608	0.328
R^2	0.793	0.705	0.918
Pseudo-second order			
q_e ($mg\ g^{-1}$)	5.1 ±0.2	4.6 ±0.4	5.31 ±0.08
$k_2 \times10^2$ ($mg\ min^{-1}\ g^{-1}$)	15 ±2	8.5 ±0.4	11.9 ±0.5
χ^2	0.376	0.310	0.129
R^2	0.887	0.850	0.968
Elovich model			
α ($mg\ g^{-1}\ min^{-1}$)	11.3 ±0.3	5.91 ±0.05	8.52 ±0.06
β ($g\ mg^{-1}$)	1.27 ±0.04	1.34 ±0.03	1.17 ±0.05
χ^2	0.107	0.031	0.183
R^2	0.968	0.985	0.954
Intraparticle diffusion model			
I part			
C ($mg\ g^{-1}$)	-1.874	0.212	0.931
k_{id} ($mg\ g^{-1}\ min^{-0.5}$)	5.580	1.553	0.423
R^2	--	--	1.000
II part			
C ($mg\ g^{-1}$)	2.015	1.204	2.216
k_{id} ($mg\ g^{-1}\ min^{-0.5}$)	0.469	0.585	0.102
R^2	0.967	0.996	0.948
III part			
C ($mg\ g^{-1}$)	4.090	2.316	4.020
k_{id} ($mg\ g^{-1}\ min^{-0.5}$)	0.173	0.297	0.162
R^2	--	0.988	0.999

Table 12. Kinetic parameters of CHP (5×10^{-5} mol dm^{-3}) adsorption onto SCG 400 materials (1 mg mL^{-1})

Material →	400	400K	400P	400C	400KC	400PC	K400
Pseudo-first order							
q_e ($mg\ g^{-1}$)	6.71 ±0.06	4.68 ±0.03	2.41 ±0.04	6.05 ±0.07	2.36 ±0.08	2.31 ±0.02	10 ±1
$k_1\times10^2$ (min^{-1})	1.75 ±0.07	1.80 ±0.04	2.37 ±0.04	2.11 ±0.07	3.39 ±0.09	5.60 ±0.03	1.8 ±0.2
χ^2	0.504	0.180	0.037	0.317	0.055	0.020	2.005
R^2	0.932	0.962	0.959	0.930	0.916	0.970	0.870
Pseudo-second order							
q_e ($mg\ g^{-1}$)	7.27 ±0.03	5.08 ±0.05	2.53 ±0.07	6.34 ±0.06	2.44 ±0.07	2.40 ±0.07	11.2 ±0.07
$k_2\times10^2$ ($mg\ min^{-1}\ g^{-1}$)	0.239 ±0.004	0.312 ±0.006	1.28 ±0.05	0.479 ±0.005	2.37 ±0.08	3.84 ±0.09	0.248 ±0.008
χ^2	0.247	0.243	0.061	0.274	0.045	0.045	1.209
R^2	0.966	0.949	0.933	0.940	0.931	0.932	0.922
Elovich model							
α ($mg\ g^{-1}\ min^{-1}$)	0.308 ±0.001	0.14 ±0.01	0.31 ±0.05	1.68 ±0.05	1.3 ±0.1	2.4 ±0.3	0.913 ±0.002
β ($g\ mg^{-1}$)	0.799 ±0.001	1.0 ±0.1	2.7 ±0.3	1.24 ±0.04	3.4 ±0.1	3.7 ±0.4	0.583 ±0.002
χ^2	0.069	0.476	0.129	0.190	0.066	0.161	0.334
R^2	0.991	0.900	0.857	0.958	0.898	0.758	0.978
Intraparticle diffusion model							
I part							
C ($mg\ g^{-1}$)	0.073	-2.329	-0.821	0.424	0.159	-0.133	1.042
k_{id} ($mg\ g^{-1}\ min^{-0.5}$)	0.461	0.695	0.363	0.484	0.237	0.373	0.647
R^2	0.988	0.976	0.991	0.959	0.963	0.954	0.979
II part							
C ($mg\ g^{-1}$)	2.969	2.416	1.967	3.737	2.056	1.576	4.653
k_{id} ($mg\ g^{-1}\ min^{-0.5}$)	0.120	0.101	0.013	0.090	0.010	0.080	0.189
R^2	0.992	1.000	0.947	1.000	0.955	1.000	0.988
III part							
C ($mg\ g^{-1}$)		4.014		4.592		2.160	
k_{id} ($mg\ g^{-1}\ min^{-0.5}$)		0.021		0.047		0.005	
R^2		0.981		1.000		0.993	

5.4.2.2. Isotherm studies of MLT and CHP adsorption onto SCG 400 materials

The graphical representations of the experimental data for MLT and CHP adsorption onto SCG materials thermochemically treated at 400°C, along with the corresponding isotherm model fits, are shown in Figure 21 (MLT) and Figure 22 (CHP). The calculated parameters, including R^2 and χ^2, are provided in Table 13 (MLT) and Tables 14 and 15 (CHP).

According to the obtained R^2 and χ^2 values, the experimental data aligns well with both Freundlich and Langmuir isotherm models for MLT and CHP adsorption at all investigated temperatures. However, the adsorption processes are better described by the Langmuir isotherm model, except for MLT adsorption at 35°C, where the Freundlich model provides a better fit. This suggests that adsorption occurs in well-defined and energetically homogeneous sites.

For CHP adsorption, the most favorable conditions are observed on K400 at 25°C, while at higher temperatures, 400PC exhibits more favorable adsorption according to the n parameter of the Freundlich isotherm model. In contrast, MLT adsorption is most favorable on 400C at 25°C and 30°C, but at 35°C, the favorability shifts to 400. As the adsorption temperature increases, the n parameter increases for CHP adsorption onto 400, 400P, and 400PC, and for MLT adsorption onto 400 and K400, while it decreases in other cases.

Increasing the adsorption temperature generally negatively affects the adsorption capacity of all materials for CHP and MLT, except for CHP adsorption onto SCG 400 materials activated with KOH. At 25°C, all activation processes yield lower adsorption capacity for just carbonized material (q_{max} = 19.4±0.4 mg g^{-1}). However, with increasing adsorption temperature, the highest adsorption capacity for CHP is observed for K400 at 35°C (q_{max} = 29.4±0.1 mg g^{-1}). For MLT, the highest q_{max} value across the temperature range is for K400, with the peak value at 25°C (q_{max} = 11.2±0.2 mg g^{-1}).

The K_T parameter from the Temkin isotherm model indicates that pesticide molecules bind most strongly to 400 and 400C materials, with weaker binding observed for other materials. The interaction strength between CHP and the materials decreases with increasing adsorption temperature, whereas the interaction strength between MLT and 400 increases. Although the Langmuir isotherm model suggests chemisorption, this can be ruled out in this case. The Temkin and Dubinin-Radushkevich isotherm models suggest that the adsorption of both pesticides onto these materials is primarily physisorption, as indicated by the predicted heat of adsorption and mean free adsorption energy values being lower ($E << 8$ kJ mol^{-1}) in all cases.

Isotherm studies reveal that at lower thermochemical conversion temperatures of SCG, post-carbonization activation decreases the material's performance, whereas KOH activation prior to carbonization enhances the material's adsorption properties.

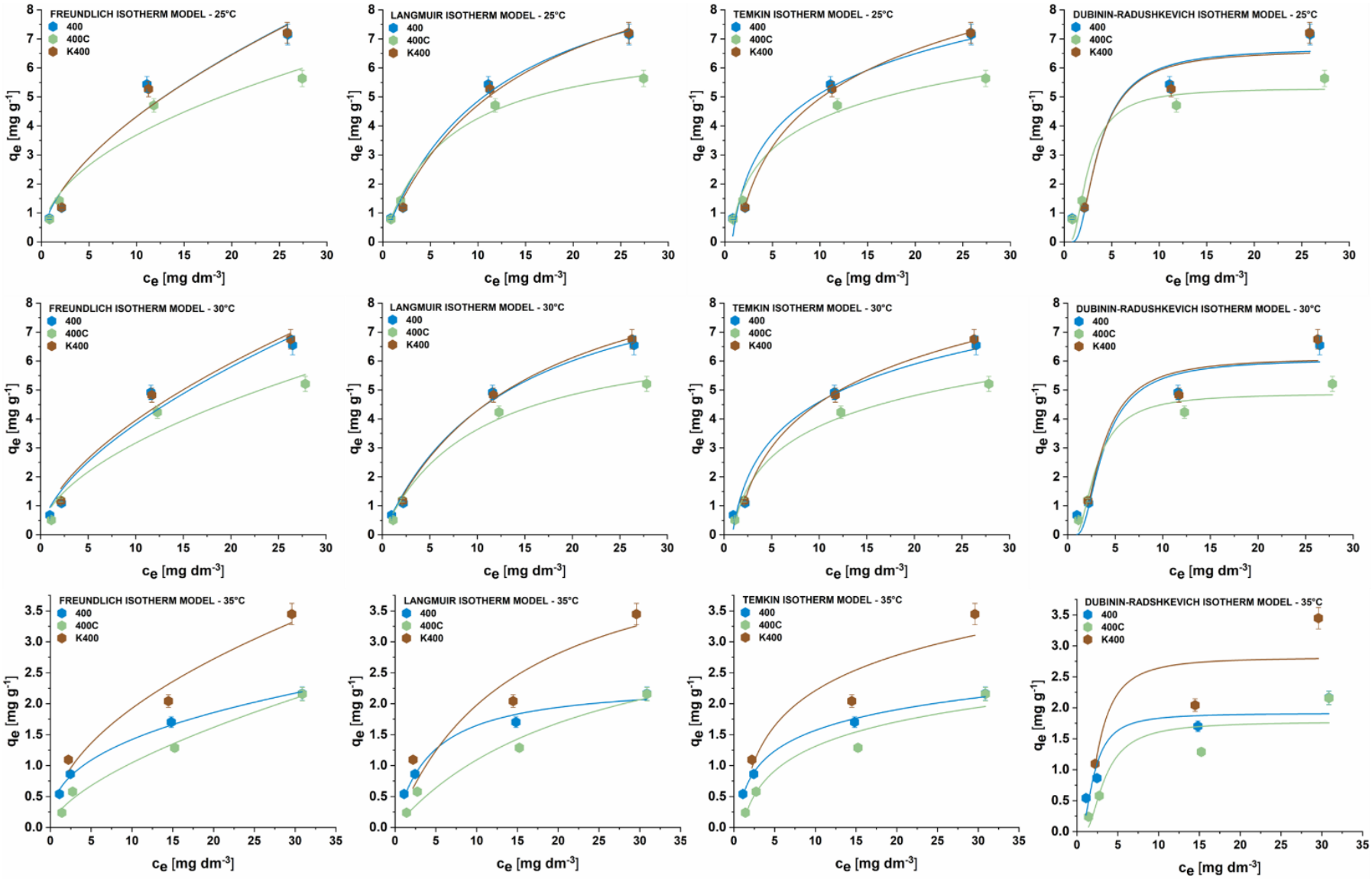

Figure 21. Graphical representations of experimental data for MLT adsorption onto SCG 400 materials fittings isotherm models at 25°C (top row), 30°C (middle row), and 35°C (bottom row)

Table 13. Isotherm adsorption parameters of MLT adsorption onto SCG 400 materials (1 mg mL^{-1}) at 25°C, 30°C, and 35°C

Material →	400			400C			K400		
	25	30	35	25	30	35	25	30	35
Freundlich isotherm									
K_F $((mg\ g^{-1})(dm^3\ g^{-1})^{1/n})$	1.14 ±0.05	0.958 ±0.005	0.584 ±0.001	1.22 ±0.06	0.903 ±0.008	0.245 ±0.002	1.14 ±0.07	1.02 ±0.05	0.608 ±0.008
n	1.72 ±0.07	1.66 ±0.04	2.59 ±0.01	2.08 ±0.08	1.83 ±0.07	1.56 ±0.02	1.73 ±0.08	1.71 ±0.06	2.00 ±0.09
χ^2	0.607	0.458	0.005	0.406	0.410	0.012	0.804	0.472	0.130
R^2	0.938	0.945	0.991	0.929	0.922	0.983	0.915	0.941	0.907
Langmuir isotherm									
$K_L \times 10^2$ $(dm^3\ mg^{-1})$	8.42 ±0.03	7.51 ±0.02	23.1 ±0.3	14.7 ±0.1	10.1 ±0.1	4.14 ±0.05	7.27 ±0.03	6.73 ±0.01	6.8 ±0.6
q_{max} $(mg\ g^{-1})$	10.6 ±0.4	10.0 ±0.2	2.36 ±0.04	7.15 ±0.03	7.23 ±0.03	3.72 ±0.04	11.2 ±0.2	10.6 ±0.1	4.9 ±0.5
χ^2	0.154	0.094	0.014	0.027	0.065	0.035	0.150	0.050	0.388
R^2	0.984	0.989	0.975	0.995	0.988	0.951	0.984	0.994	0.723
Temkin isotherm									
K_T $(dm^3\ mg^{-1})$	1.33 ±0.06	1.59 ±0.04	2.60 ±0.01	1.71 ±0.02	1.15 ±0.01	0.986 ±0.07	0.7823 ±0.0001	0.783 ±0.001	1.5 ±0.2
b_t $(J\ g\ mol^{-1}mg^{-1})$	1270 ±50	1340 ±50	5220 ±10	1690 ±20	1640 ±10	4400 ±80	1048 ±1	1140 ±10	3100 ±300
χ^2	0.581	0.334	0.004	0.098	0.039	0.056	0.002	0.010	0.358
R^2	0.941	0.960	0.994	0.983	0.993	0.922	1.000	0.999	0.744
Dubinin-Radushkevich isotherm									
$K_{DR} \times 10^6$ $(mol^2\ J^{-2})$	1.98 ±0.06	2.08 ±0.06	0.75 ±0.05	1.07 ±0.04	1.42 ±0.04	1.7 ±0.4	2.0 ±0.2	1.9 ±0.2	1.1 ±0.6
q_{DR} $(mg\ g^{-1})$	6.69 ±0.07	6.08 ±0.08	1.9 ±0.5	5.31 ±0.05	4.89 ±0.04	1.8 ±0.5	6.6 ±0.2	6.1 ±0.3	3 ±1
E $(kJ\ mol^{-1})$	503 ±5	491 ±7	820 ±60	682 ±4	593 ±5	540 ±80	500 ±30	510 ±50	700 ±400
χ^2	0.728	0.602	0.111	0.376	0.219	0.178	1.139	1.228	0.899
R^2	0.926	0.927	0.801	0.934	0.958	0.752	0.879	0.847	0.358

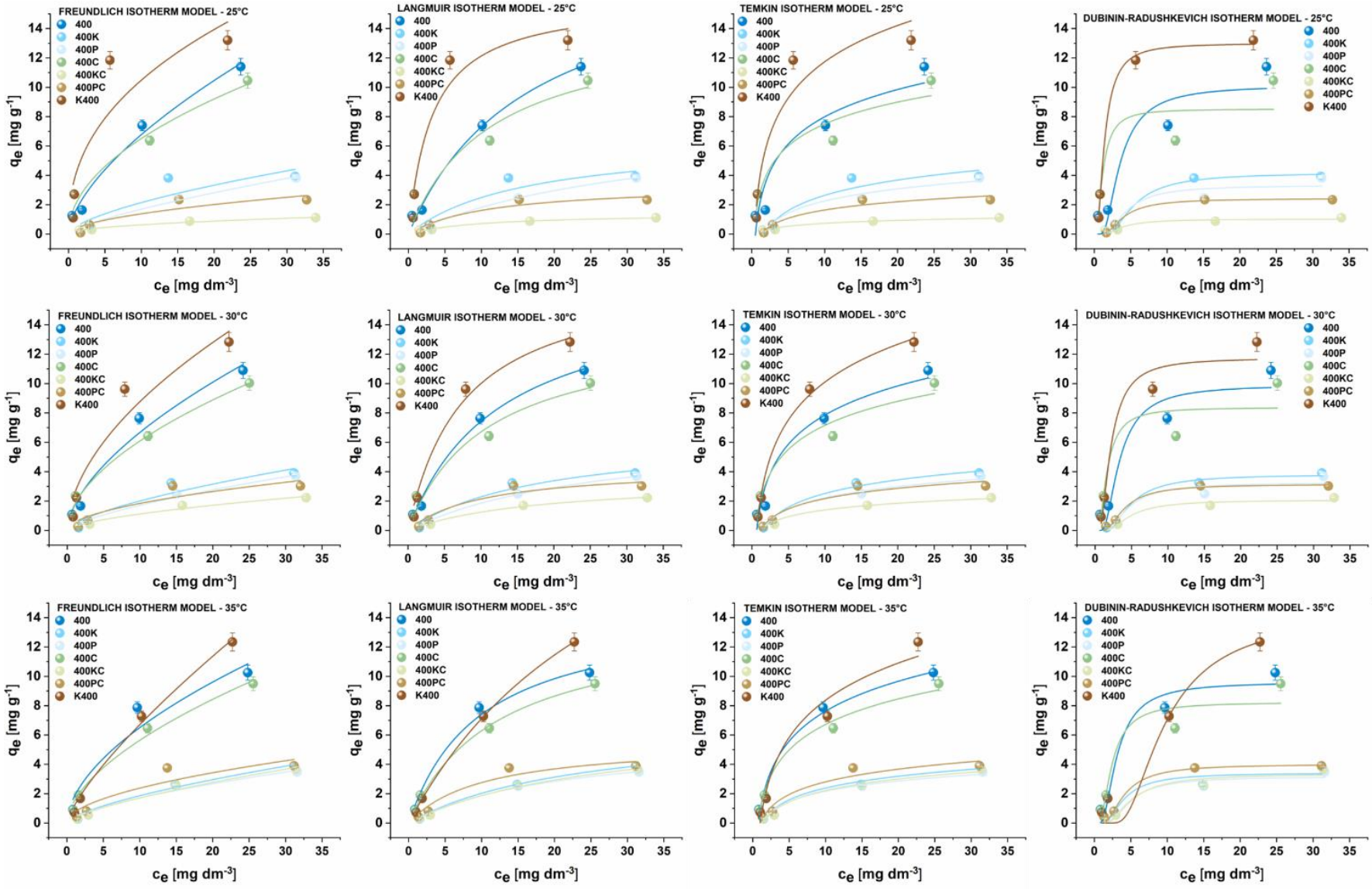

Figure 22. Graphical representations of experimental data for CHP adsorption onto SCG 400 materials fittings isotherm models at 25°C (top row), 30°C (middle row), and 35°C (bottom row)

Table 14. Isotherm adsorption parameters of CHP adsorption onto SCG 400 materials (1 mg mL^{-1}) at 25°C, 30°C, and 35°C

Material →	400			400K			400P			400C		
	25	30	35	25	30	35	25	30	35	25	30	35
Freundlich isotherm												
K_F $((mg\ g^{-1})(dm^3\ g^{-1})^{1/n})$	1.60 ±0.02	1.70 ±0.04	1.78 ±0.06	0.50 ±0.05	0.45 ±0.02	0.399 ±0.002	0.312 ±0.005	0.348 ±0.005	0.390 ±0.003	2.06 ±0.04	1.74 ±0.03	1.48 ±0.02
n	1.60 ±0.04	1.67 ±0.04	1.78 ±0.06	1.6 ±0.3	1.5 ±0.2	1.49 ±0.02	1.36 ±0.03	1.45 ±0.03	1.55 ±0.03	2.00 ±0.04	1.89 ±0.03	1.72 ±0.02
χ^2	0.483	0.906	1.856	1.188	0.426	0.052	0.061	0.047	0.065	0.716	0.227	0.262
R^2	0.980	0.960	0.912	0.728	0.878	0.981	0.978	0.982	0.971	0.958	0.986	0.984
Langmuir isotherm												
$K_L \times 10^2$ $(dm^3\ mg^{-1})$	6.01 ±0.01	8.03 ±0.01	10.2 ±0.2	6.3 ±0.2	5.42 ±0.06	4.17 ±0.01	2.92 ±0.01	3.71 ±0.01	4.68 ±0.01	9.0 ±0.3	9.27 ±0.05	8.34 ±0.01
q_{max} $(mg\ g^{-1})$	19.4 ±0.4	16.7 ±0.1	14.7 ±0.4	6.5 ±0.5	6.50 ±0.05	6.86 ±0.01	8.03 ±0.02	6.86 ±0.01	5.85 ±0.01	14 ±1	13.9 ±0.4	13.85 ±0.01
χ^2	0.295	0.185	0.421	0.733	0.191	0.011	0.024	0.003	0.013	2.166	0.763	0.058
R^2	0.988	0.992	0.980	0.832	0.945	0.996	0.991	0.999	0.994	0.874	0.955	0.996
Temkin isotherm												
K_T $(dm^3\ mg^{-1})$	2.0 ±0.2	1.55 ±0.07	1.33 ±0.03	0.587 ±0.006	0.654 ±0.005	0.780 ±0.002	0.660 ±0.003	0.739 ±0.003	0.851 ±0.005	3.3 ±0.2	2.07 ±0.05	1.45 ±0.02
b_t $(J\ g\ mol^{-1}mg^{-1})$	940 ±20	882 ±7	855 ±4	1680 ±70	1880 ±20	2170 ±30	2110 ±30	2270 ±30	2490 ±40	1200 ±100	1070 ±40	1000 ±20
χ^2	3.380	1.561	0.652	0.443	0.083	0.051	0.063	0.069	0.107	1.817	0.783	0.282
R^2	0.858	0.931	0.969	0.900	0.976	0.982	0.978	0.973	0.952	0.895	0.953	0.983
Dubinin-Radushkevich isotherm												
$K_{DR} \times 10^6$ $(mol^2\ J^{-2})$	1.9 ±0.2	1.70 ±0.07	1.51 ±0.05	4.22 ±0.01	3.45 ±0.02	2.4 ±0.3	2.9 ±0.2	3.0 ±0.2	3.3 ±0.1	0.30 ±0.04	0.51 ±0.08	0.96 ±0.05
q_{DR} $(mg\ g^{-1})$	10 ±1	9.91 ±0.08	9.61 ±0.06	4.18 ±0.03	3.81 ±0.02	3.4 ±0.4	3.3 ±0.2	3.2 ±0.3	3.2 ±0.1	8.5 ±0.3	8.4 ±0.5	8.2 ±0.4
E $(J\ mol^{-1})$	510 ±50	542 ±8	576 ±5	344 ±1	381 ±2	450 ±40	420 ±30	410 ±50	390 ±20	1300 ±200	990 ±70	720 ±40
χ^2	3.462	2.220	1.108	0.028	0.052	0.328	0.351	0.285	0.234	4.164	3.011	2.085
R^2	0.854	0.902	0.948	0.994	0.985	0.882	0.875	0.888	0.895	0.759	0.821	0.871

Table 15. Continuation of Table 14

Material →	400KC			400PC			K400		
	25	30	35	25	30	35	25	30	35
Freundlich isotherm									
K_F $((mg\ g^{-1})(dm^3\ g^{-1})^{1/n})$	0.208 ±0.003	0.275 ±0.04	0.345 ±0.04	0.40 ±0.06	0.55 ±0.05	0.71 ±0.05	4.1 ±0.5	2.50 ±0.09	1.16 ±0.01
n	2.07 ±0.03	1.64 ±0.04	1.44 ±0.03	1.9 ±0.2	1.9 ±0.3	1.90 ±0.07	2.4 ±0.5	1.84 ±0.08	1.31 ±0.01
χ^2	0.005	0.040	0.084	0.324	0.501	0.683	10.099	3.143	0.233
R^2	0.970	0.957	0.968	0.761	0.771	0.803	0.736	0.905	0.992
Langmuir isotherm									
$K_L \times 10^2$ $(dm^3\ mg^{-1})$	10.1 ±0.2	5.47 ±0.01	3.73 ±0.01	9.0 ±0.3	9.75 ±0.09	9.81 ±0.08	30.8 ±0.7	13.2 ±0.3	9.19 ±0.01
q_{max} $(mg\ g^{-1})$	1.42 ±0.02	3.50 ±0.01	6.85 ±0.01	3.4 ±0.2	4.34 ±0.08	5.57 ±0.06	16.1 ±0.8	17.6 ±0.2	29.4 ±0.1
χ^2	0.005	0.008	0.018	0.156	0.224	0.284	2.889	0.613	0.021
R^2	0.973	0.991	0.993	0.885	0.900	0.918	0.925	0.981	0.999
Temkin isotherm									
K_T $(dm^3\ mg^{-1})$	1.30 ±0.05	0.832 ±0.004	0.720 ±0.004	0.754 ±0.008	0.854 ±0.002	0.948 ±0.008	2.68 ±0.09	1.52 ±0.01	0.986 ±0.005
b_t $(J\ g\ mol^{-1}mg^{-1})$	8820 ±60	3830 ±40	2240 ±30	3100 ±80	2490 ±70	2020 ±90	710 ±9	679 ±1	689 ±5
χ^2	0.009	0.035	0.098	0.106	0.187	0.282	3.447	0.135	1.545
R^2	0.947	0.962	0.963	0.922	0.914	0.919	0.910	0.996	0.947
Dubinin-Radushkevich isotherm									
$K_{DR} \times 10^6$ $(mol^2\ J^{-2})$	2.3 ±0.5	3.33 ±0.08	3.79 ±0.07	2.42 ±0.01	2.39 ±0.02	2.46 ±0.02	0.401 ±0.01	0.797 ±0.005	12.2 ±0.4
q_{DR} $(mg\ g^{-1})$	1.0 ±0.4	2.07 ±0.06	3.34 ±0.05	2.42 ±0.01	3.14 ±0.03	4.00 ±0.03	13.0 ±0.1	11.7 ±0.4	14.3 ±0.5
E $(J\ mol^{-1})$	460 ±50	387 ±5	363 ±8	462 ±1	458 ±2	451 ±2	1120 ±10	792 ±5	202 ±5
χ^2	0.041	0.079	0.230	0.004	0.029	0.084	0.153	1.683	1.662
R^2	0.767	0.913	0.912	0.997	0.987	0.976	0.996	0.949	0.943

5.4.2.3. Thermodynamic analysis of MLT and CHP adsorption onto SCG 400 materials

Van't Hoff plots of MLT and CHP adsorption onto materials obtained through thermochemical conversion of SCG at 400°C are given in Figure 23. The results of the thermodynamic analysis are provided in Table 16.

The adsorption of MLT onto all materials shows spontaneity as indicated by negative ΔG^0 values, but this spontaneity decreases with an increase in adsorption temperature, suggesting that higher temperatures make the MLT adsorption less favorable. Both the entropy and enthalpy of the system decrease significantly during the adsorption of MLT, denoting that these processes are exothermic and reduce the randomness of the system. This points to the adsorption of MLT being predominantly entropy-driven, where the organization of the system into a more ordered state is thermodynamically favored at lower temperatures.

The obtained ΔG^0 values also indicate that the adsorption of CHP onto all materials is a spontaneous process, as ΔG^0 values are negative. This spontaneity increases with the rise in adsorption temperature, making the process more favorable under higher temperatures. Additionally, the entropy of the system increases with the adsorption of CHP, suggesting an increase in randomness. However, the enthalpy decreases for all cases except for materials with combined activation, where it increases, indicating that the process is exothermic in most cases and endothermic when combined activation materials are involved.

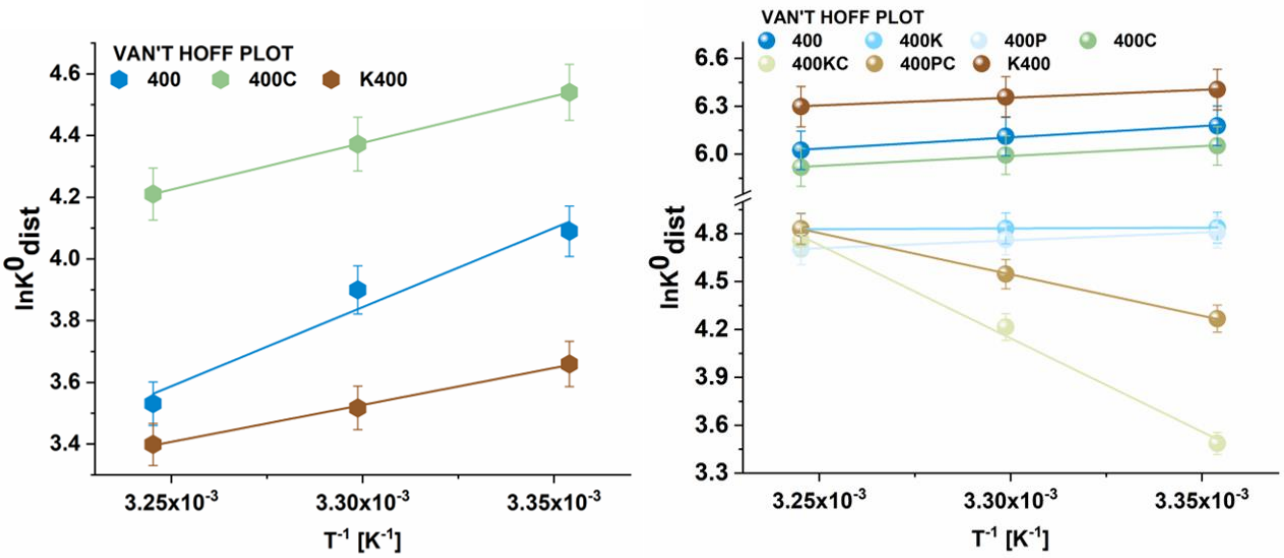

Figure 23. Van't Hoff plots for MLT (left) and CHP (right) adsorption onto SCG materials thermochemically treated at 400°C

Table 16. Thermodynamic parameters of MLT and CHP adsorption onto SCG 400 materials at 25, 30, and 35°C

		ΔH^0 (kJ mol^{-1})	ΔS^0 (J mol^{-1}K^{-1})	ΔG^0 (kJ mol^{-1})			R^2
T (°C) →				25	30	35	
MLT	400	−42 ±2	−108 ±5	−10.5 ±0.5	−9.7 ±0.5	−9.1 ±0.5	0.927
	400C	−25.2 ±0.1	−46.7 ±0.1	−11.4 ±0.1	−11.0 ±0.1	−10.8 ±0.1	0.999
	K400	−19.9 ±0.4	−36.4 ±0.6	−9.1 ±0.4	−8.9 ±0.4	−8.7 ±0.4	0.996
CHP	400	−11.7 ±0.6	12.1 ±0.6	−15.3 ±0.8	−15.4 ±0.8	−15.5 ±0.8	0.984
	400K	−0.82 ±0.04	37 ±2	−11.8 ±0.5	−12.2 ±0.6	−12.4 ±0.6	0.986
	400P	−8.2 ±0.7	12.6 ±0.7	−11.9 ±0.6	−12.0 ±0.6	−12.1 ±0.6	0.982
	400C	−10.3 ±0.5	15.8 ±0.8	−15.0 ±0.8	−15.1 ±0.8	−15.2 ±0.8	0.984
	400KC	97 ±5	360 ±20	−7.6 ±0.4	−10.5 ±0.5	−12.3 ±0.6	0.989
	400PC	43.0 ±0.1	179 ±1	−10.0 ±0.1	−11.5 ±0.1	−12.4 ±0.1	0.999
	K400	−8.1 ±0.4	26 ±1	−15.8 ±0.8	−16.0 ±0.8	−16.1 ±0.8	0.985

5.4.3. Discussion on MLT and CHP adsorption onto SCG 400 materials

The thermochemical conversion at 400°C, along with various activation methods, reveals intricate details about the effects of activation processes on material morphology, surface chemistry, and adsorption efficiency. SEM micrographs show that the materials treated post-carbonization retained a porous, spongy-like structure with unevenly distributed pores, indicating the preservation of the original SCG morphology. In contrast, the KOH-activated material prior to carbonization exhibited a combination of the raw SCG morphology and needle-like structures. This suggests that KOH reacts with SCG during high-temperature treatment, resulting in a unique morphology that enhances adsorption properties.

The elemental analysis reveals significant variations in atomic percentages, indicating the profound impact of activation processes on surface chemistry. All materials displayed high proportions of C, O, and N. Notably, the material activated with KOH prior to carbonization (K400) had a markedly lower C content and a higher O content, suggesting enhanced formation of oxygen functional groups on the surface. This change is consistent with the introduction of K and P in materials activated with KOH and H_3PO_4, respectively. FTIR spectra indicate significant changes in surface chemistry due to thermochemical conversion and chemical activation. Physical activation did not significantly alter the functional groups on the material's surface, as evidenced by the similarity in FTIR spectra between physically activated and non-activated materials. However, chemical activation with KOH and H_3PO_4 introduced noticeable changes. Bands corresponding to C=C stretching in aromatic rings and C-H in-

plane deformations are present in all materials. Additional bands from KOH activation, such as carboxylate anion stretches and C-OH bending vibrations, indicate the introduction of more functional groups, potentially enhancing the material's adsorption capabilities. Zeta potential measurements showed that all materials exhibited a negatively charged surface under experimental conditions. The isoelectric points varied, with the KOH-activated material after the carbonization (400K) having a relatively low isoelectric point, indicating a highly negatively charged surface at pH=6. This characteristic enhances the material's interaction with MLT and CHP. BET measurements revealed small specific surface areas and total pore volumes for all samples, typical of low-temperature carbonization. The K400 sample exhibited the largest S_{BET} and V_{tot} values, suggesting that KOH activation prior to carbonization enhances surface area and pore enlargement. However, no straightforward correlation between specific surface area and pore volume was observed, indicating that pore distribution and size significantly influence surface area.

The adsorption equilibrium for MLT was reached after 90 minutes (Figure 20). The PSO kinetic model provided the best fit, indicating that adsorption is influenced by the concentration of both the material and the pesticide. The similar q_e values across materials suggest consistent adsorption capacity, while varying k_2 values indicate differing adsorption rates, with the fastest adsorption observed in material 400. The Elovich model confirmed a high initial adsorption rate, and the IPD model indicated a three-stage adsorption process, reflecting complex adsorption mechanisms. CHP adsorption equilibrium was achieved after 1440 minutes, with both PFO and PSO models fitting the data well. The good fit of both models indicates a complex, multi-step adsorption process. The highest adsorption capacity for CHP was observed in K400, with the PSO model indicating dependency on material and pesticide concentrations. The Elovich model suggested prolonged adsorption due to simultaneous adsorption and desorption, and the IPD model revealed three distinct adsorption stages, particularly for 400K, 400C, and 400PC materials.

Both Freundlich and Langmuir isotherm models fit the experimental data well, with the Langmuir model generally providing a better fit. This suggests adsorption occurs on well-defined, homogeneous sites. The highest CHP adsorption capacity was observed for K400 at 25°C, supporting the assumption of the positive effect of KOH activation prior to carbonization. For MLT, the highest adsorption capacity was observed for K400 at 25°C. The Temkin model indicated strong binding for CHP on K400, while the Dubinin-Radushkevich model suggested physisorption for both pesticides, confirmed by low mean free energy values. The thermodynamic analysis revealed spontaneous adsorption processes for both MLT and CHP, with negative ΔG^0 values. The spontaneity of MLT adsorption decreased with increasing temperature, indicating less favorable adsorption at higher temperatures. In contrast, CHP adsorption became more favorable at higher temperatures, with increasing system randomness (entropy) and generally exothermic processes.

The findings indicate that KOH activation prior to carbonization significantly enhances the adsorption properties of SCG 400 materials, particularly for CHP. The introduction of additional functional groups, increased surface area, and unique morphological features contribute to improved adsorption capacities. The adsorption processes for both MLT and CHP are complex, involving multiple stages and predominantly physisorption mechanisms.

5.5. Materials obtained by thermochemical conversion of SCG at 650°C – SCG 650 materials

5.5.1. Characterization of SCG 650 materials

The SEM micrographs displayed in Figure 24 show the morphology of the SCG materials thermochemically treated at 650°C, which remained unchanged during the carbonization and activation processes, maintaining porous and spongy-like structure with unevenly distributed pores, consistent with the original morphology of raw SCG and materials thermochemically treated at 400°C.

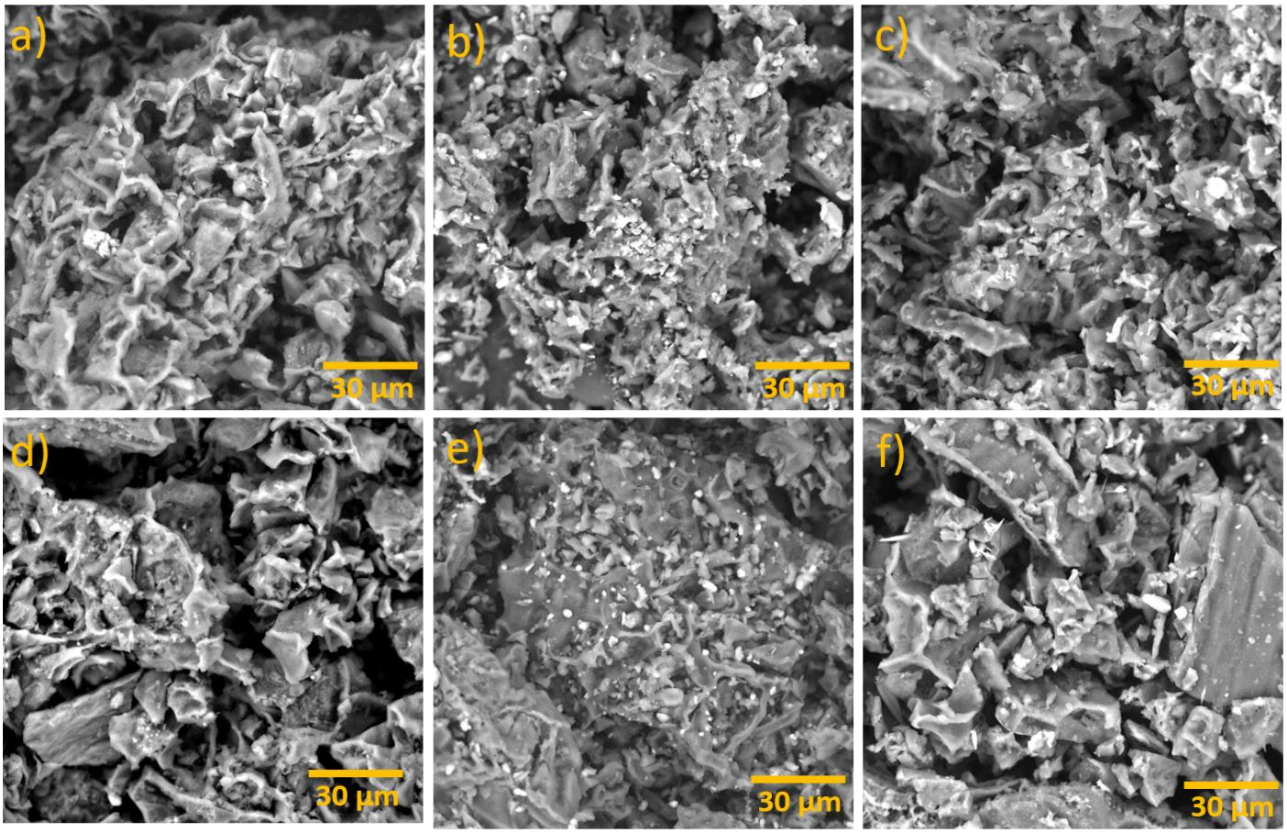

Figure 24. SEM micrographs of: a) 650; b) 650K; c) 650P; d) 650C; e) 650KC; f) 650PC (magnification 2000×)

As in the case of SCG materials thermochemically treated at 400°C, the elemental composition exhibited distinct atomic percentages of various elements in these carbon materials. C, O, and N are present in significant proportions, indicating the organic nature of the precursor, with carbon being the predominant component in all materials (Table 17). With the increase of the carbonization temperature, the rise in the at.% of C can be seen, as expected. Notably, the atomic percentage of oxygen increases with the activation process, particularly in materials activated with KOH, indicating a primary influence on surface oxygen functional groups.

Chemical activation with KOH and H_3PO_4 resulted in the increased at.% of K and P, respectively, while physical activation did not affect the elemental composition of the materials. Minor elements such

as magnesium, calcium, sodium, chlorine, and sulfur contribute to the elemental profile in varying but relatively small amounts.

Table 17. Elemental composition of the SCG materials thermochemically treated at 650°C

(at%)→	C	O	N	K	P	Mg	Ca	Na	Cl	S	Si
650	82.13	8.70	8.11	0.55	0.08	0.22	0.21	0.00	0.00		
650K	73.50	17.72	5.76	2.57	0.07	0.17	0.18	0.03	0.00		
650P	79.01	12.23	6.27	0.70	1.23	0.23	0.29	0.04	0.00		
650C	80.25	9.34	8.94	0.77	0.12	0.21	0.32	0.04	0.00		
650KC	71.54	16.80	7.70	3.35	0.10	0.21	0.18	0.06	0.01	0.03	0.01
650PC	77.44	13.79	6.27	0.55	1.40	0.21	0.21	0.02	0.01	0.05	0.05

The FTIR spectra of these materials, as shown in Figure 25, indicate that by the temperature of 650°C, the SCG remain almost without functional groups. Additionally, the activation processes with CO_2 and H_3PO_4 do not introduce new functional groups. In contrast, activation with KOH induces several changes in the FTIR spectrum. The band at 1616 cm^{-1} is attributed to the stretching of C=C bonds in aromatic rings, while the bands at 1391 cm^{-1} and 1364 cm^{-1} are assigned to C-H in-plane deformation vibrations [90]. The bands at 967 cm^{-1} and 1000 cm^{-1} correspond to C-O bending vibrations, and the C-H bending vibrations in the aromatic ring are observed at 823 cm^{-1} and 694 cm^{-1} [94]. These changes indicate that KOH activation significantly alters the surface chemistry of the SCG material by introducing new functional groups.

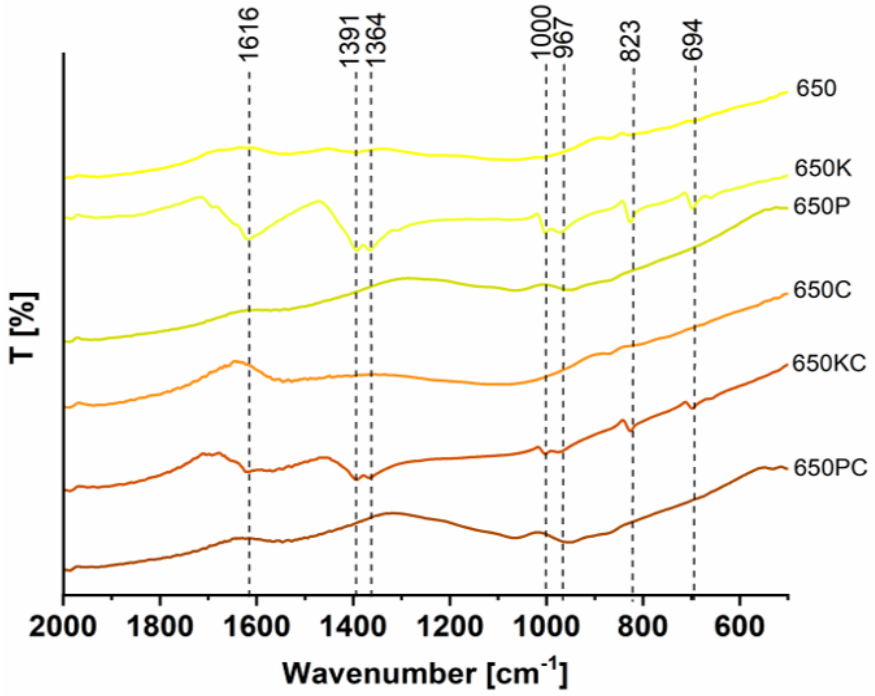

Figure 25. FTIR spectra of the SCG materials thermochemically treated at 650°C

Zeta potential measurements were conducted to assess the charge of the materials and determine their isoelectric points. The isoelectric points for 650, 650K, 650P, 650C, 650KC, and 650PC were found to be 4.35, 6.16, 5.47, 5.23, 2.29, and 3.71, respectively (Figure 26). Given that the initial pH value of

all materials suspended in 50% ethanol was 6, it can be concluded that all materials, except 650K, exhibit a negatively charged surface under the conditions employed for adsorption measurements.

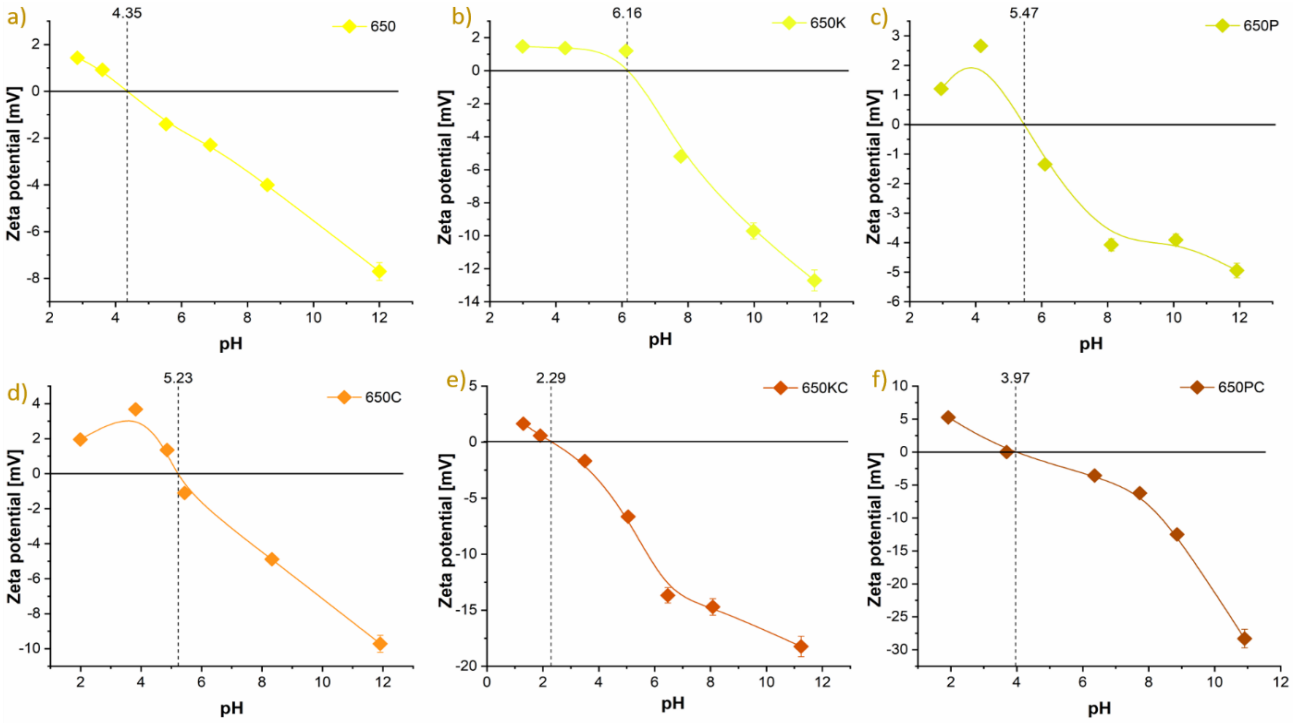

Figure 26. Dependence of zeta potential of pH value of the suspension with indicated IEP for materials: a) 650; b) 650K; c) 650P; d) 650C; e) 650KC; f) 650PC

The results of BET measurements and total pore volume determination, as summarized in Table 18, reveal that all the samples have relatively small specific surface areas (S_{BET}) and total pore volumes (V_{tot}). After the chemical activation of material 650, the specific surface area and total pore volume highly increase, while in the case of physical activation, S_{BET} increases, but V_{tot} decreases, indicating the formation of a larger number of smaller pores on the surface of the material. Physicochemical activation KOH/CO_2 showed multiple times higher values of these parameters, while H_3PO_4/CO_2 showed lower results, implying that results obtained by combining these activation methods can not be linked to the results obtained or the materials with separate activations.

Table 18. Specific surface areas by BET method (S_{BET}) and total pore volumes (V_{tot}) of the SCG materials thermochemically treated at 650°C

Sample	S_{BET} [$m^2\ g^{-1}$]	$V_{tot} \times 10^3$ [$cm^3\ g^{-1}$]
650	0.826	1.39
650K	2.207	4.06
650P	5.472	4.94
650C	1.349	0.99
650KC	98.03	44.37
650PC	0.706	0.77

5.5.2. Adsorption of CHP onto SCG 650 materials

5.5.2.1. Kinetic studies for CHP adsorption onto SCG 650 materials

The graphical representations of kinetic models indicated that the equilibrium between CHP and the materials is achieved after 400 minutes, except for 650KC, where the equilibrium is reached after 1440 minutes (Figure 27). For consistency, all further experiments will be performed at 1440 minutes incubation time. The obtained parameters (Table 19) showed the difference in the kinetic behavior of the materials due to the different activation processes applied. The experimental data for the adsorption onto 650 and 650P did not fit well R^2 in PFO and PSO kinetic models according to R^2, but it is slightly better for PFO. Experimental data for the other materials fitted well into both PFO and PSO. According to q_e values that are similar for both PFO and PSO, it can be seen that the 650KC has the highest equilibrium adsorption capacity under the given experimental conditions (7.33±0.03 mg g^{-1}). The adsorption process is considered slow as the equilibrium is reached after 24 h. The parameters of the Elovich kinetic model confirmed the previously stated, as the initial rate is lower than the desorption constant of the adsorption. The IPD kinetic model plot displays two linear stages for CHP adsorption onto all materials, except for adsorption onto materials with combined activation, where the adsorption process has three stages. The decline in k_{id} values across stages corresponds to the gradual slowing down of the adsorption process as the boundary layer value increases through the stages, signifying an increase in the molecules adsorbed on the material's surface. Ultimately, the boundary layer reaches a value similar to q_e values obtained from PFO and PSO, and k_{id} reach very low values, signifying the completion of the adsorption process.

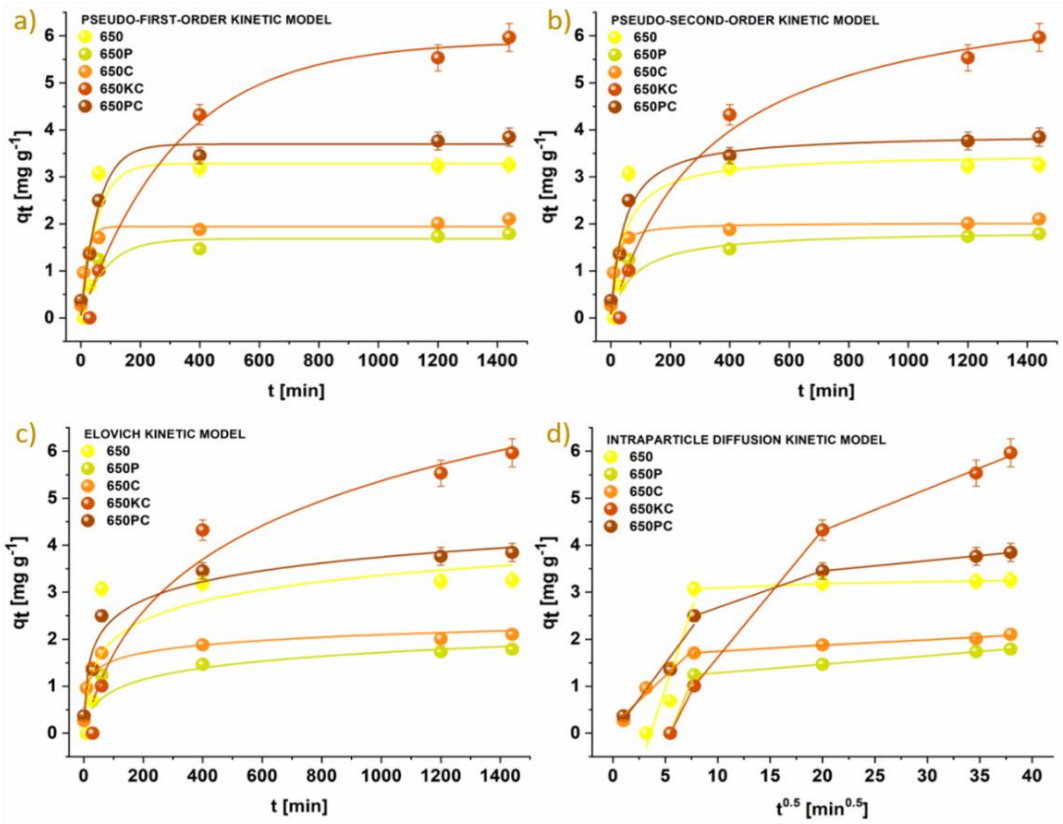

Figure 27. Graphical representations of kinetic models for CHP adsorption onto SCG materials thermochemically treated at 650°C: a) PFO; b) PSO; c) Elovich; d) IPD

Table 19. Kinetic parameters of CHP (5×10^{-5} mol dm^{-3}) adsorption onto investigated materials (1 mg mL^{-1})

Material →	650	650P	650C	650KC	650PC
Pseudo-first order					
qe ($mg\ g^{-1}$)	3.3 ±0.3	1.7 ±0.7	1.94 ±0.05	5.89 ±0.02	3.70 ±0.02
k_1 (min^{-1}) $\times10^2$	1.9 ±0.4	1.2 ±0.5	5.12 ±0.06	0.324 ±0.002	1.73 ±0.02
χ^2	0.394	0.153	0.028	0.120	0.053
R^2	0.821	0.713	0.937	0.984	0.974
Pseudo-second order					
qe ($mg\ g^{-1}$)	3.5 ±0.5	1.9 ±0.8	2.02 ±0.03	7.33 ±0.03	3.92 ±0.02
k_2 ($mg\ min^{-1}\ g^{-1}$) $\times10^2$	0.61 ±0.07	0.72 ±0.08	4.31 ±0.02	0.0112 ±0.0002	0.624 ±0.003
χ^2	0.524	0.155	0.007	0.175	0.050
R^2	0.763	0.709	0.984	0.976	0.975
Elovich model					
α ($mg\ g^{-1}\ min^{-1}$)	0.15 ±0.09	0.040 ±0.008	1.51 ±0.08	0.0262 ±0.0004	0.402 ±0.004
β ($g\ mg^{-1}$)	1.7 ±0.7	2.7 ±0.8	4.15 ±0.08	0.487 ±0.004	1.75 ±0.05
χ^2	0.793	0.183	0.033	0.298	0.092
R^2	0.640	0.657	0.924	0.959	0.955
Intraparticle diffusion model					
I part					
C ($mg\ g^{-1}$)	−2.39	−3.00	0.170	−2.430	−0.023
k_{id} ($mg\ g^{-1}\ min^{-0.5}$)	0.669	0.549	0.210	0.444	0.302
R^2	0.810	--	0.946	0.988	0.896
II part				--	
C ($mg\ g^{-1}$)	3.041	1.104	1.619	−1.090	1.892
k_{id} ($mg\ g^{-1}\ min^{-0.5}$)	0.006	0.018	0.012	0.271	0.078
R^2	0.923	1.000	0.970	--	--
III part					
C ($mg\ g^{-1}$)				2.532	3.019
k_{id} ($mg\ g^{-1}\ min^{-0.5}$)				0.089	0.022
R^2				0.986	0.999

5.5.2.2. Isotherm studies for CHP adsorption onto SCG 650 materials

The graphical representations of the experimental data for CHP adsorption onto SCG materials thermochemically treated at 650°C, along with the corresponding isotherm model fits, are shown in Figure 28, and the calculated parameters, including R^2 and χ^2, are provided in Table 20.

The parameters in Table 20 show that both Freundlich and Langmuir isotherm models effectively describe the CHP adsorption process onto all materials at all investigated temperatures. This suggests that the surface of the materials is not entirely homogeneous energetically, which is expected given the precursor and activation processes used. At all adsorption temperatures, the n parameter from the Freundlich isotherm model is greater than 1 for all materials, indicating the favorability of the adsorption processes. However, the n value decreases with increasing adsorption temperature in all cases except for the adsorption of CHP onto 650, where it increases.

The maximum amount of CHP that could be adsorbed by 1 g of material, as determined from the Langmuir isotherm model, ranges from 2.52 to 7.14 mg at 25°C, from 3.78 to 12.3 mg at 30°C, and from 3.94 to 51.7 mg at 35°C. 650KC demonstrated the best adsorption properties for CHP removal at 25°C, while at higher temperatures, 650C exhibited the best efficiency. With increasing adsorption temperature, q_{max} values increase for CHP adsorption onto 650P, 650C, and 650PC, while they decrease in other cases.

The b_T parameter from the Temkin isotherm model, representing adsorption heat, increases with adsorption temperature, except for CHP adsorption onto 650KC. This suggests that the adsorption processes are endothermic in all cases except for 650KC. This is in line with that that the 650KC material does not adsorb CHP at 35°C under the given experimental conditions, which highlights the significance of adsorption temperature. The K_T parameter from the Temkin isotherm model, representing the binding constant, decreases with increasing adsorption temperature for CHP adsorption onto 650P, 650C, and 650KC. This indicates that the binding strength of CHP molecules to the materials weakens with rising temperature. This finding is further supported by the E parameter from the Dubinin-Radushkevich isotherm, which also decreases in the mentioned cases. Since the E values are significantly below 8 kJ mol^{-1}, it can be concluded that the process is primarily physisorption across all investigated materials and temperatures.

In the case of CHP adsorption onto materials obtained through the thermochemical conversion of SCG at 650°C, isotherm studies indicated that only the physical activation increases the adsorption efficiency of the material, while chemical activations lead to its decrease.

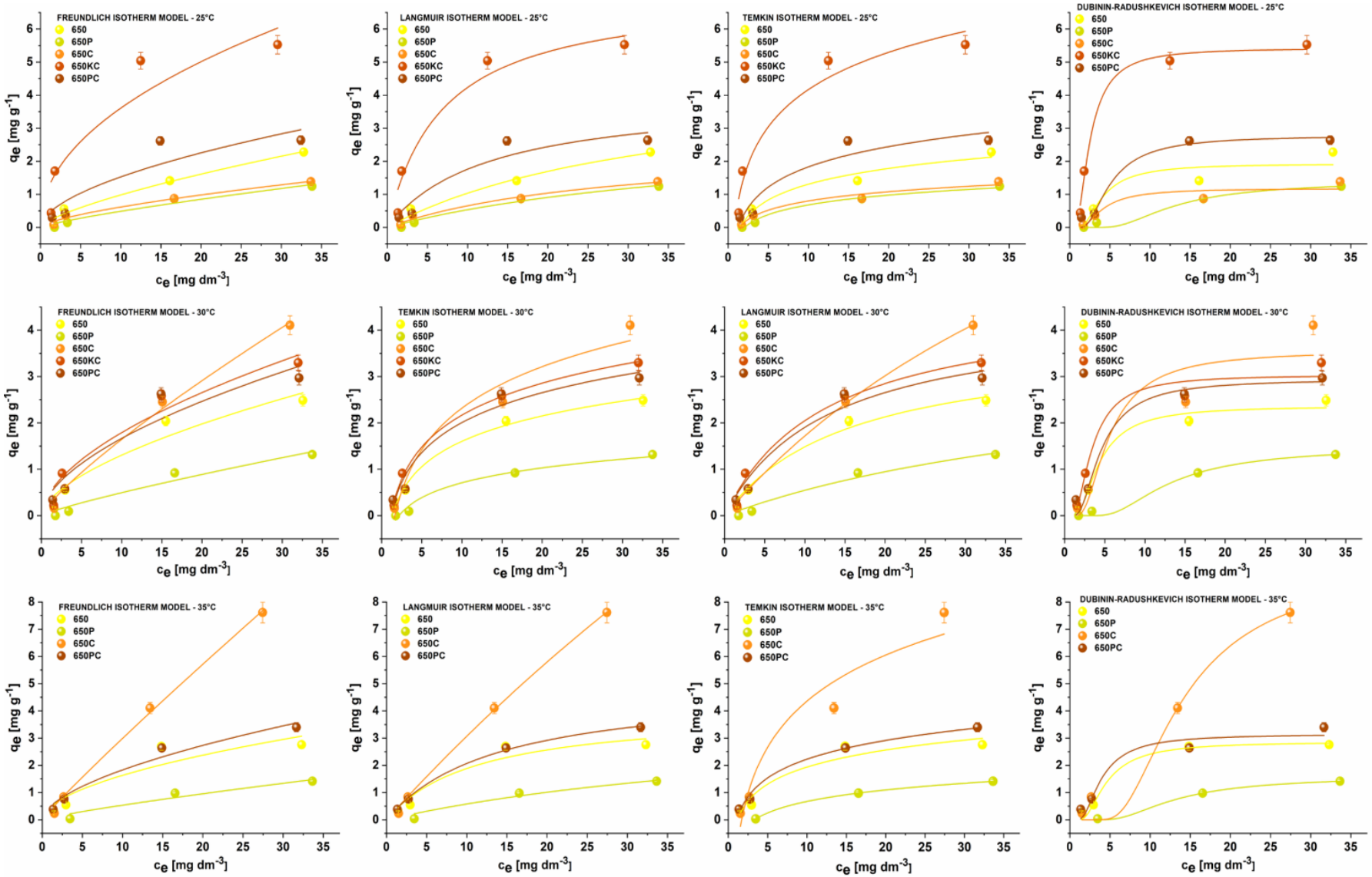

Figure 28. Graphical representations of experimental data for CHP adsorption onto SCG 650 material fittings isotherm models at 25°C (top row), 30°C (middle row), and 35°C (bottom row)

Table 20. Isotherm adsorption parameters of CHP adsorption onto SCG 650 materials (1 mg mL^{-1}) at 25°C, 30°C, and 35°C

Material →	650			650P			650C			650KC			650PC		
	25	30	35	25	30	35	25	30	35	25	30	35	25	30	35
Freundlich isotherm															
K_F ($(mg\ g^{-1})(dm^3\ g^{-1})^{1/n}$)	1.89 ±0.03	3.28 ±0.08	4.7 ±0.8	0.76 ±0.01	0.71 ±0.01	0.78 ±0.07	1.32 ±0.03	2.47 ±0.02	3.48 ±0.01	12 ±2	3.42 ±0.05	/	4.2 ±0.8	4.5 ±0.3	4.85 ±0.05
n	1.40 ±0.04	1.67 ±0.06	1.8 ±0.3	1.24 ±0.06	1.18 ±0.05	1.2 ±0.2	1.49 ±0.02	1.21 ±0.01	1.07 ±0.01	2.1 ±0.2	1.33 ±0.06	/	1.8 ±0.5	1.8 ±0.2	1.73 ±0.04
χ^2	0.035	0.104	0.358	0.019	0.027	0.065	0.008	0.033	0.055	1.109	0.109	/	0.391	0.232	0.095
R^2	0.963	0.917	0.798	0.945	0.934	0.869	0.975	0.990	0.995	0.822	0.926	/	0.772	0.875	0.955
Langmuir isotherm															
$K_L \times 10^2$ ($dm^3\ mg^{-1}$)	2.81 ±0.05	6.52 ±0.02	8.8 ±0.1	2.22 ±0.03	1.82 ±0.03	1.7 ±0.1	3.53 ±0.03	1.61 ±0.01	0.62 ±0.01	14.6 ±0.6	6.13 ±0.05	/	7.9 ±0.5	7.74 ±0.04	7.21 ±0.01
q_{max} ($mg\ g^{-1}$)	4.67 ±0.04	3.78 ±0.03	4.03 ±0.09	2.98 ±0.03	3.53 ±0.04	3.94 ±0.09	2.52 ±0.02	12.3 ±0.1	51.7 ±0.1	7.14 ±0.07	5.42 ±0.05	/	4.0 ±0.2	4.38 ±0.03	4.96 ±0.01
χ^2	0.034	0.028	0.162	0.010	0.018	0.047	0.009	0.012	0.035	0.406	0.088	/	0.204	0.082	0.007
R^2	0.965	0.977	0.908	0.970	0.957	0.905	0.972	0.996	0.997	0.935	0.940	/	0.881	0.956	0.997
Temkin isotherm															
K_t ($dm^3\ mg^{-1}$)	0.667 ±0.005	0.760 ±0.001	0.857 ±0.008	0.494 ±0.002	0.463 ±0.003	0.304 ±0.001	0.725 ±0.005	0.602 ±0.005	0.597 ±0.006	1.30± 0.04	0.871 ±0.001	/	0.79± 0.04	0.862 ±0.004	0.940 ±0.002
b_t ($kJ\ g\ mol^{-1}mg^{-1}$)	3600 ±40	3190 ±10	2840 ±0.07	5810 ±30	5440 ±30	4220 ±10	6140 ±40	1950 ±50	1050 ±60	1520 ±60	2490 ±10	/	2800 ±100	2710 ±50	2580 ±30
χ^2	0.042	0.010	0.161	0.006	0.013	0.000	0.014	0.167	0.945	0.357	0.013	/	0.204	0.092	0.026
R^2	0.956	0.992	0.909	0.984	0.969	1.000	0.959	0.950	0.918	0.943	0.991	/	0.881	0.951	0.988
Dubinin-Radushkevich isotherm															
$K_{DR} \times 10^6$ ($mol^2\ J^{-2}$)	2.5 ±0.3	4.2 ±0.2	2.87 ±0.03	23.2 ±0.4	1.58 ±0.01	21.7 ±0.1	2.6 ±0.3	2.93 ±0.02	24.2 ±0.3	1.06 ±0.03	2.2 ±0.2	/	3.75 ±0.05	0.11 ±0.02	2.21 ±0.06
q_{DR} ($mg\ g^{-1}$)	1.9 ±0.2	2.4 ±0.2	2.86 ±0.03	1.40 ±0.03	1.48 ±0.01	1.60 ±0.01	1.2 ±0.2	3.55 ±0.03	9.34 ±0.02	5.42 ±0.03	2.7 ±0.2	/	2.78 ±0.03	2.9 ±0.2	3.14 ±0.06
E ($J\ mol^{-1}$)	450 ±30	340 ±30	418 ±6	148 ±8	562 ±1	152 ±2	440 ±30	413 ±4	144 ±3	686 ±5	480 ±20	/	365 ±7	2200 ±100	476 ±8
χ^2	0.156	0.516	0.048	0.011	0.000	0.001	0.055	0.061	0.380	0.070	1.842	/	0.051	7.930	0.155
R^2	0.835	0.844	0.973	0.969	1.000	0.998	0.832	0.967	0.967	0.989	0.869		0.970	0.866	0.927

5.5.2.3. Thermodynamic analysis of CHP adsorption onto SCG 650 materials

Thermodynamics of the adsorption processes have also been investigated, and Figure 29 shows Van't Hoff plots for CHP adsorption onto these materials. The obtained thermodynamic parameters with corresponding R^2 values are given in Table 21. It can be concluded that the adsorption of CHP is, in all cases, spontaneous, as the values $\Delta G^0 < 0$. The CHP adsorption processes are endothermic with increasing randomness of the system, except for the adsorption onto 650KC, as assumed previously. The processes of CHP adsorption onto 650C and 650KC are highly dependent on the adsorption temperature. With the temperature increase, the efficiency of 650C increases, while in the case of 650KC, it decreases. It can be seen that the adsorption of CHP onto 650C is entropy-driven, while the process is enthalpy-driven for 650KC. Even though thermodynamic analysis predicts spontaneous adsorption of CHP onto 650KC at 35°C, that is not the case experimentally, and for that reason, these results must be taken with caution.

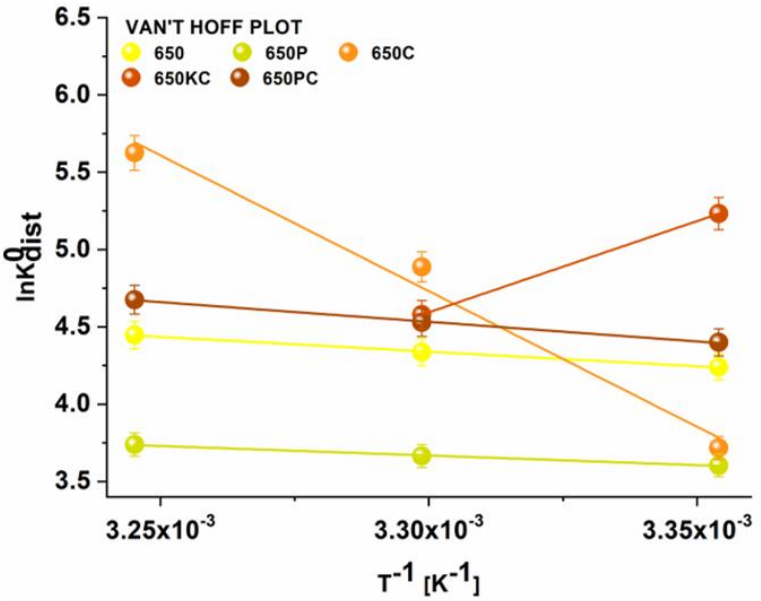

Figure 29. Van't Hoff plots for CHP adsorption onto SCG materials thermochemically treated at 650°C

Table 21. Thermodynamic parameters of CHP adsorption onto materials at 25, 30, and 35°C

	ΔH^0 (kJ mol^{-1})	ΔS^0 (J mol^{-1}K^{-1})	ΔG^0 (kJ mol^{-1})			R^2
T (°C) →			25	30	35	
650	15.8 ±0.1	88.2 ±0.1	−10.5 ±0.1	−10.9 ±0.1	−11.4 ±0.1	0.994
650P	10.3 ±0.1	64.5 ±0.1	−8.92 ±0.01	−9.23 ±0.01	−9.62 ±0.01	0.992
650C	146 ±4	521 ±5	−9.42 ±0.04	−12.0 ±0.2	−14.6 ±0.3	0.971
650KC	−98.2	−285.7	−13.0	−11.5	−10.1	--
650PC	21.1 ±0.1	107 ±2	−10.9 ±0.1	−11.4 ±0.1	−12.0 ±0.1	0.995

5.5.3. Discussion on MLT and CHP adsorption onto SCG 650 materials

SEM micrographs of SCG materials thermochemically treated at 650°C reveal a porous, spongy-like structure with unevenly distributed pores. This morphology remains consistent with that of raw SCG and materials treated at 400°C, indicating that the high temperature does not significantly alter the material's fundamental structure. EDX analysis shows that C is the predominant component, with significant amounts of O and N, which reflects the organic nature of the precursor. The increase in the atomic percentage of O post-activation, especially with KOH, suggests an enhancement in surface oxygen functional groups, which can play a crucial role in adsorption processes. Minor elements are present in varying small amounts, adding to the complexity of the material's composition. FTIR spectra indicate that at 650°C, the SCG materials lose most of their functional groups. However, activation with KOH introduces new functional groups, such as aromatic C=C bonds and various C-H and C-O vibrations, significantly altering the surface chemistry. This modification is crucial as it enhances the material's interaction with adsorbates through specific functional groups. BET measurements reveal very low specific surface area and total pore volume of the materials, but chemical activation, particularly with KOH, drastically increases them. Physical activation also increases the specific surface area but reduces the total pore volume, indicating the formation of smaller pores. Combined activation methods yield even higher values for these parameters, suggesting a synergistic effect.

The screening test (Section 5.1.) revealed that SCG 650 materials have a lower affinity for MLT adsorption than raw material. Therefore, they were not analyzed, and the material 650K was not used for CHP adsorption for the same reason. The reasons behind decreased adsorption properties towards MLT are probably due to very low S_{BET} and $V_{tot,}$ indicating clogging of the pores of the materials after the thermochemical treatment at 650°C. Besides this, material 650K exhibits a positive surface charge, indicating weak repulsion between CHP and this material.

The adsorption kinetics of CHP onto SCG materials thermochemically treated at 650°C show variations depending on the activation process. Equilibrium is generally achieved after 400 minutes, except for 650KC, which requires 1440 minutes. This prolonged equilibrium time for 650KC indicates a slower adsorption process. The data for most materials fit well with both PFO and PSO kinetic models, suggesting that the adsorption involves both physisorption and chemisorption mechanisms. The Elovich model indicates that the initial adsorption rate is lower than the desorption constant, particularly for 650KC, highlighting the slow nature of the process. The IPD model reveals two linear stages for CHP adsorption onto most materials, while combined activation processes show three stages, indicating a more complex adsorption mechanism involving multiple diffusion steps.

Both Freundlich and Langmuir isotherm models effectively describe the CHP adsorption process across all materials and temperatures. This dual fit suggests a heterogeneous surface with both monolayer and multilayer adsorption. The Freundlich parameter n values greater than 1 indicate favorable adsorption, although n decreases with increasing temperature, except for adsorption onto 650, where it increases, suggesting temperature dependence. The Langmuir model shows that the maximum adsorption capacity increases with temperature for most materials, indicating endothermic adsorption. Notably, 650KC demonstrates the best adsorption properties at 25°C but loses efficiency at higher temperatures, underscoring the importance of temperature in adsorption efficiency. Thermodynamic analysis using Van't Hoff plots confirms that the adsorption of CHP onto SCG 650 materials is spontaneous ($\Delta G^0 < 0$) and generally endothermic, except for 650KC. The positive entropy change (ΔS^0) suggests increased randomness during adsorption, except for 650KC, where the process is enthalpy-driven. The efficiency of CHP adsorption onto 650C increases with temperature, while it decreases for 650KC, highlighting the critical role of temperature in determining adsorption efficacy.

5.6. Materials obtained by thermochemical conversion of SCG at 900°C – SCG 900 materials

5.6.1. Characterization of SCG 900 materials

The morphology of the SCG materials thermochemically treated at 900°C can be seen on the SEM micrographs in Figure 30. As in the previous cases, the thermochemical treatment did not affect the change in the material morphology. It remained porous and spongy-like, with heterogeneously distributed pores across all activation processes. All materials retained the original morphology of raw SCG.

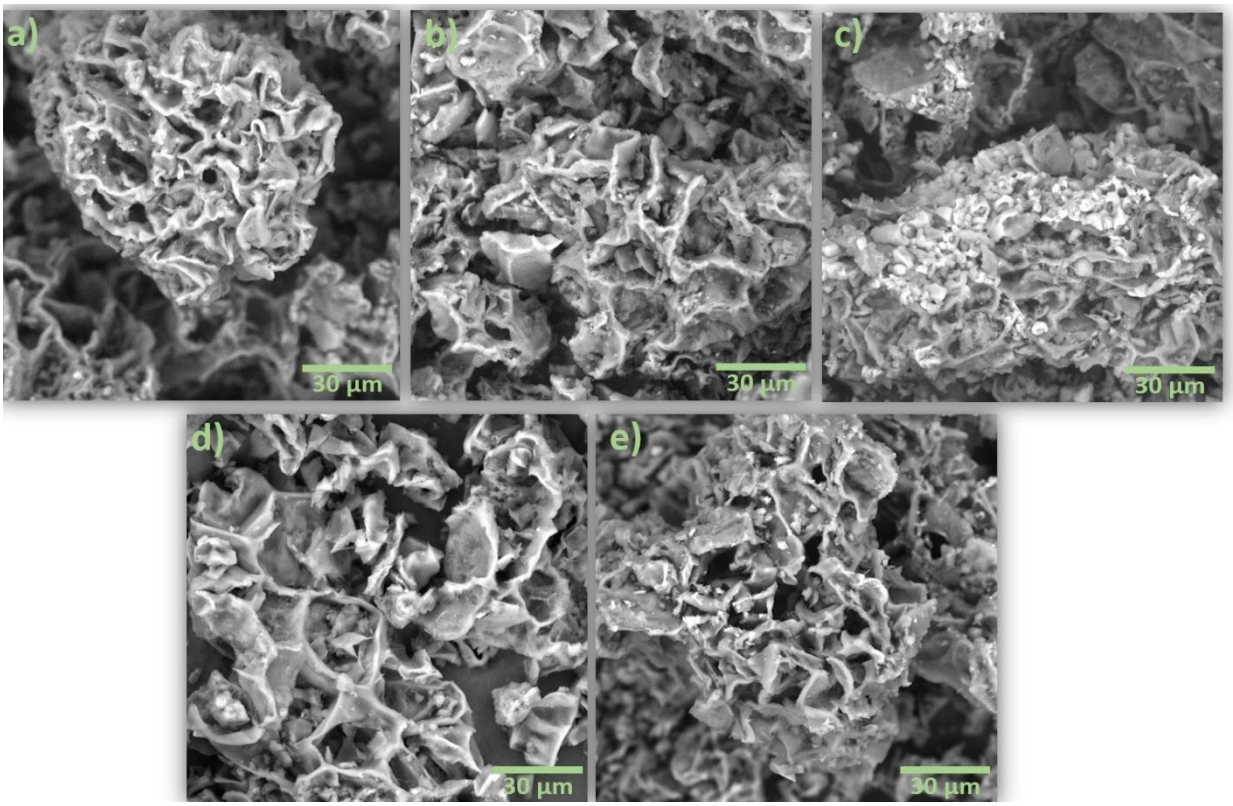

Figure 30. SEM micrographs of: a) 900; b) 900K; c) 900P; d) 900C; e) 900KC (magnification 2000×)

The elemental composition of these materials is given in Table 22. The presence of C, O, and N in a high percentage across all materials reflects the precursor's organic nature. Carbon dominates the elemental content, constituting the primary component across all materials (>75 at.%). It can be noticed that the at.% of O increases with the activation process, especially for the materials activated with KOH, meaning that the activation process primally affects surface oxygen functional groups. Physical activation of the material decreased the presence of trace elements (K, P, Mg, Na, Cl), increasing the atomic percentage of C. As expected, K and P can be noticed in the materials activated with KOH and H_3PO_4, respectively. Minor elements such as Mg, Ca, Na, Cl, and S contribute to the elemental profile, each in varying but relatively small quantities. These results indicated that various activation processes could be used to tailor the material's composition to the needed application.

The elemental composition of these materials is similar to the elemental composition of the SCG materials thermochemically treated at 650°C, indicating that the carbonization temperature above 650°C does not further influence the elemental composition of SCG.

Table 22. Elemental composition of the SCG materials thermochemically treated at 900°C

(at%)→	C	O	N	K	P	Mg	Ca	Na	Cl	S	Si
900	79.28	9.62	9.45	0.94	0.11	0.35	0.22	0.02	0.01		
900K	75.96	15.84	6.15	1.45	0.10	0.20	0.18	0.11	0.01		
900P	78.03	12.83	5.97	0.92	1.67	0.23	0.28	0.06	0.00		
900C	83.69	9.86	5.00	0.55	0.20	0.26		0.02	0.00		
900KC	70.64	18.03	7.64	3.12	0.10	0.23	0.20	0.04	0.00	0.02	0.00

The FTIR spectra of SCG materials thermochemically treated at 900°C are shown in Figure 31. As previously stated, SCG remains almost without functional groups on its surface after thermochemical treatment at 650°C, so the obtained FTIR spectra of the materials thermochemically treated at 650°C and those thermochemically treated at 900°C are quite similar, supporting the similarity in the elemental composition. The bands present in the spectrum are assigned to a specific vibration. The activation with KOH leads to several changes in the FTIR spectrum, increasing with subsequent CO_2 activation. The band at 1615 cm^{-1} is attributed to the stretching of the C=C in the aromatic rings, and the band at 1681 cm^{-1} to the oxygen-containing functional groups (C=O and C-O). The band at 982 cm^{-1} signifies the C-OH bending vibration, and the C-H bending vibrations in the aromatic ring can be seen at 814 and 686 cm^{-1} [90, 94].

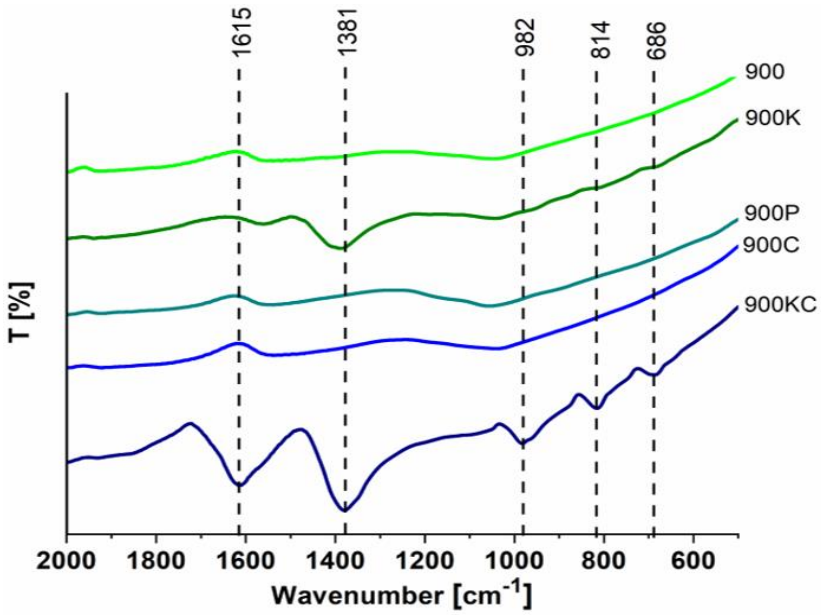

Figure 31. FTIR spectra of the SCG materials thermochemically treated at 900°C

The zeta potential was measured to investigate the charge of the material and its isoelectric point, and its dependence on pH values is given in Figure 32. It can be seen that the isoelectric points of 900, 900K, 900P, 900C, and 900KC are 5.58, 3.39, 4.09, 5.10, and 3.93, respectively. As the initial pH value of all materials suspended in 50 % ethanol was 6, they have a slightly negatively charged surface under the conditions applied for adsorption measurements.

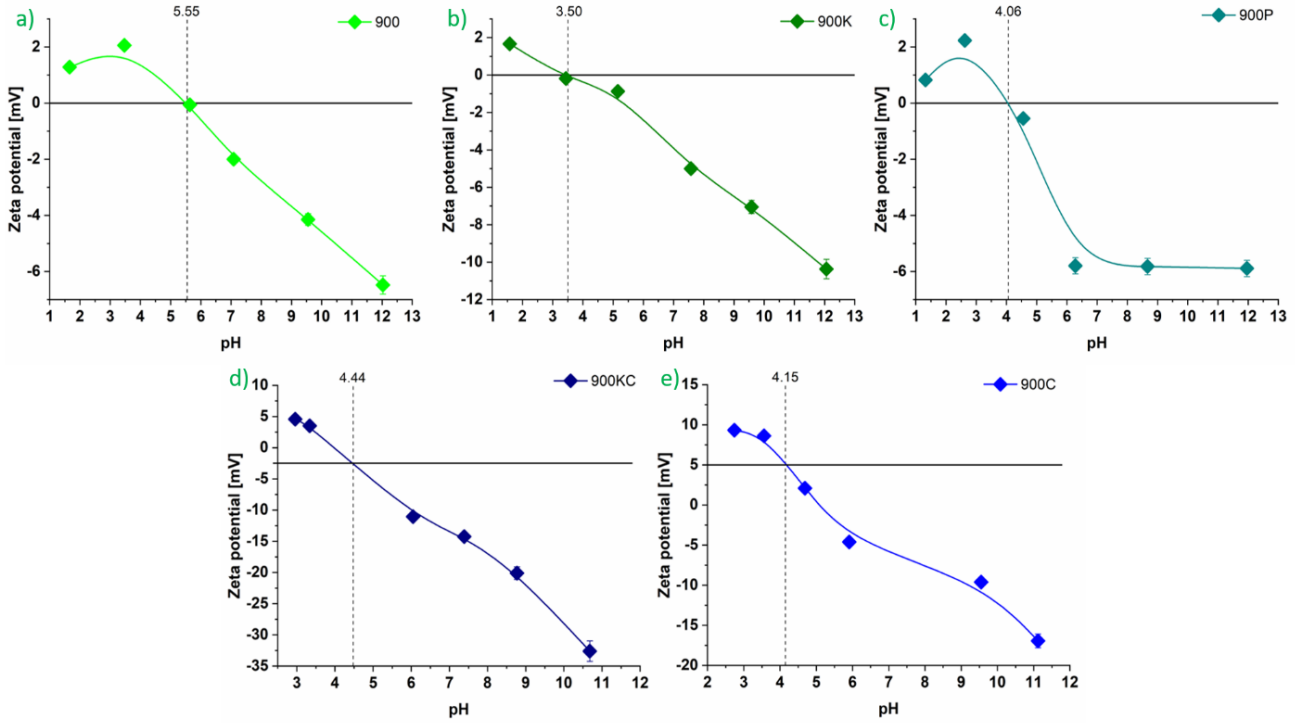

Figure 32. Dependence of zeta potential of pH value of the suspension with indicated IEP for materials: a) 900; b) 900K; c) 900P; d) 900C; e) 900KC

The results obtained from BET and total pore volume measurements (Table 23) revealed that by increasing the temperature of thermochemical treatment S_{BET} and V_{tot} increase. By examining the results, it can be seen that physical activation further increased the specific surface area and total pore volume, highly increasing the porosity of the material. The chemical activation using H_3PO_4 almost did not affect these characteristics, while the activation with KOH influenced their reduction.

Table 23. Specific surface areas by BET method (S_{BET}) and total pore volumes (V_{tot}) of the SCG materials thermochemically treated at 900°C

Sample	S_{BET} [$m^2\ g^{-1}$]	V_{tot} $\times 10^1$ [$cm^3\ g^{-1}$]
900	249.44	1.12
900K	159.98	0.83
900P	248.84	1.07
900C	665.93	2.97
900KC	141.43	0.74

5.6.2. Adsorption of MLT and CHP onto SCG 900 materials

5.6.2.1. Kinetic studies of MLT and CHP adsorption onto SCG 900 materials

The graphical representations of kinetic models (Figure 33) show that equilibrium for adsorption was achieved within the initial 60 minutes for both MLT and CHP, indicating rapid adsorption of these pesticides onto these materials. Upon examining the results in Tables 24 (MLT) and 25 (CHP), it is evident that experimental data for both OP adsorption align well with PFO and PSO kinetic models, as indicated by the high R^2 and low χ^2 values. The q_e values obtained from both kinetic models are similar, confirming both fits' robustness. It can be noticed that the adsorption of MLT is faster compared to the CHP adsorption according to the k_1 and k_2 values. Even though the adsorption of MLT is faster on all investigated materials compared to CHP adsorption, the q_e values are higher for CHP adsorption in all cases.

Parameters of PFO and PSO kinetic models indicate a high influence of the activation process on the adsorption, as they vary greatly depending on the activation process. By comparing q_e and k values of activated materials with non-activated, 900, it can be concluded that activation with KOH, CO_2, and their combination improved the adsorption efficiency of the material up to 5 times, while the activation using H_3PO_4 diminishes it. The maximum equilibrium amount of MLT is obtained with 900KC (q_e=8.43±0.04 mg g^{-1}) and the maximum adsorption rate is obtained for 900K ((86.2 ±0.4) $\times 10^{-2}$ mg min^{-1} g^{-1}), while the highest equilibrium amount of CHP and the maximum adsorption rate are observed with 900KC, with q_e = 19.1 ± 0.4 mg g^{-1} and k = (0.243 ± 0.003) × 10^{-2} mg min^{-1} g^{-1}.

For non-activated, KOH, and CO_2-activated materials, the Elovich model further reveals that the initial adsorption rate (parameter α) is significantly higher than the desorption rate (parameter β), emphasizing faster adsorption kinetics for OPs on these materials and confirming the assumptions of PFO and PSO.

The IPD kinetic model for MLT displays three distinct linear stages (external diffusion, intraparticle diffusion, and equilibrium stage) when adsorbing onto KOH-activated materials, again confirming fast initial adsorption of MLT onto these materials. In other cases, the plot displays two stages. The adsorption of CHP is driven by two distinct linear stages across all cases. IPD kinetic model illustrates a gradual slowdown in the adsorption process as evidenced by declining k_{id} values, which ultimately converge with the boundary layer value reaching levels similar to the q_e values obtained from PFO and PSO models, indicating the completion of the adsorption process, with Ops molecules fully occupying the available adsorption sites.

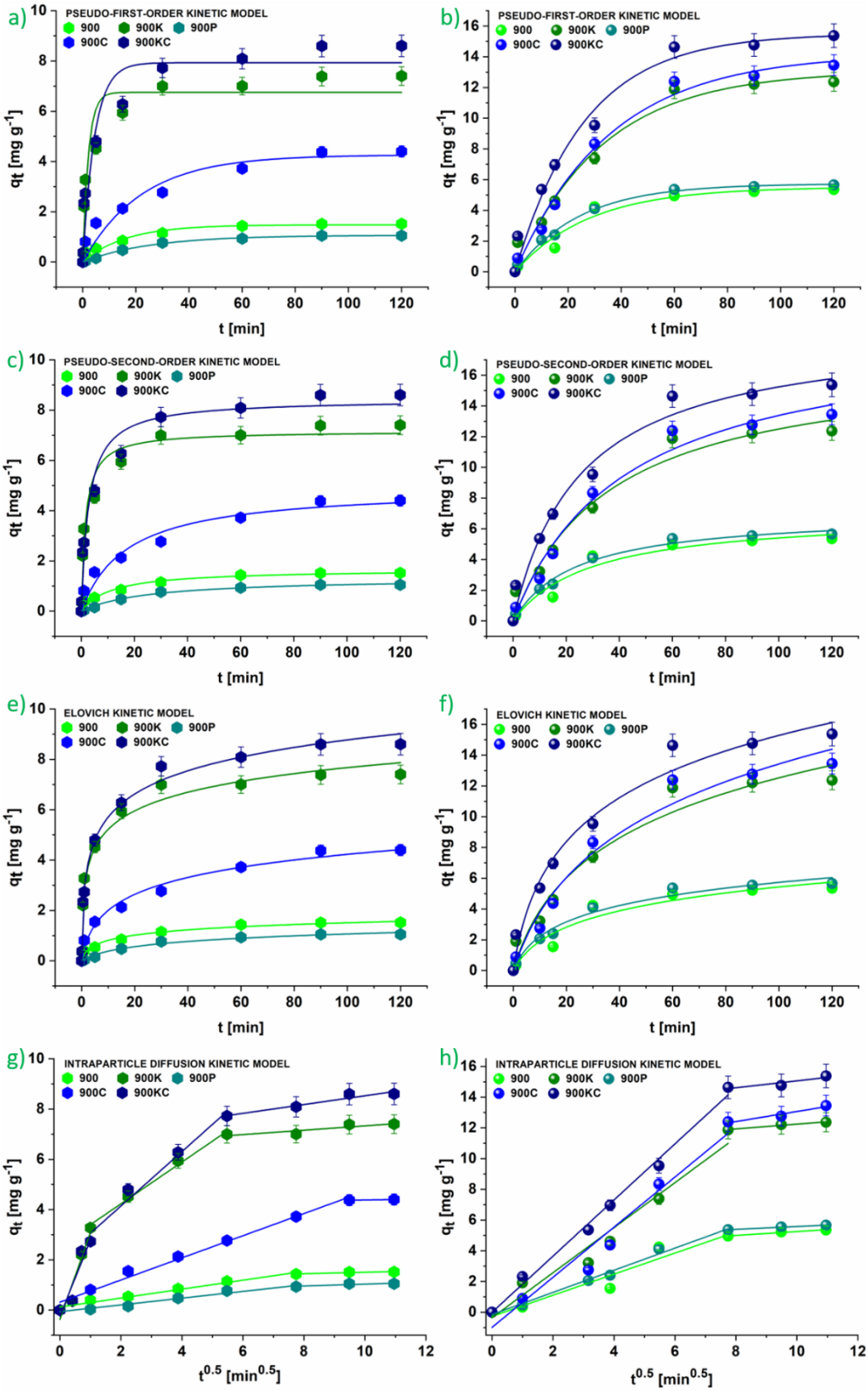

Figure 33. Graphical representation of kinetic models for MLT (left) and CHP (right) adsorption onto SCG materials thermochemically treated at 900°C: PFO (a,b), PSO (c,d), Elovich (e,f) and IPD (g,h)

Table 24. Kinetic parameters of MLT adsorption (5×10^{-5} mol dm^{-3}) onto SCG 900 materials (1 mg mL^{-1})

Material →	900	900K	900P	900C	900KC
Pseudo-first order model					
q_e (mg g^{-1})	1.48 ±0.07	6.75 ±0.09	1.07 ±0.01	4.26 ±0.08	7.93 ±0.08
$k_1\times10^2$ (min^{-1})	6.22 ±0.07	46.5 ±0.7	39.1 ±0.1	4.52 ±0.09	22.3 ±0.7
χ^2	0.022	0.665	0.001	0.190	0.839
R^2	0.934	0.921	0.997	0.929	0.927
Pseudo-second order model					
q_e (mg g^{-1})	1.67 ±0.05	7.17 ±0.03	1.32 ±0.01	4.93 ±0.05	8.43 ±0.04
$k_2\times10^2$ (mg min^{-1} g^{-1})	5.22 ±0.06	86.2 ±0.4	2.93 ±0.01	1.20 ±0.05	4.33 ±0.03
χ^2	0.014	0.250	0.002	0.119	0.346
R^2	0.957	0.970	0.993	0.956	0.970
Elovich kinetic model					
α (mg g^{-1} min^{-1})	0.389 ±0.004	14.0 ±0.4	0.0691 ±0.0002	0.618 ±0.002	9.34 ±0.01
β (g mg^{-1})	3.20 ±0.05	0.936 ±0.005	2.84 ±0.03	0.973 ±0.004	0.747 ±0.002
χ^2	0.008	0.212	0.004	0.051	0.129
R^2	0.977	0.975	0.981	0.981	0.989
Intraparticle diffusion model					
I part					
C (mg g^{-1})	0.123	−0.369	−0.061	0.316	−0.239
k_{id} (mg g^{-1} min$^{-0.5}$)	0.178	3.457	0.134	0.441	3.029
R^2	0.970	0.862	0.963	0.984	0.830
II part					
C (mg g^{-1})	1.224	2.569	0.663	4.204	1.978
k_{id} (mg g^{-1} min$^{-0.5}$)	0.028	0.831	0.037	0.018	1.082
R^2	0.675	0.988	0.592	--	0.966
III part					
C (mg g^{-1})	--	6.464	--	--	6.780
k_{id} (mg g^{-1} min$^{-0.5}$)	--	0.087	--	--	0.175
R^2	--	0.706	--	--	0.900

Table 25. Kinetic parameters of CHP adsorption (5×10^{-5} mol dm^{-3}) onto SCG 900 materials (1 mg mL^{-1})

Material →	900	900K	900P	900C	900KC
Pseudo-first order model					
qe ($mg\ g^{-1}$)	5.52 ±0.05	13.1 ±0.4	5.74 ±0.02	14.2 ±0.3	15.5 ±0.4
$k_1 \times 10^2$ (min^{-1})	3.61 ±0.06	3.02 ±0.05	4.11 ±0.02	2.84 ±0.02	3.81 ±0.05
χ^2	0.191	0.587	0.025	0.321	0.810
R^2	0.966	0.976	0.995	0.990	0.977
Pseudo-second order model					
qe ($mg\ g^{-1}$)	6.99 ±0.07	17.1 ±0.4	7.04 ±0.02	19.0 ±0.2	19.1 ±0.4
$k_2 \times 10^2$ ($mg\ min^{-1}\ g^{-1}$)	0.532 ±0.005	0.202 ±0.003	0.642 ±0.001	0.153 ±0.003	0.245 ±0.003
χ^2	0.261	0.776	0.054	0.580	0.808
R^2	0.954	0.969	0.990	0.981	0.977
Elovich kinetic model					
α ($mg\ g^{-1}\ min^{-1}$)	0.334 ±0.007	0.600 ±0.003	0.447 ±0.002	0.535 ±0.005	1.16 ±0.04
β ($g\ mg^{-1}$)	0.543 ±0.005	0.207 ±0.004	0.572 ±0.003	0.174 ±0.006	0.212 ±0.004
χ^2	0.345	0.992	0.107	0.891	0.907
R^2	0.939	0.960	0.980	0.971	0.974
Intraparticle diffusion model					
I part					
C ($mg\ g^{-1}$)	−0.270	−0.361	−0.152	−0.989	−0.006
k_{id} ($mg\ g^{-1}\ min^{-0.5}$)	0.687	1.466	0.721	1.631	1.828
R^2	0.912	0.955	0.988	0.948	0.992
II part					
C ($mg\ g^{-1}$)	4.009	10.684	4.658	9.799	12.809
k_{id} ($mg\ g^{-1}\ min^{-0.5}$)	0.124	0.156	0.092	0.327	0.226
R^2	0.949	0.950	0.985	0.905	0.684
III part					
C ($mg\ g^{-1}$)	--	--	--	--	--
k_{id} ($mg\ g^{-1}\ min^{-0.5}$)	--	--	--	--	--
R^2	--	--	--	--	--

5.6.2.2. Isotherm studies of MLT and CHP adsorption onto SCG 900 materials

The graphical representations of the experimental data for MLT and CHP adsorption onto SCG materials thermochemically treated at 900°C, along with the corresponding isotherm model fits, are shown in Figure 34 (MLT) and Figure 35 (CHP). The calculated parameters, including R^2 and χ^2, are provided in Table 26 (MLT) and Table 27 (CHP).

Based on the obtained parameters for pesticide adsorption, the experimental data fits well with both Freundlich and Langmuir isotherm models. However, the Langmuir isotherm model, according to R^2 and χ^2 values, provides a better description of the adsorption processes, suggesting that the adsorption occurs at well-defined and energetically homogeneous sites.

As the adsorption temperature increases, the n value, which indicates the favorability of the process, increases for MLT adsorption but decreases for CHP adsorption on all materials except 900K, where the opposite trend is observed for q_{max} values. Materials activated with KOH and physically activated materials show a significant increase in adsorption efficiency, while activation with H_3PO_4 negatively impacted adsorption compared to non-activated SCG. The highest amount of MLT adsorbed at 25°C is achieved by 900C (18.6±0.2 mg g^{-1}), at 30°C again by 900C (15.2±0.4 mg g^{-1}), and at 35°C by 900K (16.5±0.2 mg g^{-1}). On the other hand, for CHP adsorption, the highest q_{max} at 25°C is for 900KC (25.6±0.1 mg g^{-1}), at 30°C for 900C (27.2±0.1 mg g^{-1}), and at 35°C for 900C (31.8±0.3 mg g^{-1}). The variation in maximum adsorption capacities at different temperatures underscores the importance of considering adsorption temperature in these processes.

The parameters from the Temkin isotherm model align with these findings. The K_T binding constant and b_T values, related to adsorption heat, exhibit the same temperature trends as the n value from the Freundlich isotherm model. It can be seen that CHP adsorption generally has higher binding constant values but lower b_T values, indicating stronger binding of CHP than MLT on these materials. This is further supported by the Dubinin-Radushkevich isotherm parameter E, which is higher for CHP adsorption. The mean free energy values are significantly below 8000 J mol^{-1}, characterizing the adsorption processes of MLT and CHP on these materials as physisorption.

Overall, physical and chemical activations notably enhance the capacity for pesticide adsorption. For MLT and CHP adsorption onto SCG 900 materials at higher temperatures, physical activation has the most substantial positive effect. In contrast, chemical activation with KOH is the most influential factor for CHP adsorption at lower temperatures.

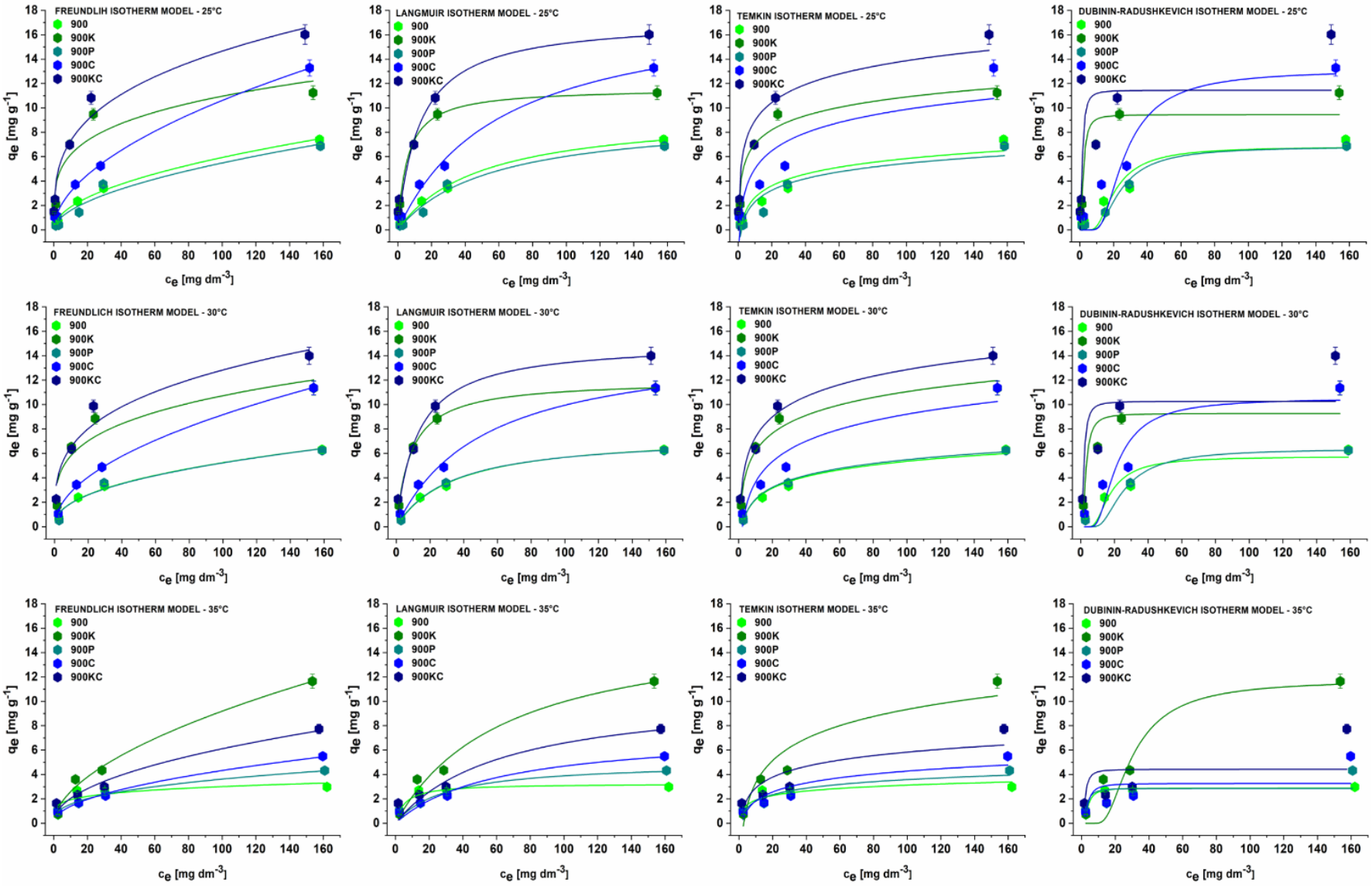

Figure 34. Graphical representations of experimental data for MLT adsorption onto SCG 900 materials fittings isotherm models at 25°C (top row), 30°C (middle row), and 35°C (bottom row)

Table 26. Isotherm adsorption parameters of MLT adsorption onto SCG 900 materials (1 mg mL^{-1}) at 25°C, 30°C, and 35°C

Material →	900			900K			900P			900C			900KC		
	25	30	35	25	30	35	25	30	35	25	30	35	25	30	35
Freundlich isotherm															
K_F ($(mg\ g^{-1})(dm^3\ g^{-1})^{1/n}$)	0.586 ±0.001	0.722 ±0.003	1.0 ±0.7	3.4 ±0.2	3.2 ±0.6	0.729 ±0.002	0.30 ±0.03	0.708 ±0.007	0.674 ±0.001	0.913 7±0.01	0.894 ±0.001	0.447 ±0.001	3.62 ±0.04	3.35 ±0.08	0.678 ±0.006
n	1.99 ±0.01	2.32 ±0.04	5 ±2	4.0 ±0.3	3.8 ±0.8	1.82 ±0.01	1.6 ±0.1	2.30 ±0.08	2.74 ±0.01	1.88 ±0.02	1.98 ±0.01	2.03 ±0.02	3.29 ±0.06	3.43 ±0.05	2.10 ±0.05
χ^2	0.058	0.127	0.622	2.816	3.300	0.343	1.103	0.603	0.022	0.083	0.056	0.046	1.266	1.925	0.414
R^2	0.993	0.977	0.440	0.853	0.803	0.984	0.870	0.927	0.989	0.997	0.997	0.989	0.965	0.923	0.946
Langmuir isotherm															
$K_L \times 10^2$ ($dm^3\ mg^{-1}$)	2.02 ±0.07	2.93 ±0.01	18 ±2	17.5 ±0.5	11.6 ±0.1	1.52 ±0.03	1.21 ±0.08	3.01 ±0.01	3.4 ±0.7	16.0 ±0.2	1.91 ±0.03	1.69 ±0.05	7.71 ±0.04	7.92 ±0.05	1.6 ±0.4
q_{max} ($mg\ g^{-1}$)	9.64 ±0.01	7.63 ±0.02	3.3 ±0.2	11.6 ±0.2	12.0 ±0.1	16.5 ±0.2	10.6 ±0.4	7.56 ±0.01	5.0 ±0.2	18.6 ±0.2	15.2 ±0.4	7.51 ±0.07	17.3 ±0.3	15.1 ±0.4	11 ±1
χ^2	0.056	0.044	0.132	0.351	0.013	0.625	0.888	0.004	0.248	0.511	0.269	0.270	1.336	0.686	1.102
R^2	0.993	0.992	0.881	0.982	0.999	0.971	0.900	1.000	0.878	0.980	0.986	0.933	0.963	0.973	0.856
Temkin isotherm															
K_t ($dm^3\ mg^{-1}$)	0.68 ±0.02	0.495 ±0.003	3.6 ±0.9	6.66 ±0.06	1.84 ±0.04	0.36 ±0.06	0.5 ±0.1	0.494 ±0.002	1.1 ±0.2	1.1 ±0.5	0.45 ±0.02	0.56 ±0.07	6.73 ±0.09	2.10 ±0.05	0.98 ±0.08
b_t ($J\ g\ mol^{-1} mg^{-1}$)	1800 ±200	1840 ±30	4800 ±800	1480 ±60	1190 ±50	980 ±60	1900 ±500	1790 ±10	3400 ±100	1200 ±400.	1000 ±10	2400 ±200	1160 ±80	1050 ±40	2000 ±300
χ^2	0.888	0.201	0.418	1.216	0.731	2.754	2.560	0.056	0.285	5.909	2.320	0.919	2.985	0.737	2.777
R^2	0.888	0.964	0.624	0.936	0.956	0.872	0.699	0.993	0.860	0.766	0.881	0.773	0.918	0.971	0.636
Dubinin-Radushkevich isotherm															
$K_{DR} \times 10^6$ ($mol^2\ J^{-2}$)	5.7 ±0.7	3.9 ±0.9	0.202 ±0.001	0.082 ±0.007	0.14 ±0.07	11 ±2	10.1 ±0.3	8.18 ±0.06	0.13 ±0.09	9.2 ±0.9	5.6 ±0.9	0.19 ±0.09	0.04 ±0.01	0.06 ±0.04	0.07 ±0.06
q_{DR} ($mg\ g^{-1}$)	6.8 ±0.5	5.7 ±0.8	2.9 ±0.2	9.5 ±0.3	9.3 ±0.9	11.7 ±0.9	7.12 ±0.03	6.38 ±0.04	3 ±2	13 ±2	11 ±1	3 ±2	11 ±5	10 ±4	4 ±3
E ($J\ mol^{-1}$)	94 ±2	110 ±30	500 ±50	820 ±20	600 ±60	68 ±7	70.0 ±0.3	78.0 ±0.7	600 ±500	74 ±3	100 ±30	500 ±400	1100 ±400	900 ±400	800 ±700
χ^2	1.201	1.139	0.008	3.157	4.433	6.267	0.136	0.277	1.787	4.736	4.783	3.993	13.66	13.50	8.484
R^2	0.848	0.796	0.993	0.835	0.736	0.709	0.984	0.966	0.120	0.812	0.755	0.014	0.623	0.461	0.111

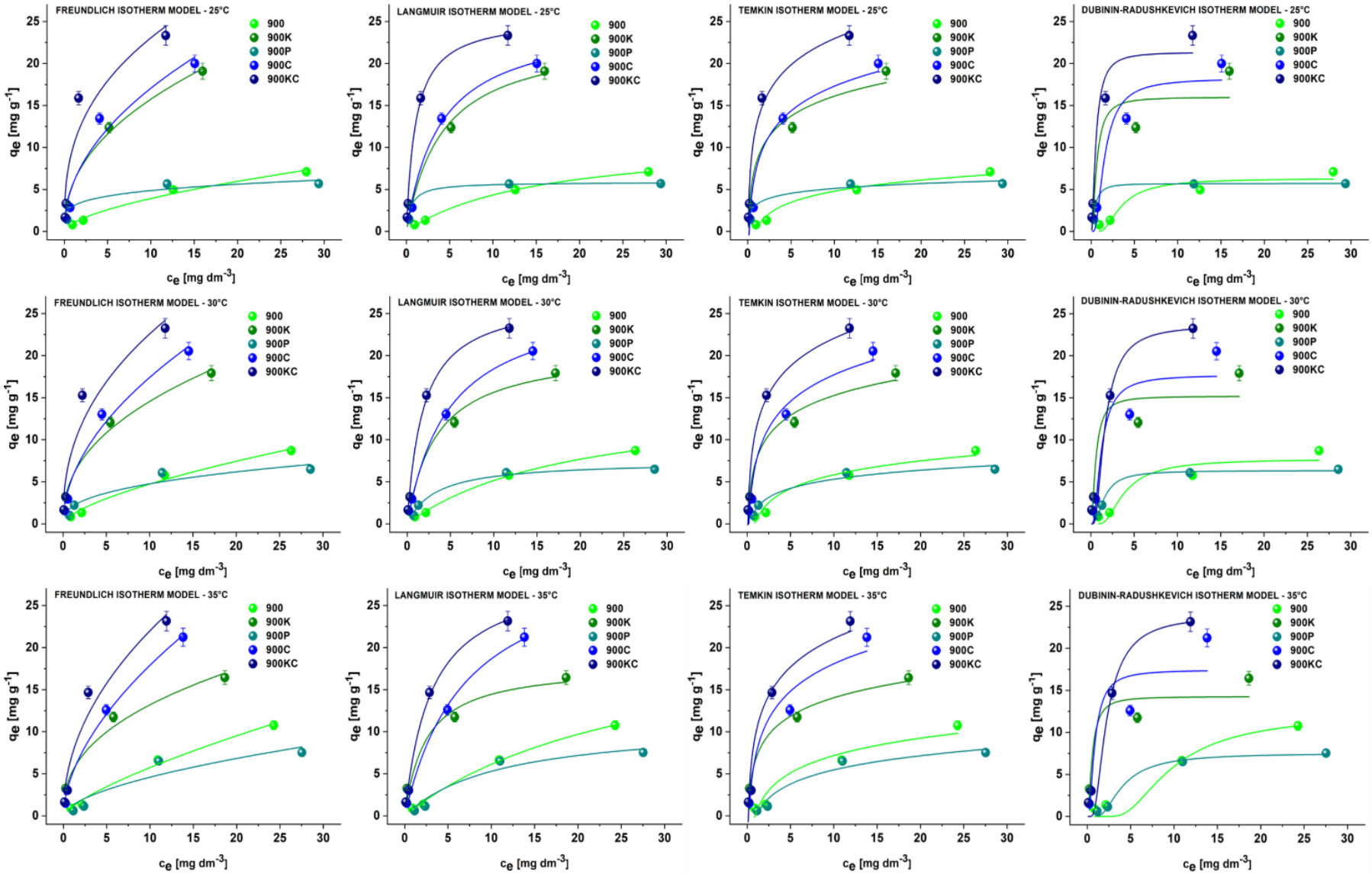

Figure 35. Graphical representations of experimental data for CHP adsorption onto SCG 900 material fittings isotherm models at 25°C (top row), 30°C (middle row), and 35°C (bottom row)

Table 27. Isotherm adsorption parameters of CHP adsorption onto 900-series materials (1 mg mL^{-1}) at 25°C, 30°C, and 35°C

Material →	900			900K			900P			900C			900KC		
	25	30	35	25	30	35	25	30	35	25	30	35	25	30	35
Freundlich isotherm															
K_F ($(mg\ g^{-1})(dm^3\ g^{-1})^{1/n}$)	0.980 ±0.002	1.05 ±0.02	1.08 ±0.02	5.70 ±0.02	5.43 ±0.02	5.22 ±0.04	3.0 ±0.9	2.0 ±0.5	1.2 ±0.3	5.64 ±0.08	5.31 ±0.04	4.92 ±0.01	10 ±1	8.59 ±0.09	7.26 ±0.06
n	1.66 ±0.04	1.53 ±0.03	1.38 ±0.01	2.26 ±0.01	2.34 ±0.04	2.48 ±0.05	4.8 ±0.9	2.7 ±0.3	1.8 ±0.2	2.08 ±0.04	1.94 ±0.02	1.78 ±0.01	2.8 ±0.6	2.38 ±0.06	2.08 ±0.04
χ^2	0.162	0.243	0.279	0.361	0.888	1.847	0.965	1.025	2.259	5.028	2.085	0.486	12.76	9.116	6.252
R^2	0.982	0.983	0.987	0.995	0.985	0.963	0.777	0.864	0.824	0.935	0.974	0.994	0.881	0.914	0.940
Langmuir isotherm															
$K_L \times 10^2$ ($dm^3\ mg^{-1}$)	6.5 ±0.1	5.1 ±0.1	3.6 ±0.1	24.3 ±0.3	29.7 ±0.7	40.8 ±0.4	180 ±20	30.3 ±0.2	9.1 ±0.6	25.7 ±0.1	20.9 ±0.1	14.2 ±0.2	94.1 ±0.2	54.1 ±0.1	32.9 ±0.1
q_{max} ($mg\ g^{-1}$)	11.0 ±0.1	15.2 ±0.1	23.2 ±0.1	23.6 ±0.2	20.9 ±0.6	18.0 ±0.4	5.9 ±0.6	7.47 ±0.03	11.1 ±0.8	25.4 ±0.2	27.2 ±0.1	31.8 ±0.3	25.6 ±0.1	27.1 ±0.2	29.3 ±0.1
χ^2	0.012	0.033	0.071	2.022	1.903	1.815	0.578	0.120	0.987	0.712	0.111	1.037	0.183	0.511	0.730
R^2	0.999	0.998	0.997	0.970	0.968	0.964	0.867	0.984	0.923	0.991	0.999	0.988	0.998	0.995	0.993
Temkin isotherm															
K_t ($dm^3\ mg^{-1}$)	1.21 ±0.06	1.15 ±0.06	1.11 ±0.09	0.11 ±0.01	8.80 ±0.04	8.54 ±0.04	44 ±2	3.03 ±0.03	0.95 ±0.01	5.76 ±0.09	4.89 ±0.06	4.67 ±0.04	16.1 ±0.2	10.4 ±0.6	7.53 ±0.07
b_t ($J\ g\ mol^{-1}mg^{-1}$)	1290 ±40	1060 ±60	859 ±7	722 ±7	740 ±7	811 ±5	2900 ±400	1620 ±30	1060 ±20	581 ±9	553 ±9	544 ±6	548 ±5	531 ±9	525 ±8
χ^2	0.378	0.890	2.081	3.287	1.014	0.887	0.770	0.285	0.844	6.782	3.633	3.927	2.415	4.961	8.708
R^2	0.958	0.937	0.905	0.951	0.983	0.982	0.822	0.962	0.934	0.913	0.955	0.953	0.978	0.953	0.916
Dubinin-Radushkevich isotherm															
$K_{DR} \times 10^6$ ($mol^2\ J^{-2}$)	1.9 ±0.5	0.471 ±0.005	12.2 ±0.4	0.13 ±0.03	0.31 ±0.06	0.10 ±0.02	0.085 ±0.002	0.503 ±0.007	2.34 ±0.05	0.489 ±0.007	0.252 ±0.003	0.18 ±0.03	0.112 ±0.004	0.77 ±0.01	0.823 ±0.006
q_{DR} ($mg\ g^{-1}$)	6.3 ±0.4	7.72 ±0.02	12.2 ±0.9	16 ±2	15 ±3	14 ±1	5.7 ±0.1	6.34 ±0.06	7.5 ±0.3	18.2 ±0.6	17.7 ±0.2	17.4 ±0.7	21.4 ±0.6	24 ±5	23.9 ±0.8
E ($J\ mol^{-1}$)	510 ±10	1040 ±20	201 ±9	2000 ±200	1300 ±100	2200 ±200	2500 ±100	1000 ±50	460 ±20	1020 ±50	1420 ±20	1650 ±50	2160 ±80	810 ±90	780 ±40
χ^2	1.142	0.098	1.338	11.215	11.404	5.581	0.484	6.321	0.203	6.852	90.277	16.462	7.104	4.739	5.857
R^2	0.874	0.987	0.939	0.833	0.858	0.888	0.888	0.940	0.984	0.912	0.981	0.805	0.934	0.897	0.944

5.6.2.3. Thermodynamic study of MLT and CHP adsorption onto SCG 900 materials

Thermodynamics of the adsorption processes have also been investigated, and Figure 36 shows Van't Hoff plots for OPs' adsorption onto these materials. The obtained thermodynamic parameters with corresponding R^2 values are given in Table 28.

The obtained thermodynamic parameters show that the adsorption of MLT onto all materials is spontaneous, as evidenced by the negative change in Gibbs free energy across all cases and temperatures. The adsorption generally leads to a decrease in both enthalpy and entropy, suggesting it is exothermic and results in a more ordered system. However, there is an exception in the case of adsorption onto 900K material, where the process is slightly endothermic and entropically driven, indicating a unique interaction where adsorption may be facilitated by increased randomness and energy absorption.

Also, for CHP adsorption onto these materials, the thermodynamic data indicate spontaneous adsorption onto all materials, with Gibbs free energy changes remaining negative. The adsorption is exothermic when the material is KOH-activated, implying strong interactions that release heat. Conversely, with non-KOH activated materials, the process becomes endothermic, suggesting that energy input is required for adsorption, possibly due to weaker or less efficient interactions between CHP molecules and the adsorbent surfaces.

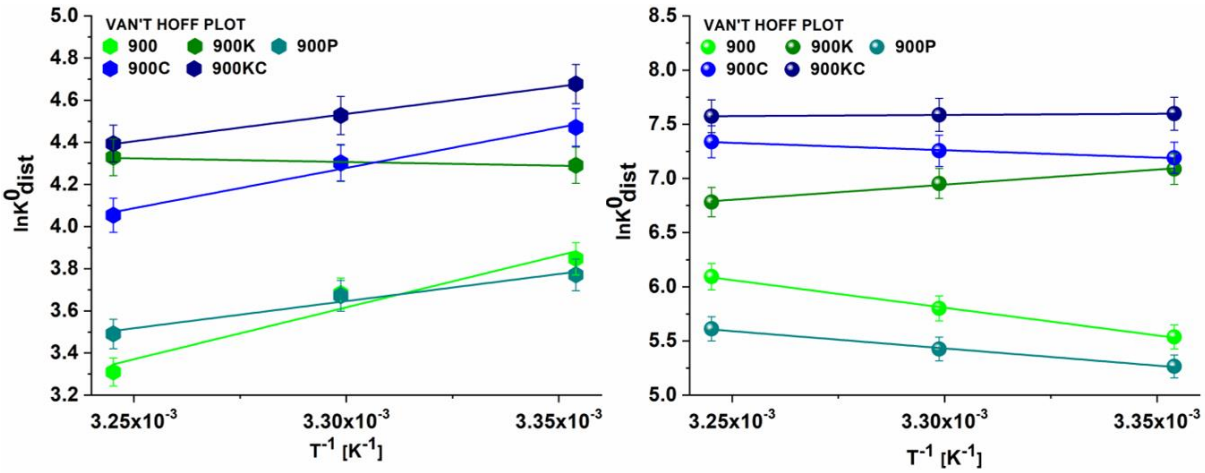

Figure 36. Van't Hoff plots for MLT (left) and CHP (right) adsorption onto SCG materials thermochemically treated at 900°C

Table 28. Thermodynamic parameters of adsorption of MLT and CHP onto SCG 900 materials

		ΔH^0 (kJ mol^{-1})	ΔS^0 (J mol^{-1}K^{-1})	ΔG^0 (kJ mol^{-1})			R^2
T (°C) →				**25**	**30**	**35**	
MLT	900	−40.9 ±0.9	−105 ±8	−9.94 ±0.08	−9.10 ±0.07	−8.57 ±0.07	0.897
	900K	2.9 ±0.4	45 ±5	−10 ±1	−11 ±1	−11 ±1	0.834
	900P	−21.4 ±0.6	−40.3 ±0.7	−9.50 ±0.05	−9.18 ±0.04	−8.98 ±0.04	0.938
	900C	−31.8 ±0.3	−69.3 ±0.2	−11.3 ±0.3	−10.8 ±0.3	−10.4 ±0.2	0.970
	900KC	−21.6 ±0.1	−33.6 ±0.1	−11.7 ±0.1	−11.4 ±0.1	−11.2 ±0.1	0.999
CHP	900	42.5 ±0.1	188 ±3	−13.1 ±0.2	−14.6 ±0.2	−15.6 ±0.2	0.996
	900K	−23.2 ±0.1	−18.9 ±0.1	−17.6 ±0.1	−17.5 ±0.1	−17.4 ±0.1	0.987
	900P	26.5 ±0.3	132 ±4	−12.6 ±0.3	−13.7 ±0.3	−14.4 ±0.3	0.995
	900C	11.2 ±0.2	97.4 ±0.3	−17.5 ±0.3	−18.3 ±0.3	−18.8 ±0.4	0.985
	900KC	−1.78 ±0.02	57.2 ±0.3	−18.7 ±0.3	−19.1 ±0.3	−19.4 ±0.3	0.987

5.6.3. Discussion on MLT and CHP adsorption onto SCG materials 900

The SEM micrographs demonstrate that the porous, spongy-like structure of SCG materials is retained post-activation at 900°C, with pores heterogeneously distributed. This indicates that the original morphology of raw SCG is preserved despite the high-temperature treatment and activation processes. The elemental composition analysis reveals high percentages of C, O, and N, reflecting the organic nature of SCG. Notably, the C content exceeds 75 at.% across all materials. Activation, particularly with KOH, significantly increases O content, indicating the formation of oxygen-containing surface functional groups essential for adsorption processes. FTIR spectra show that thermochemical treatment at 900°C results in minimal functional groups, similar to materials treated at 650°C. However, KOH activation introduces several functional groups, which is evident from the additional bands. These changes suggest the formation of specific functional groups that enhance adsorption capabilities. Zeta potential measurements indicate slightly negatively charged surfaces for all materials under the experimental conditions, with isoelectric points ranging from 3.39 to 5.58. BET and total pore volume measurements reveal that increasing the thermochemical treatment temperature enhances the specific surface area and total pore volume, particularly with physical activation. However, KOH activation reduces these values, suggesting a trade-off between surface functionalization and porosity.

The adsorption kinetics of MLT and CHP indicate rapid adsorption within 60 min, with data fitting well to both PFO and PSO kinetic models. MLT adsorption is faster than CHP, but CHP exhibits higher

equilibrium adsorption capacities. This can be attributed to the different structures of these molecules. While MLT is a smaller, aliphatic molecule, it enters pores of the material faster, while CHP, being aromatic, can stack due to π-π interactions. Activation processes, especially with KOH and CO_2, significantly enhance adsorption efficiency, improving q_e up to five times compared to non-activated materials. The Elovich model and IPD kinetic model analyses further corroborate these findings, highlighting the influence of activation on adsorption kinetics and mechanisms.

Isotherm studies show that adsorption data fit well with both Freundlich and Langmuir models, with Langmuir providing a slightly better fit. This suggests adsorption occurs on energetically homogeneous sites. The maximum adsorption capacities vary with temperature, indicating the importance of adsorption temperature. CHP adsorption capacity is highest at 900C at 35°C, while MLT adsorption is highest at 900C at 25°C. Thermodynamic parameters indicate spontaneous adsorption of both MLT and CHP, with negative ΔG^0 values. MLT adsorption is generally exothermic and leads to a more ordered system, except for 900K, where the process is slightly endothermic and entropically driven. Conversely, CHP adsorption is exothermic for KOH-activated materials and endothermic for others, suggesting stronger interactions in KOH-activated materials that release heat during adsorption.

Overall, the adsorption of MLT and CHP onto SCG 900 materials is significantly influenced by the activation process and temperature. Physical activation enhances porosity and surface area, improving adsorption capacity, while chemical activation, particularly with KOH, introduces functional groups that enhance adsorption efficiency despite reducing porosity. The kinetic, isotherm, and thermodynamic analyses collectively indicate that activation processes and adsorption conditions must be carefully considered to optimize the adsorption performance of SCG-based adsorbents for OP removal.

5.7. SCG material 900PC

5.7.1. Characterization of SCG material 900PC

SEM micrography and EDX analysis were performed to examine the morphology and elemental composition of materials. The SEM micrograph and EDX spectrum are given in Figure 37. On the SEM micrograph, it can be seen that the material has a granular, heterogeneous, and highly porous structure, resembling the previously reported morphology of the precursor. EDX analysis revealed a high percentage of C, O, and P (46.27, 36.76, and 6.97 at.%, respectively. Besides mentioned, N, K, Ca, Mg, Na, and Si are also present in the sample as the chemical footprint of the precursor.

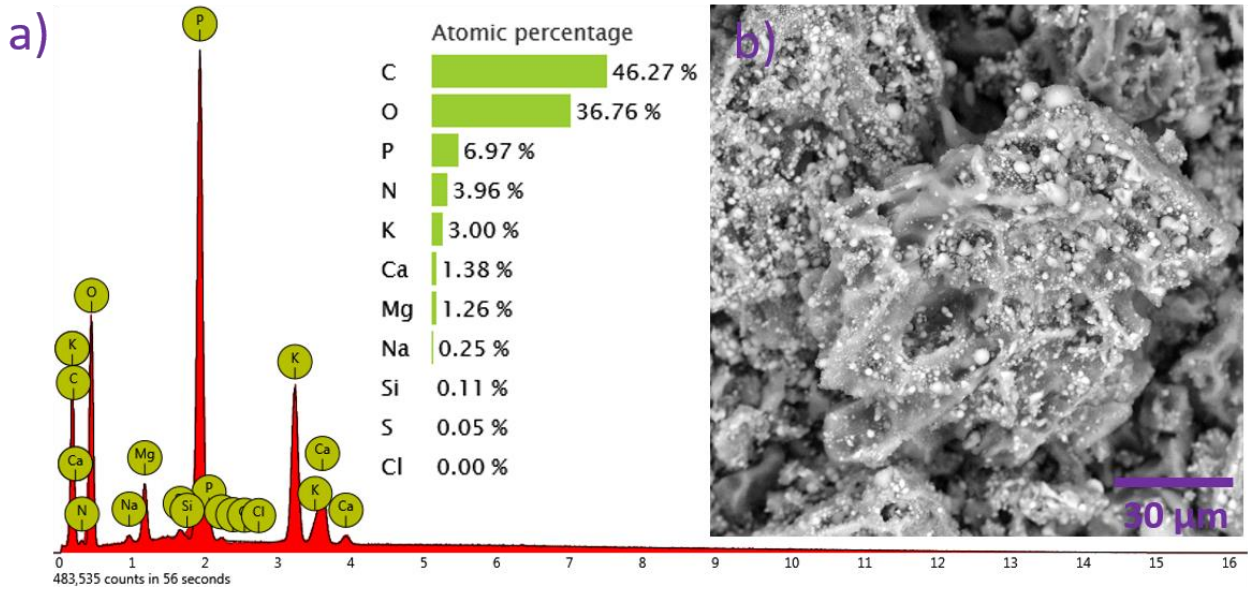

Figure 37. a) EDX spectrum and elemental composition in at.% of 900PC; b) SEM micrograph of 900PC (magnification 2000×)

The crystalline structure of 900PC is examined using XRD, and the obtained diffractogram is given in Figure 38. XRD diffraction pattern of 900PC shows two reflections characteristic of graphitic carbon, located at 2θ around 27° and 44°. It confirms the dominant carbon structure of the sample in line with the chemical composition determined by EDX.

The FTIR spectrum of 900PC is given in Figure 38. The observed bands in the spectrum correspond to specific vibrations. The band at 1554 cm^{-1} indicates the presence of condensed aromatic rings, signifying aromatic carbon-carbon double bonds (C=C) within the carbon structure. These aromatic rings enhance the material's π-electron system, improving its adsorption properties through π-π interactions with adsorbates. The band at 1227 cm^{-1} is assigned to the stretching vibration of phosphorus-oxygen double bonds (P=O), suggesting the presence of phosphorus-containing functional groups. These groups may stem from phosphorus compounds in the precursor material or be introduced during the carbonization and activation processes, potentially enhancing the material's adsorption affinity for certain contaminants. The band at 1079 cm^{-1} is linked to the coupling of aromatic carbon-hydrogen (C-H) in-plane deformation vibrations and carbon-oxygen (C-O) stretch vibrations in primary alcohols, indicating the presence of aromatic C-H bonds and hydroxyl (OH) functional groups, likely derived from phenolic compounds in the precursor material. These functional groups contribute to the material's hydrophilicity

and surface reactivity, affecting its adsorption behavior towards polar contaminants [90]. The band at 877 cm^{-1} corresponds to vibrations from 3-4 condensed aromatic rings, pointing to carbonaceous structures with multiple fused aromatic rings. These condensed aromatic structures enhance the material's graphitic nature and provide additional adsorption sites for contaminants through π-π interactions [95].

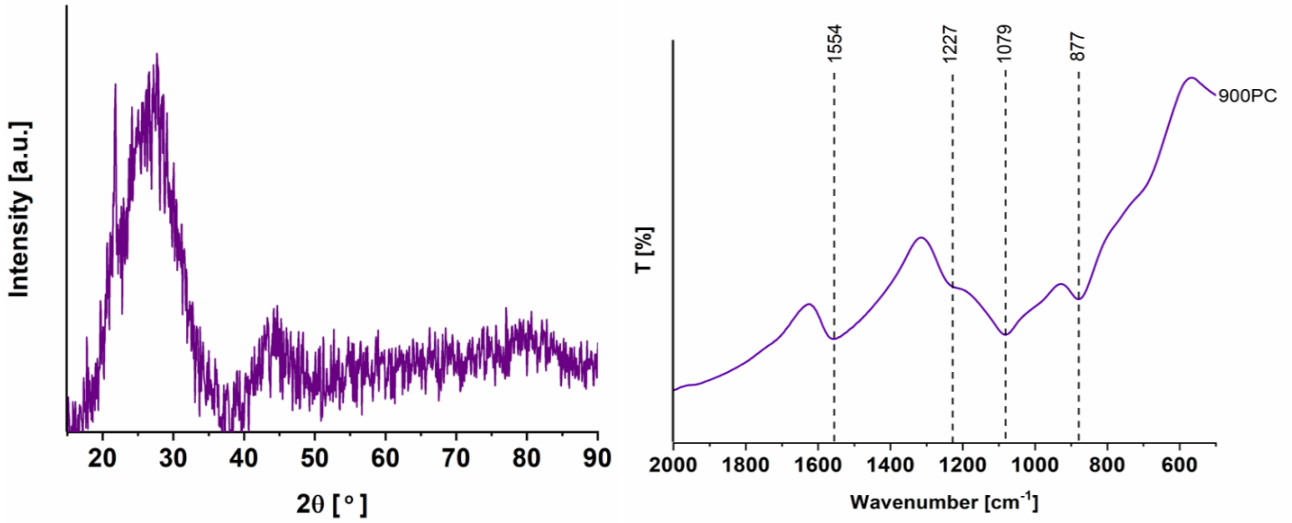

Figure 38. XRD diffraction pattern of 900PC sample (left); FTIR spectrum of 900PC (right)

Due to the relatively high carbonization temperature, it is anticipated that the degree of graphitization is high, implying that the graphitization process is complete. The Raman spectrum (Figure 39) exhibits typical characteristics of disordered carbon, which can be attributed to the presence of various functional groups on the surface, as observed in the FTIR analysis, leading to defects. The I_D/I_G ratio was determined to be 2.04, indicating that the material is disordered with crystallite sizes smaller than 10 nm. This observation is consistent with the broad (002) reflection seen in the XRD analysis.

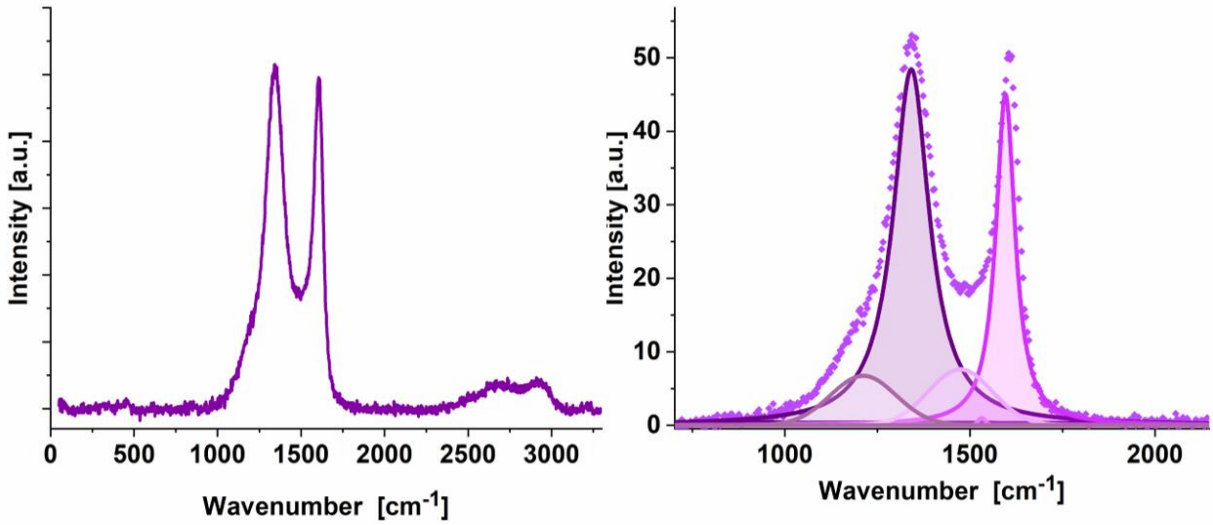

Figure 39. Recorded Raman spectra of the SCG-900PC sample (left) and deconvolved G and D region of the Raman spectra, split into five components

In addition to FTIR analysis, surface functional groups were quantified using Boehm titration. The titration curves given in Figure 40 reveal that no carboxyl groups are present on the material's

surface. Conversely, titration experiments with Na_2CO_3 and NaOH onto 900PC demonstrate the presence of lactone and phenol functional groups. During the Na_2CO_3 titration, the equivalence point is reached at pH 6.33 after adding 5.68×10^{-5} dm³ of titrant, indicating the combined presence of carboxyl and lactone functional groups at a concentration of 0.057 mmol g^{-1}. Since carboxyl groups are absent, this amount corresponds solely to lactone groups. Similarly, in the NaOH titration, the equivalence point (pH = 7.95) is achieved after adding 2.50×10^{-4} dm³ of titrant, neutralizing 2.50×10^{-6} mol of carboxyl, lactone, and phenol functional groups on the surface of 10 mg of the material. Given that lactone and phenol groups are the only acidic groups present, subtracting the lactone content yields the phenol content at 0.193 mmol g^{-1}. This finding aligns with the FTIR analysis, which indicates the presence of aromatic rings and hydroxyl groups, both characteristic of phenol functional groups.

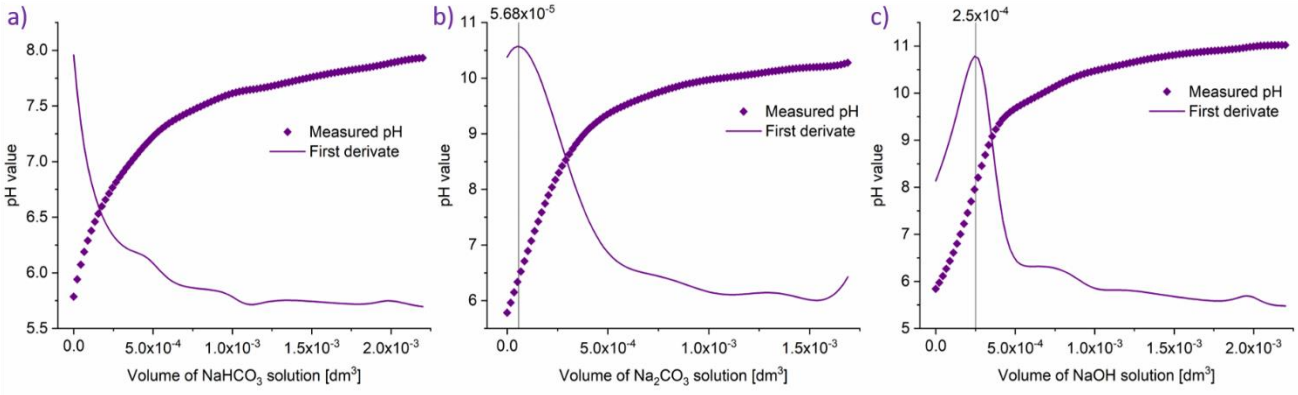

Figure 40. Titration curves and their first derivates of 1 mg mL^{-1} SCG-900PC suspension titrated with 0.01 mol dm^3 a) $NaHCO_3$, b) Na_2CO_3, and c) NaOH

By examining the dependence of zeta potential of the materials' suspension with pH (Figure 41), it can be seen that the isoelectric point of 900PC is at pH=4.87, and as the initial pH value of the suspension used in adsorption experiments was 6, it can be concluded that 900PC has a slightly negatively charged surface.

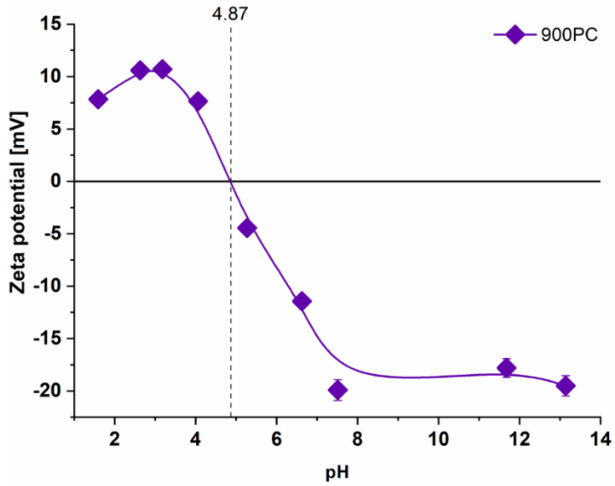

Figure 41. Dependence of zeta potential of pH with indicated IEP for 900PC

The specific surface area of 900PC determined by N_2 adsorption is found to be 846 $m^2\ g^{-1}$, while the total pore volume is 0.557 $cm^3\ g^{-1}$.

5.7.2. Adsorption of MLT and CHP onto SCG material 900PC

5.7.2.1. Kinetic studies of MLT and CHP adsorption onto SCG material 900PC

The graphical representations of kinetic models in Figure 42 shows that equilibrium for adsorption was achieved within the initial 10 minutes for MLT and 30 min for CHP adsorption, indicating rapid adsorption of these compounds onto 900PC. Upon examining the results in Table 29, it becomes apparent that experimental data for both pesticides align well with PFO and PSO kinetic models, as indicated by the high R^2 and low χ^2 values. The q_e and k values obtained from both kinetic models are similar, confirming both fits' robustness. Additionally, even though experimental data do not fit the Elovich kinetic model very well, parameters α and β suggest a high initial adsorption rate and very low desorption constant, particularly for CHP adsorption. With α being significantly greater than β, it is evident that the adsorption of these pesticides onto 900PC is a favorable process. The high initial adsorption rate ensures rapid removal of pesticides from wastewater, making this material suitable for applications requiring fast treatment processes or dealing with high pollutant concentrations. Moreover, the IPD kinetic model plot displays three linear stages for MLT and CHP. As previously stated, the initial stage signifies the diffusion to the external surface of the material, followed by intraparticle diffusion and, finally, the equilibrium stage. The breaking point for the adsorption of these pesticides onto 900PC is observed within the first minute, after which the adsorption rate decreases, finally reaching equilibrium after 60 minutes. The decline in k_{id} values across stages corresponds to the gradual slowing down of the adsorption process as the boundary layer value increases through the stages, signifying an increase in the molecules adsorbed on the material's surface. Ultimately, the boundary layer reaches a value similar to q_e values obtained from PFO and PSO, and k_{id} values nearly reach zero, signifying the completion of the adsorption process.

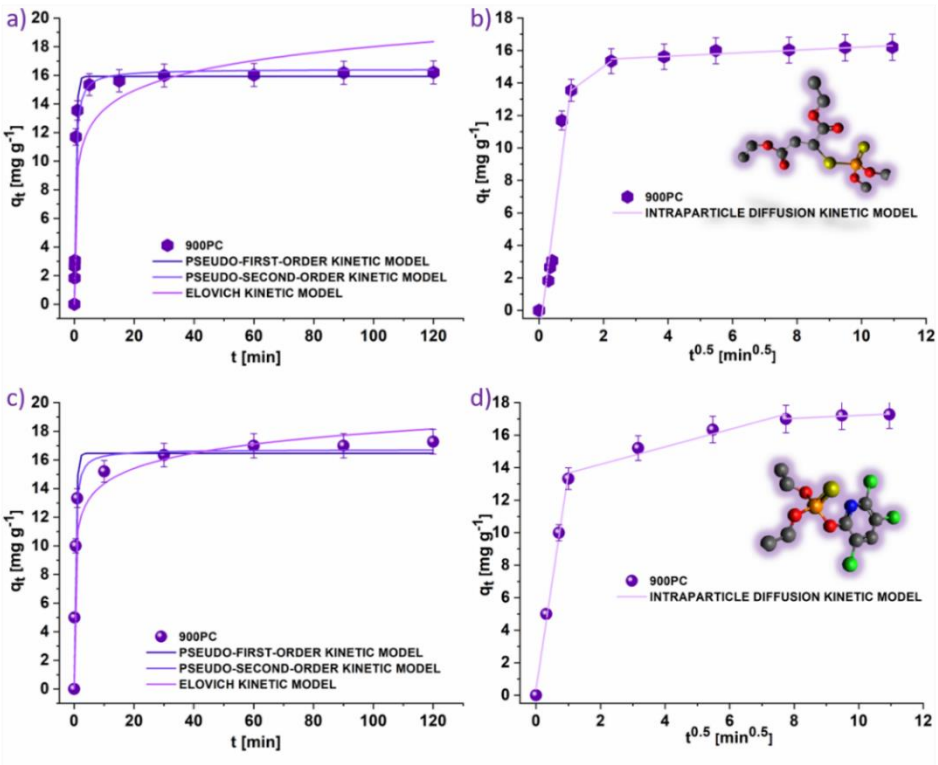

Figure 42. Graphical representations of kinetic models for MLT (a,b), and CHP (c,d) adsorption onto 900PC

Table 29. Kinetic parameters of MLT and CHP adsorption on 900PC (1 mg mL^{-1}) at 25°C

OP→	**MLT**	**CHP**
	Pseudo-first-order kinetic model	
q_e ($mg\ g^{-1}$)	15.9 ±0.4	16.5 ±0.3
$k_1 \times 10^2$ (min^{-1})	200 ±20	195 ±2
χ^2	0.768	1.35
R^2	0.98	0.929
	Pseudo-second-order kinetic model	
q_e ($mg\ g^{-1}$)	16.5 ±0.6	16.7 ±0.3
$k_2 \times 10^2$ ($mg\ min^{-1}\ g^{-1}$)	16 ±4	21 ±3
χ^2	1892	0.459
R^2	0.95	0.976
	Elovich kinetic model	
α ($mg\ g^{-1}\ min^{-1}$)	200 ±10	31000 ±8000
β ($g\ mg^{-1}$)	0.5 ±0.1	0.9 ±0.1
χ^2	8.58	4.66
R^2	0.773	0.757
	Intraparticle diffusion model	
I part		
C ($mg\ g^{-1}$)	−3.39	1.21
k_{id} ($mg\ g^{-1}\ min^{-0.5}$)	18.11	12.21
R^2	0.920	0.998
II part		
C ($mg\ g^{-1}$)	12.10	12.80
k_{id} ($mg\ g^{-1}\ min^{-1}$)	1.45	0.67
R^2	--	0.949
III part		
C ($mg\ g^{-1}$)	15.20	16.28
k_{id} ($mg\ g^{-1}\ min^{-0.5}$)	0.11	0.03
R^2	0.856	0.893

5.7.2.2. Isotherm studies of MLT and CHP adsorption onto SCG material 900PC

The graphical representations of the experimental data for MLT and CHP adsorption onto 900PC, along with the corresponding isotherm model fits, are shown in Figure 43, and the calculated parameters, including R^2 and χ^2, are provided in Table 30.

The results show that both Freundlich and Langmuir isotherm models effectively describe the adsorption of MLT and CHP onto 900PC. The strong fit of the Langmuir isotherm model with the experimental data suggests the initial formation of a monolayer due to adsorption at very well-defined sites. The fit of the Freundlich isotherm model with the experimental data indicates that the adsorbent surface is not uniform and possesses energetically diverse adsorption sites. Given that the Freundlich isotherm model also accounts for multilayer adsorption, it can be suspected that molecules are adsorbed in multiple layers on the material's surface. Combining the assumptions of these two models, it can be concluded that the adsorption of pesticides onto 900PC is a complex process involving both monolayer and multilayer adsorption on a heterogeneous surface.

As all values of the parameter n in the Freundlich isotherm model are greater than 1, it can be concluded that the adsorption of MLT and CHP onto 900PC is favorable. The decrease in the parameter n with increasing temperature indicates a decline in the material's affinity for the investigated OPs as temperature rises.

Considering the q_{max} values obtained from the Langmuir isotherm model, 900PC shows higher maximum adsorption capacities for OPs with increasing temperature. The q_{max} value increases 2.5 times (from 72.1 to 183 mg g^{-1}) for MLT adsorption and 1.25 times (from 193 to 240 mg g^{-1}) for CHP adsorption as the adsorption temperature changes from 25°C to 35°C. The K_L and K_F values indicate that the interactions between 900PC and MLT decrease with increasing temperature, while they increase in the case of CHP.

The parameters of the Temkin isotherm model align with these observations. The K_T binding constant and b_T value, which is related to adsorption heat, decrease with increasing temperature for MLT and increase for CHP. The mean free energy values of adsorption obtained from the Dubinin-Radushkevich isotherm model are all below 8 kJ mol^{-1}, indicating that the adsorption process of MLT and CHP onto 900PC is predominantly physisorption.

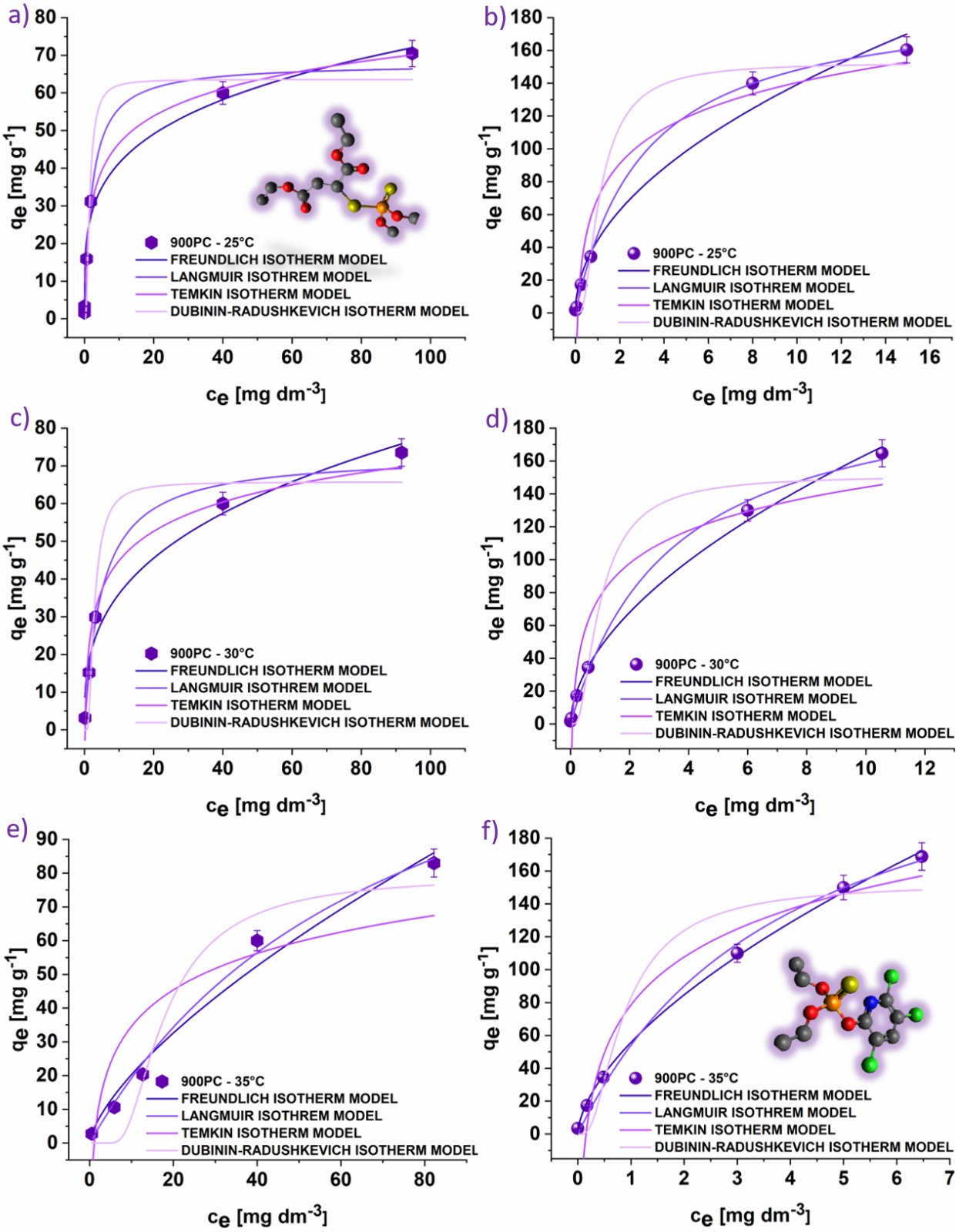

Figure 43. Graphical representations of isotherm models for MLT (a,c,e) and CHP (b,d,f) adsorption onto 900PC (1 mg mL^{-1}) at 25°C (a,b), 30°C (c,d), and 35°C (e,f)

Table 30. Isotherm adsorption parameters of MLT and CHP adsorption onto 900PC (1 mg mL^{-1}) at 25°C, 30°C, and 35°C

	MLT			CHP		
T (°C)	**25**	**30**	**35**	**25**	**30**	**35**
Freundlich isotherm						
K_F ($(dm^3 mg^{-1})^{1/n}$)	23.0 ±0.3	16.2 ±0.3	2.94 ±0.04	37.9 ±0.1	43.58 ±0.01	53.31 ±0.01
n	4.05 ±0.05	2.96 ±0.04	1.32 ±0.02	1.88 ±0.02	1.77 ±0.01	1.62 ±0.01
χ^2	25.5	35.9	0.686	13.1	4.99	6.59
R^2	0.970	0.962	0.999	0.997	0.999	0.999
Langmuir isotherm						
$K_L \times 10^2$ ($dm^3 mg^{-1}$)	42.8 ±0.3	19.3 ±0.1	1.0 ±0.1	32.7 ±0.1	34.4 ±0.1	36.5 ±0.1
q_{max} ($mg g^{-1}$)	72.1 ±0.6	77.7 ±0.2	183 ±1	193 ±1	210 ±1	240 ±1
χ^2	6.01	1.00	1.82	3.62	4.96	11.7
R^2	0.993	0.999	0.999	0.999	0.999	0.998
Temkin isotherm						
K_T ($dm^3 mg^{-1}$)	8.48 ±0.05	5.46 ±0.09	0.9 ±0.1	9.8 ±0.1	14.86 ±0.07	16.57 ±0.03
b_T ($J g mol^{-1} mg^{-1}$)	234 ±6	224 ±8	170 ±20	83 ±3	88 ±6	98 ±2
χ^2	8.98	52.3	501	374	686	210
R^2	0.989	0.945	0.625	0.916	0.854	0.964
D-R isotherm						
q_{DR} ($mg g^{-1}$)	5.4 ±0.3	0.15 ±0.04	3.7 ±0.1	0.30 ±0.04	0.80 ±0.07	0.19 ±0.02
$K_{DR} \times 10^6$ ($mol^2 J^{-2}$)	68 ±3	71.7 ±0.8	85.9 ±0.5	161 ±5	166 ±7	173 ±2
E ($J mol^{-1}$)	970 ±40	580 ±20	120 ±10	1290 ±10	790 ±20	1640 ±50
χ^2	104	84.5	58.5	90.4	1.68	127
R^2	0.877	0.911	0.956	0.980	0.949	0.978

5.7.2.3. Thermodynamic analysis of MLT and CHP adsorption onto SCG material 900PC

To get insight into the thermodynamics of the process, Van't Hoff plots were constructed and analyzed (Figure 44). The obtained thermodynamic parameters, presented in Table 31, provide insights into the adsorption behavior of MLT and CHP onto 900PC.

The adsorptions of both OPs onto 900PC are characterized as an endothermic process, accompanied by a large positive change in entropy. This suggests that OP adsorptions on 900PC are driven by entropy, which compensates for the enthalpy increase, resulting in a negative ΔG^0 that increases with temperature. These findings imply spontaneous adsorption, consistent with experimental observations.

Even though MLT and CHP are structurally very different, their adsorption onto 900PC is shown to be very similar, indicating that 900PC does not have preferences over any group (aliphatic or aromatic).

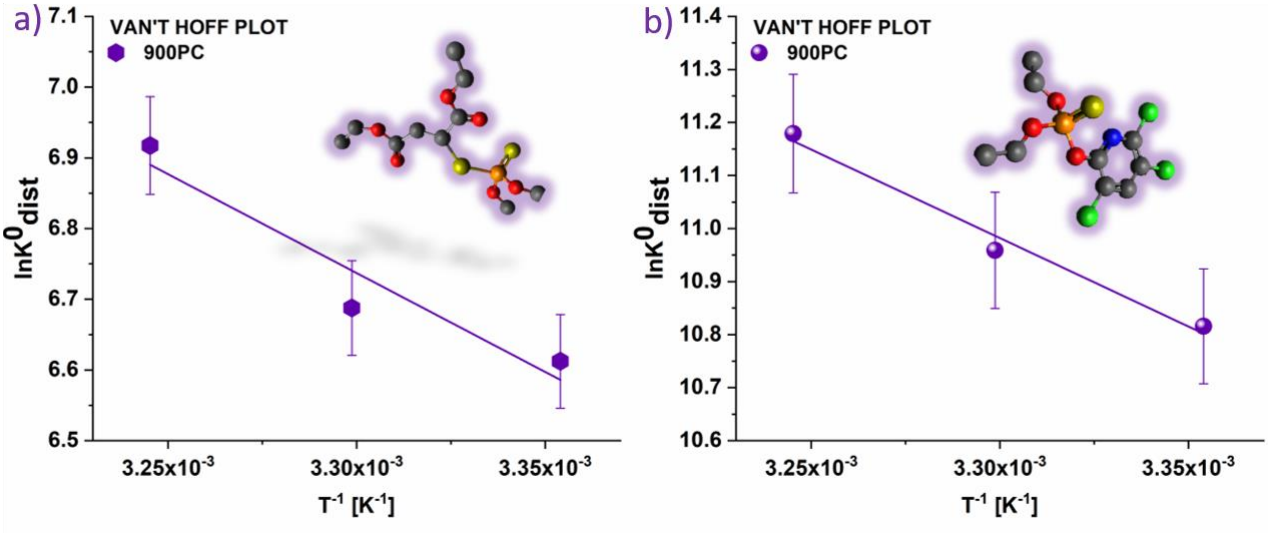

Figure 44. Van't Hoff plots for a) MLT, b) CHP adsorption onto 900PC

Table 31. Thermodynamic parameters for MLT and CHP adsorption onto 900PC (1 mg mL^{-1})

	ΔH^0 [kJ mol^{-1}]	ΔS^0 [J $mol^{-1}K^{-1}$]	ΔG^0 [kJ mol^{-1}]			R^2
T [°C] →			25	30	35	
MLT	23 ±3	130 ±20	−16.3 ±0.9	−17.0 ±0.9	−17.7 ±0.9	0.833
CHP	27.7 ±0.4	182 ±3	−26.8 ±0.4	−27.7 ±0.4	−28.6 ±0.4	0.966

5.7.2.4. Influence of varying SCG materials' 900PC concentration on adsorption of MLT and CHP

To further explore the adsorption behavior of MLT and CHP, experiments were conducted at 25°C using material concentrations of 0.5 mg mL^{-1} and 0.1 mg mL^{-1}. The experimental data were analyzed using non-linear Freundlich, Langmuir, Temkin, and Dubinin-Radushkevich isotherm models. The Graphical representations are given in Figure 45, while the obtained parameters are summarized in Table 32.

For both MLT and CHP, variations in material concentration induced significant shifts in adsorption parameters. Decreased values of parameters such as n, K_T, b_T, and E with lower material concentrations indicated weaker interactions between 900PC and the pesticides, reflecting reduced affinity, as expected. Conversely, the reduction in material concentration to 0.5 mg mL^{-1} led to substantial increases in q_{max} values for both contaminants, indicating higher maximum adsorption capacities at lower material concentrations due to the shift in the equilibrium. On the other hand, the further reduction in materials concertation influenced the decrease of q_{max}. Specifically, at lower material concentrations, there were notable changes in q_{max} values for both OPs adsorption. When the material concentration was reduced to 0.5 mg mL^{-1}, q_{max} values for their adsorption showed the highest values (92.0±0.2 for MLT and 259±2 for CHP).

These findings imply the sensitivity of adsorption parameters to changes in material concentration and their impact on the adsorption process. While the fundamental nature of the adsorption process remained unchanged, alterations in various adsorption parameters reflected adjustments in the interactions between 900PC and the OPs, emphasizing the importance of considering material concentration in optimizing adsorption processes.

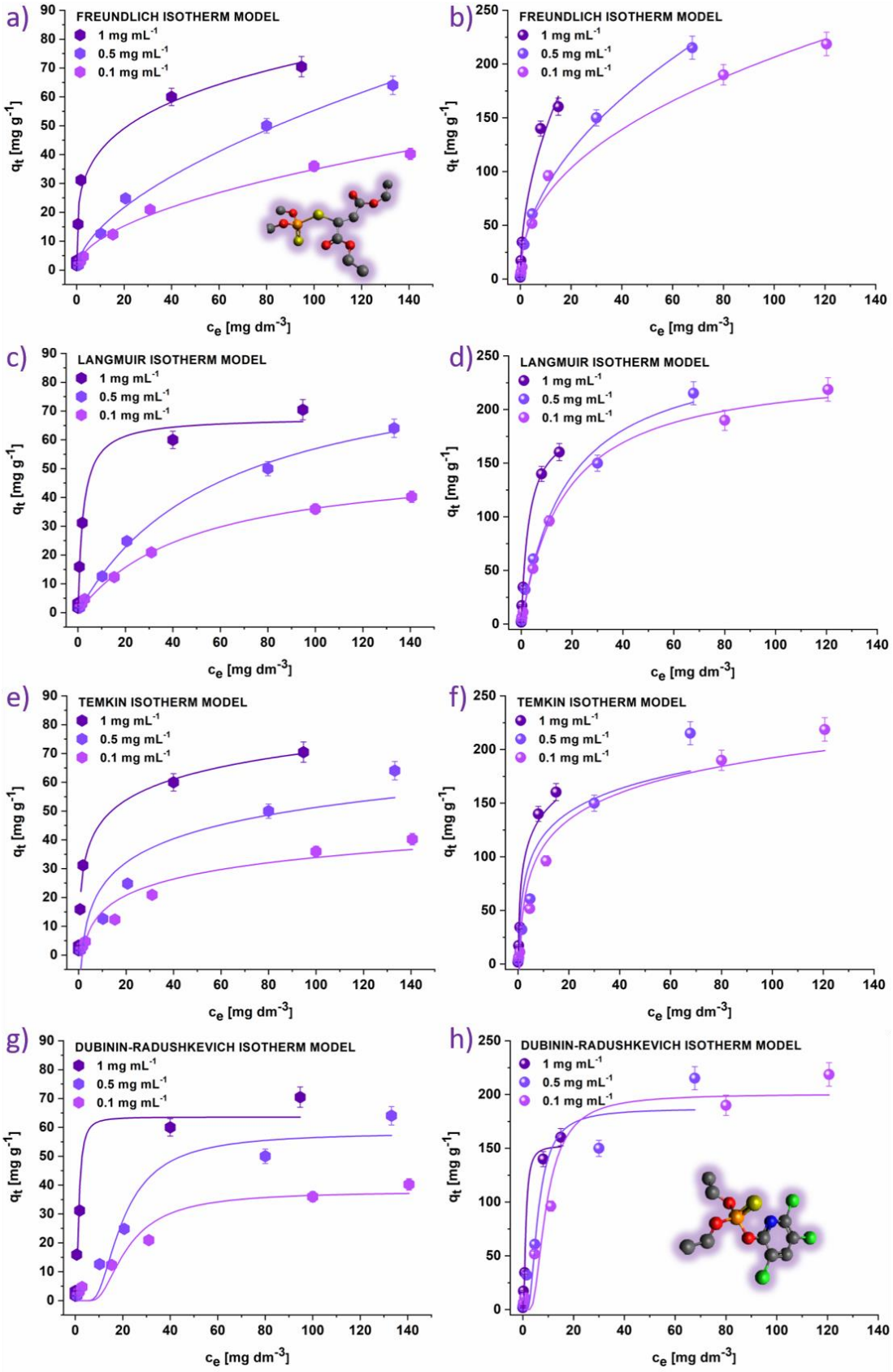

Figure 45. Graphical representations of isotherm models fitting the experimental data of MLT (left) and CHP (right) adsorption onto 900PC (1, 0.5, and 0.1 mg mL^{-1})

Table 32. Isotherm adsorption parameters of MLT and CHP adsorption onto 900PC (1 mg mL^{-1}, 0.5 mg mL^{-1}, and 0.1 mg mL^{-1}) at 25°C

	MLT			CHP		
C_{mat} (mg mL^{-1})	**1**	**0.5**	**0.1**	**1**	**0.5**	**0.1**
Freundlich isotherm						
K_F ($(dm^3\ mg^{-1})^{1/n}$)	23.0 ±0.3	3.68 ±0.02	3.26 ±0.02	37.9 ±0.1	25.9 ±0.1	28.3 ±0.2
n	4.05 ±0.05	1.71 ±0.03	1.96 ±0.03	1.88 ±0.02	1.90 ±0.02	2.33 ±0.04
χ^2	25.5	6.23	2.33	13.14	28.08	194
R^2	0.970	0.990	0.990	0.997	0.996	0.974
Langmuir isotherm						
$K_L \times 10^2$ ($dm^3\ mg^{-1}$)	42.8 ±0.3	1.72 ±0.01	2.22 ±0.03	32.7 ±0.1	7.11 ±0.02	5.721 ±0.001
q_{max} (mg g^{-1})	72.1 ±0.6	92.0 ±0.2	54.0 ±0.6	193 ±1	259 ±2	250 ±1
χ^2	6.01	0.835	1.73	3.61	25.97	2.21
R^2	0.993	0.999	0.993	0.999	0.997	1.000
Temkin isotherm						
K_T ($dm^3\ mg^{-1}$)	8.48 ±0.05	0.75 ±0.08	0.65 ±0.08	9.8 ±0.1	4.4 ±0.5	2.16 ±0.08
b_T (J g mol^{-1} mg^{-1})	234 ±6	251 ±9	316 ±7	83 ±3	77 ±7	70 ±5
χ^2	8.98	114	25.4	374	1334	374
R^2	0.989	0.826	0.890	0.916	0.827	0.916
D-R isotherm						
q_{DR} (mg g^{-1})	5.4 ±0.3	64.01 ±0.07	38.2 ±0.1	0.30 ±0.04	216 ±4	213 ±8
$K_{DR} \times 10^6$ ($mol^2\ J^{-2}$)	68 ±3	58 ±1	61 ±3	161 ±5	5.53 ±0.05	1.4 ±0.4
E (J mol^{-1})	970 ±40	92 ±5	90 ±10	1290 ±10	300 ±10	190 ±20
χ^2	104	41.8	26.6	90.4	361	792
R^2	0.877	0.936	0.885	0.980	0.953	0.896

5.7.2.5. Adsorption of MLT and CHP onto SCG material 900PC under dynamic conditions. Regeneration and reuse of the adsorbent

The obtained results are shown in Figure 46. By observing the presented results, it can be concluded that the material can successfully remediate 98% of MLT and 97% of CHP under dynamic conditions, and it can be regenerated using 5 mL of 25% ethanol solution and reused for at least 10 cycles without significant impact on the adsorption capacity, as it loses around 10% of its efficiency after 10th cycles.

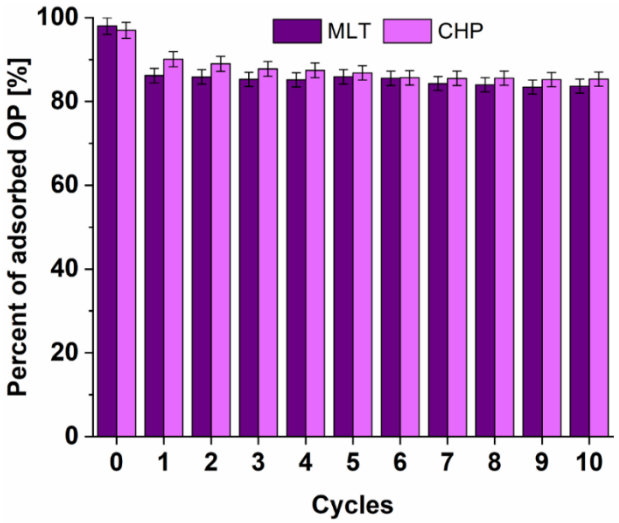

Figure 46. Histogram representing the percent of adsorbed OP through 10 cycles of regeneration and reuse

5.7.2.6. Assessment of AChE activity inhibition after MLT and CHP remediation using 900PC

The neurotoxicological assessment was performed as described in Section 4.2.2.4, and the histogram showing the difference in the activity of AChE before and after the adsorption of MLT and CHP is shown in Figure 47. It can be seen that the AChE inhibition due to the contact with samples was highly reduced after the adsorption in all cases, indicating that no more toxic products, such as OPs' oxo-forms, were formed during this process.

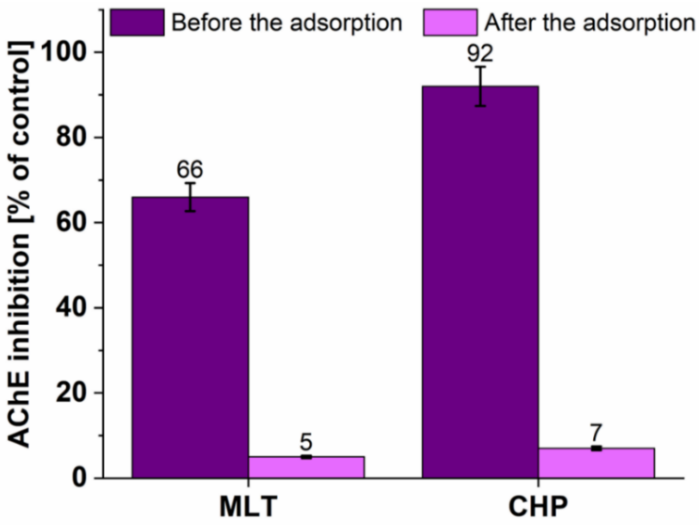

Figure 47. Histogram of AChE activity inhibition before and after the adsorption of MLT and CHP using 900PC

5.7.3. Adsorption of MLT and CHP from the mixture onto SCG material 900PC

In order to test the specificity of the material, the mixture containing 1 mg mL^{-1} adsorbent and 5×10^{-5} mol dm^{-3} of both OPs was made. The mixture was incubated for 60 min and analyzed using UPLC. The obtained results can be seen in Figure 48.

The results show that 900PC prefers CHP over MLT, as was expected by comparing previously obtained q_{max} values from the Langumir isotherm model. As the material adsorbed a similar amount of OPs in the mixture as in the one-contaminant experiments, it can be assumed that these pesticides are adsorbed onto different adsorption places. Moreover, it can be concluded that matrix complexification with the presence of the other pesticide does not impact the efficiency of the material and that there are no hindrances between them. Even though the material shows a preference towards CHP, it cannot be considered specific, as it adsorbs both components very well.

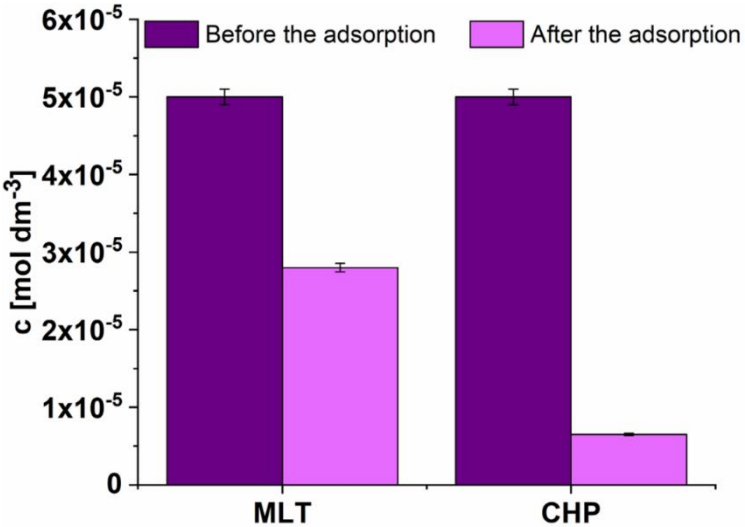

Figure 48. Histogram representing the concentration of OPs in the mixture before and after remediation using 900PC

5.7.4. Discussion on MLT and CHP adsorption onto SCG material 900PC

The SEM micrography and EDX analysis of 900PC confirm a granular, heterogeneous, and highly porous structure. This morphology is advantageous for adsorption processes, providing abundant surface area and pore volume, which are critical for effective contaminant uptake. The high percentage of C, O, and P suggests a dominant carbon structure with phosphorus-containing functional groups. The presence of minor elements such as N, K, Ca, Mg, Na, and Si further characterizes the material's complex chemical composition derived from the precursor. XRD analysis indicates a crystalline structure with characteristic reflections of graphitic carbon, affirming the material's high degree of graphitization. This graphitic nature is beneficial for adsorption through π-π interactions, especially with aromatic pollutants like CHP. FTIR and Boehm titration analyses highlight the presence of functional groups such as aromatic rings, hydroxyl, and P=O bonds. These groups enhance the material's hydrophilicity and surface reactivity, contributing to its adsorption capacity. The zeta potential measurements indicate a slightly negatively charged surface, favoring the adsorption of positively charged or polar molecules under the experimental conditions.

The adsorption kinetics of MLT and CHP onto 900PC reveal rapid adsorption, achieving equilibrium within 10 minutes for MLT and 30 minutes for CHP. The data fit well with both PFO and PSO kinetic models, indicating that the adsorption mechanism is likely chemisorption involving valence forces through the sharing or exchange of electrons between adsorbent and adsorbate. The IPD model further supports a multi-stage adsorption process, with initial external diffusion followed by intraparticle diffusion and, finally, equilibrium.

The adsorption isotherms for MLT and CHP fit both Freundlich and Langmuir models, suggesting a complex adsorption process involving both monolayer and multilayer adsorption on a heterogeneous surface. The Langmuir model's fit indicates initial monolayer adsorption at specific sites, while the Freundlich model accounts for the material's diverse adsorption sites and multilayer adsorption behavior. The Langmuir maximum adsorption capacities for MLT and CHP increase with temperature, highlighting the endothermic nature of the adsorption process. The increasing q_{max} values suggest that higher temperatures enhance the material's adsorption efficiency, possibly due to increased diffusion rates and interaction energies at elevated temperatures. Thermodynamic analysis via Van't Hoff plots confirms that the adsorption of MLT and CHP onto 900PC is spontaneous, as evidenced by negative ΔG^0. The assumed endothermic nature of the process is supported by positive ΔH^0 values, while the positive entropy ΔS^0 changes suggest increased randomness at the solid-liquid interface during adsorption.

Experiments at different material concentrations demonstrate that adsorption parameters are sensitive to changes in adsorbent concentration. Lower material concentrations increase the q_{max} values, reflecting a higher efficiency at these conditions due to equilibrium shifts. This sensitivity highlights the importance of optimizing material concentration for practical applications. The dynamic adsorption experiments show that 900PC can effectively remediate 98% of MLT and 97% of CHP, and the material can be regenerated using a 25% ethanol solution. It retains high adsorption efficiency over at least 10 cycles, losing only about 10% of its capacity, indicating good reusability. Neurotoxicological assessment indicates that contact with the material significantly lowers the toxicity of MLT and CHP, suggesting that no toxic by-products are formed during the adsorption process. This finding implies the material's potential for safe environmental applications in pesticide remediation.

Overall, the 900PC material demonstrates excellent adsorption characteristics for both MLT and CHP, driven by its highly porous structure, suitable surface functional groups, and favorable adsorption kinetics and thermodynamics.

5.8. Comparative analysis of materials obtained by thermochemical conversion of SCG for MLT and CHP removal

5.8.1. The impact of thermochemical conversion on physicochemical properties of SCG materials

The SEM analysis indicated uniformity across materials that were first carbonized and then activated, reflecting the morphology of the precursor materials. The materials that underwent primary chemical activation (K and K400) show distinct changes in the micrographs, indicating the chemical interaction between the SCG and KOH.

As the carbonization temperature increases to 650°C, there is a noticeable increase in the carbon content while the oxygen content decreases. After reaching this temperature, the carbon percentage stabilizes at approximately 80 atomic percent. Oxygen content increases with chemical activation, suggesting that this type of activation primarily promotes the formation of oxygen-containing functional groups on the surface of the material. In contrast, physical activation does not alter the elemental profile of the materials.

This observation is further supported by the reduction in the number of vibrational bands in the FTIR spectra of the materials thermochemically treated up to 650°C, after which the FTIR spectra of the materials remain unchanged. Physical activation has no significant effect on the appearance of the spectra. Chemical activation with H_3PO_4 introduces minimal changes, whereas chemical activation with KOH results in new vibrational bands in the spectra, indicating ongoing chemical interactions, even post-carbonization.

Zeta potential measurements have shown that the thermochemical conversion of materials also affects the stability of the materials in suspension, with most SCG materials being more stable at a pH greater than 10. No correlation was observed between the isoelectric points and the method of activation.

BET analysis demonstrated that the specific surface area and total pore volume do not linearly increase with the increase of the temperature of thermochemical conversion, as their values obtained for SCG materials 400 and SCG 650 are similar, even lower for SCG 650 materials. Increasing the temperature of the thermochemical conversion to 900°C led to the increase of S_{BET} and V_{tot} by far. Activation of the materials influenced these parameters differently, depending on the temperature. In summary, physical activation of the materials using CO_2 further increased S_{BET} and $V_{tot,}$ and chemical activation tends to reduce these properties. Physicochemical-activated materials exhibited the highest increase of these parameters, no matter the temperature.

By summarizing these results, it can be concluded that the temperature of thermochemical conversion and the activation method highly influence SCG materials, implying the importance of the investigation of synthesis parameters for obtaining activated carbon material with desired properties for specific applications.

5.8.2. Economic, environmental and practical aspects of thermochemical conversion of SCG and SCG materials' application as adsorbents for MLT and CHP

To adequately choose the most cost-effective and environmentally friendly material for synthesis and use, it is essential to evaluate both economic factors and environmental protection aspects of their production. The costs of the chemicals used will be excluded from the material cost calculation since the quantities used are minimal, making the normalized cost per amount negligible. The power of the tube furnace is 5kW.

SCG is a biowaste material, while material K represents SCG treated with KOH and is not carbonized, making their production economically free. For the synthesis of materials carbonized at 400°C, the furnace operated for 80 minutes to reach the desired temperature and maintained that temperature for an additional 60 minutes, totaling 140 minutes (2.33 hours) of operation. For materials that underwent a second carbonization after chemical activation, the furnace operated twice as long, totaling 4.66 hours. To reach a temperature of 650°C at a rate of 5°C min^{-1}, the furnace operated for 130 minutes and maintained that temperature for 60 minutes, resulting in a total carbonization time of 190 minutes (3.17 hours). Chemically activated materials were returned to the furnace, requiring the same amount of time again, totaling 6.33 hours. Carbonization at 900°C required the furnace to reach the temperature in 180 minutes and maintain it for 60 minutes, totaling 240 minutes (4 hours) of operation. Chemical activation required additional carbonization, bringing the total furnace operation time to 480 minutes (8 hours).

Given the furnace's power of 5kW, the energy consumption was calculated using the formula:

$$A = P \times t \qquad \text{Eq. 26}$$

Currently, in Serbia, the electricity price for the industry is P(1 kWh)=23.9117 RSD per kWh [96]. Thus, the cost of thermochemical conversion of SCG under conditions of interest can be calculated:

$$\text{Price(tc)} = A \times P(1\ \text{kWh}) \qquad \text{Eq. 27}$$

The carbonization vessel can hold up to 10g of SCG, allowing us to calculate the mass of the produced material:

$$m = 10\text{g} \times Y \qquad \text{Eq. 28}$$

Finally, the cost of synthesizing one gram of material is determined using the formula:

$$\text{Price}(1\ \text{g}) = \frac{\text{Price(tc)}}{m} \qquad \text{Eq. 29}$$

The data are presented in Table 33.

Table 33. Cost of SCG materials' production

	Y [%]	Operating time [h]	A [kWh]	Price (tc) [RSD]	m [g]	Price (1g) [RSD g^{-1}]
SCG	/	/	/	/	/	/
K	/	/	/	/	/	/
400	21	2.33	11.65	278.57	2.10	132.65
400K	17.6	4.66	23.3	557.14	1.76	316.56
400P	16.8	4.66	23.3	557.14	1.68	331.63
400C	19	2.33	11.65	278.57	1.90	146.62
400KC	19.1	4.66	23.3	557.14	1.91	291.70
400PC	19.3	4.66	23.3	557.14	1.93	288.67
K400	5.8	2.33	11.65	278.57	0.58	480.30
650	18	3.17	15.85	379.00	1.80	210.56
650K	15.5	6.33	31.7	758.00	1.55	489.03
650P	15.5	6.33	31.7	758.00	1.55	489.03
650C	17	3.17	15.85	379.00	1.70	222.94
650KC	14.8	6.33	31.7	758.00	1.48	512.16
650PC	15.3	6.33	31.7	758.00	1.53	495.43
900	15	4	20	478.23	1.50	318.82
900K	12.2	8	40	956.47	1.22	783.99
900P	10.5	8	40	956.47	1.05	910.92
900C	14	4	20	478.23	1.40	341.60
900KC	12.6	8	40	956.47	1.26	759.10
900PC	2.1	8	40	956.47	0.21	4554.61

The impact of synthesizing and applying these materials on the environment is highly positive. The thermochemical conversion of SCG significantly reduces the negative environmental effects of this biowaste. Furthermore, using these materials for pesticide remediation is highly beneficial, as they effectively remove harmful compounds from the environment.

While the synthesis process of some materials involves using KOH, H_3PO_4, and CO_2, which slightly diminishes the environmental benefit from biowaste valorization, this is compensated with the substantial enhancement in the materials' adsorption properties. These chemicals improve the effectiveness of the materials, ensuring that they can adsorb and remove a larger amount of pollutants.

The synthesis and application of these materials not only effectively address waste management issues but also play a crucial role in environmental remediation efforts. This dual function emphasizes their large positive impact on the environment.

In assessing the suitability of various adsorbent materials for removing MLT and CHP from aqueous solutions, several critical parameters: synthesis cost per gram (Price(1g)), specific surface area (S_{BET}), total pore volume (V_{tot}), surface charge at pH 6, adsorption equilibrium time (t_{eq}), adsorption capacity (q_{max}), and energy of adsorption (E) were evaluated (Table 34). These metrics help determine the efficiency, cost-effectiveness, and practicality of each material for environmental remediation.

SCG and K represent cost-free adsorbents, as SCG is a widely spread biowaste. SCG exhibits a quick equilibrium time for MLT (10 minutes) and a moderate adsorption capacity of 7.06 mg g^{-1}. For CHP, however, SCG takes much longer to reach equilibrium (1440 minutes) with a lower capacity (2.36

mg g^{-1}). The high adsorption energy for CHP (4850 J/mol) indicates strong interaction, but the long equilibrium time is a significant drawback. On the other hand, K shows improved performance with a notable adsorption capacity for both pesticides, particularly for CHP (22.3 mg/g). This enhancement suggests the benefits of chemical activation without carbonization. However, it is important to note that SCG and K, despite their promising performance, are biowaste. As it was previously stated, uncarbonized SCG, in large quantities, negatively impact the environment, making them less suitable for sustainable application.

The synthesis of 400 series materials varies from 132.65 to 480.30 RSD for 1g. For instance, 400 costs 132.65 RSD per gram, with an S_{BET} of 2.38 m^2 g^{-1} and V_{tot} of 3.1×10^{-3} cm^3 g^{-1}. This material shows improved adsorption capacity for MLT (10.6 mg g^{-1}) and very good efficiency for CHP (19.4 mg g^{-1}). Further activation using KOH, H_3PO_4, and CO_2 enhanced S_{BET} and V_{tot} significantly but also impacted the decrease in adsorption capacity. So, out of 400 series materials, 400 stands out as the material with the cheapest synthesis, without using harmful chemicals, and with very good adsorption capacity for MLT and CHP, but it takes a long time to achieve equilibrium.

Materials carbonized at 650°C generally show mixed results. While 650P and 650C perform moderately well for CHP, their performance for MLT is poor. The synthesis cost is higher for these materials, with 650K and 650P costing 489.03 RSD per gram, yet they do not significantly outperform the 400 series in terms of adsorption capacity.

The 900 series materials, carbonized at 900°C, exhibit the highest S_{BET} and V_{tot} values but also significantly higher cost, with 900PC costing 4554.61 RSD per gram. These materials exhibit remarkable adsorption capacities for both MLT and CHP. For example, 900PC has an extraordinary S_{BET} (846 m^2 g^{-1}) and V_{tot} (0.557 cm^3 g^{-1}), achieving rapid equilibrium (10 minutes for MLT and 30 minutes for CHP) with exceptionally high adsorption capacities (72.1 mg g^{-1} for MLT and 193 mg g^{-1} for CHP). Despite the high cost, their superior performance makes them ideal for applications requiring maximum efficiency.

Among all the tested materials, 900PC demonstrates the best performance but is also the most expensive, costing 34.3 times more to produce than the 400 material. Additionally, its production requires the use of H_3PO_4 and CO_2. For the cost of producing 1g of 900PC, 34.3g of 400 can be produced. The quantities of MLT and CHP that these amounts can remove are 72.1 mg MLT and 193 mg CHP for 900PC, compared to 363.58 mg MLT and 665.42 mg CHP for 34.3g of 400 under stationary conditions. In dynamic conditions, where contact time between contaminants and the material is minimal, as well as when a smaller amount of the material is required, 900PC justifies its higher cost, as it exhibits adsorption rates for MLT and CHP that are 9 and 24 times faster, respectively, and higher adsorption capacities compared to 400.

Table 34. Comparison of parameters for MLT and CHP adsorption onto investigated SCG materials

Material					**MLT**				**CHP**			
	Price (1g) [RSD g^{-1}]	**S_{BET} [m^2 g^{-1}]**	**V_{tot} ×10^3 [cm^3 g^{-1}]**	**Surface charge (pH=6)**	**t_{eq} [min]**	**n at 25°C**	**q_{max} at 25°C [mg g^{-1}]**	**E at 25°C [J mol^{-1}]**	**t_{eq} [min]**	**n at 25°C**	**q_{max} at 25°C [mg g^{-1}]**	**E at 25°C [J mol^{-1}]**
SCG	0	/	/	/	10	2.94	7.06	155	1440	19.2	2.36	4850
K	0	1.53	1.69	/	90	1.28	15.5	380	400	1.95	22.3	940
400	132.65	2.38	3.13	-	90	1.72	10.6	503	1440	1.60	19.4	510
400K	316.56	3.52	8.54	-	/	/	/	/	1440	1.6	6.5	344
400P	331.63	4.28	2.43	-	/	/	/	/	1440	1.36	8.03	420
400C	146.62	6.50	7.93	-	90	2.08	7.15	682	1440	2.00	14	1300
400KC	291.70	3.96	4.91	-	/	/	/	/	1440	2.07	1.42	460
400PC	288.67	5.63	6.69	-	/	/	/	/	1440	1.9	3.4	462
K400	480.30	9.38	25.4	-	90	1.73	11.2	500	1440	2.4	16.1	1120
650	210.56	0.83	1.42	-	/	/	/	/	400	1.40	4.67	450
650K	489.03	2.21	4.06	+	/	/	/	/	/	/	/	/
650P	489.03	5.47	4.94	-	/	/	/	/	400	1.24	2.98	148
650C	222.94	1.35	0.99	-	/	/	/	/	400	1.49	2.52	440
650KC	512.16	98.03	44.37	-	/	/	/	/	1440	2.1	7.14	686
650PC	495.43	0.706	0.77	-	/	/	/	/	400	1.8	4.0	365
900	318.82	249.44	112	-	60	1.99	9.64	94	60	1.66	11.0	510
900K	783.99	159.98	83	-	60	4.0	11.6	820	60	2.26	23.6	2000
900P	910.92	248.84	107	-	60	1.6	10.6	70	60	4.8	5.9	2500
900C	341.60	665.93	297	-	60	1.88	18.6	74	60	2.08	25.4	1020
900KC	759.10	141.43	74	-	60	3.29	17.3	1100	60	2.8	25.6	2160
900PC	4554.61	846.09	557	-	10	4.05	72.1	970	30	1.88	193	1290

6. CONCLUSION

Within this doctoral dissertation, the usage of SCG as a precursor for producing adsorbents through thermochemical conversion and activation processes was investigated. The research focused on examining their efficacy as adsorbents for eliminating OPs, specifically MLT and CHP, from water. Thermochemical conversion involves modifying the chemical structure of materials through heat treatment, while activation enhances their surface characteristics, such as area and porosity, thereby improving their ability to adsorb contaminants. By employing SCG, which is abundantly available, the study aimed to develop sustainable adsorbents for addressing OP pollution in water. Additionally, economic, environmental, and practical aspects of the synthesis and application of these materials were discussed.

In the first part of the research, 20 materials were successfully synthesized by thermochemical conversion of SCG at 400°C, 650°C, and 900°C, and activation using KOH, H_3PO_4, CO_2, KOH/CO_2, and H_3PO4/CO_2 and along with SCG were characterized using: SEM, EDX, FTIR, BET, Zeta potential. Additionally, SCG material 900PC, as the most promising material, was characterized using Raman, Boehm titration, and XRD to investigate graphitization, oxygen-containing functional groups, and crystallinity, respectively.

SEM micrographs revealed that all materials, except K and K400, have the same spongy-like structure with heterogeneously distributed pores, resembling the SCG morphology. Activation with KOH prior to the thermochemical conversion led to a change in the materials' morphology, implying a chemical reaction between KOH and SCG. Analysis of the chemical composition of the materials revealed an increase of at.% of C with thermochemical conversion at up to 650°C, after which it remains at around 80 at.%. Chemical activation induced the increase in at.% of O, implying that these activations mostly affect the increase of oxygen functional groups, while physical activation did not affect the chemical composition of the materials, as expected. The conclusions drawn from EDX are supported with FTIR spectra analysis, as with the increase of the temperature of thermochemical conversion up to 650°C, changes can be seen in FTIR spectra, and the further increase of temperature does not affect functional groups. As previously stated after EDX analysis, chemical activation led to an increase of the oxygen-containing functional groups, while physical activation did not affect any vibrations in the material. S_{BET} and V_{tot} did not show any dependence on the temperature of thermochemical conversion or activation. Series of SCG materials 900 showed the highest values of these parameters, implying that temperature has a great impact on specific surface area and porosity. On the other hand, SCG materials 650 have lower values of these parameters compared to SCG materials 400, implying that the porosity of the material does not only depend on the temperature of thermochemical conversion but also on the processes happening during the thermochemical conversion. At a temperature of 650°C, the pores are clogged, possibly due to the products of chemical degradation SCG. Chemical activation of SCG 400 and SCG 650 materials increased these parameters, while for SCG 900 materials, it led to their decrease. Physical activation induced the increase of S_{BET} and V_{tot} by widening existing pores and creating new ones. Zeta potential measurements revealed that all materials, except 650K, have negatively charged surfaces at the desired pH=6.

Before the start of the adsorption experiments, a screening test was performed, and only the materials that exhibited a higher percent of OP adsorption compared to raw material were further investigated.

The adsorption characteristics of MLT and CHP onto SCG reveal distinct behaviors reflecting their molecular structures' impact on the adsorption process. MLT, being aliphatic, reaches adsorption

equilibrium much faster than the aromatic CHP, suggesting that the nature of the molecule significantly influences the adsorption kinetics. The kinetic models, particularly the PFO model, aligned well with experimental data for both OPs, indicating a surface adsorption mechanism influenced predominantly by adsorbate concentration. The thermodynamic analysis showed contrasting behaviors: MLT adsorption was exothermic with slight negative entropy change, driven by enthalpic interactions, while CHP adsorption was endothermic with significant positive entropy change, driven by entropy. These findings highlight the importance of molecular structure in determining adsorption behavior and kinetics.

The activation of SCG using KOH significantly impacts its adsorption properties and mechanisms. SEM analysis of SCG material K demonstrated a transformation in structure, providing a diverse array of adsorption sites. EDX and FTIR analyses indicated the introduction of functional groups and the preservation of certain structural features of cellulose, contributing to the material's mechanical properties and interaction with adsorbates. Kinetic studies showed that MLT and CHP reached equilibrium at different times, with the Elovich model providing a good fit, especially for CHP, indicating a high initial adsorption rate and low desorption rates. The Langmuir isotherm model suggested monolayer adsorption on homogeneous sites, with CHP showing higher adsorption capacities than MLT, influenced by temperature-dependent behaviors.

Kinetic and isotherm studies indicated that materials activated at higher temperatures, particularly with KOH, exhibited significantly improved adsorption capacities and kinetics. The thermodynamic analysis confirmed the spontaneous nature of the adsorption processes, with varying enthalpic and entropic contributions. These results emphasize the critical role of activation processes and temperature in optimizing SCG-based adsorbents for effective pesticide removal.

The impact of SCG activation on adsorption is further evidenced by the comparison of various materials synthesized at different conditions. The specific surface area, pore volume, and surface charge were key factors influencing adsorption performance. Materials like 900PC demonstrated excellent adsorption characteristics, driven by a highly porous structure and suitable surface functional groups. Dynamic adsorption experiments showed high removal efficiencies and good reusability, indicating the material's potential for practical applications. The presence of functional groups and the material's zeta potential were crucial in enhancing adsorption efficiency, particularly for CHP through π-π interactions.

SCG material 900PC stands out as the most effective, despite its high cost, due to its high surface area and adsorption capacity. On the other hand, 400 stands out as a low-cost, green synthesized material with good adsorption capacity but slow. Experimental conditions, the economic and environmental implications, and the adsorption efficiency must be carefully considered for the adequate choice of the material.

Overall, the thermochemical conversion of SCG and subsequent activation processes have significant environmental benefits, reducing biowaste and enhancing pesticide remediation. The synthesis of SCG-based adsorbents involves careful consideration of activation methods to balance surface area, pore volume, and functional group introduction. The favorable adsorption kinetics and capacities, alongside the materials' reusability, highlight their suitability for environmental applications. The comprehensive analysis of adsorption mechanisms, kinetics, and thermodynamics underscores the importance of optimizing synthesis parameters to develop effective adsorbents for organic pollutant removal, contributing positively to environmental sustainability.

Considering all processes investigated in this doctoral dissertation, it can be concluded that this contribution supports and advances the UN’s sustainable development goals, in particular SDG 6 (Clean Water and Sanitation) by remediation of OPs, SDG 12 (Responsible consumption and production) and SDG 13 (Climate action) by using climate-harmful biowaste (SCG) in production of carbon materials.

7. REFERENCES

[1] P. Sharma, V.K. Gaur, S. Gupta, S. Varjani, A. Pandey, E. Gnansounou, S. You, H.H. Ngo, J.W.C. Wong, Trends in mitigation of industrial waste: Global health hazards, environmental implications and waste derived economy for environmental sustainability, Science of The Total Environment, 811 (2022) 152357, DOI: https://doi.org/10.1016/j.scitotenv.2021.152357.

[2] R. Santagata, M. Ripa, A. Genovese, S. Ulgiati, Food waste recovery pathways: Challenges and opportunities for an emerging bio-based circular economy. A systematic review and an assessment, Journal of Cleaner Production, 286 (2021) 125490, DOI: https://doi.org/10.1016/j.jclepro.2020.125490.

[3] I. Ahmed, M.A. Zia, H. Afzal, S. Ahmed, M. Ahmad, Z. Akram, F. Sher, H.M.N. Iqbal, Socio-Economic and Environmental Impacts of Biomass Valorisation: A Strategic Drive for Sustainable Bioeconomy, Sustainability, 13 (2021) 4200, DOI: https://doi.org/10.3390/su13084200.

[4] S. Sharma, S. Kumar, V. Kumar, R. Sharma, Pesticides and vegetables: ecological and metabolic fate with their field and food significance, International Journal of Environmental Science and Technology, 20 (2023) 2267-2292, DOI: 10.1007/s13762-021-03716-1.

[5] P. Kumar, A. Raj, V.A. Kumar, Approach to Reduce Agricultural Waste via Sustainable Agricultural Practices, in: A.L. Srivastav, A.K. Bhardwaj, M. Kumar (Eds.) Valorization of Biomass Wastes for Environmental Sustainability: Green Practices for the Rural Circular Economy, Springer Nature Switzerland, Cham, 2024, pp. 21-50, DOI: 10.1007/978-3-031-52485-1_2.

[6] E. Bevilacqua, V. Cruzat, I. Singh, R.B. Rose'Meyer, S.K. Panchal, L. Brown, The Potential of Spent Coffee Grounds in Functional Food Development, Nutrients, 15 (2023) 994, DOI.

[7] M. Stylianou, A. Agapiou, M. Omirou, I. Vyrides, I.M. Ioannides, G. Maratheftis, D. Fasoula, Converting environmental risks to benefits by using spent coffee grounds (SCG) as a valuable resource, Environmental Science and Pollution Research, 25 (2018) 35776-35790, DOI: 10.1007/s11356-018-2359-6.

[8] S. Ramola, T. Belwal, R.K. Srivastava, Thermochemical Conversion of Biomass Waste-Based Biochar for Environment Remediation, in: O.V. Kharissova, L.M.T. Martínez, B.I. Kharisov (Eds.) Handbook of Nanomaterials and Nanocomposites for Energy and Environmental Applications, Springer International Publishing, Cham, 2020, pp. 1-16, DOI: 10.1007/978-3-030-11155-7_122-2.

[9] P.T. Williams, A.R. Reed, Development of activated carbon pore structure via physical and chemical activation of biomass fibre waste, Biomass and Bioenergy, 30 (2006) 144-152, DOI: https://doi.org/10.1016/j.biombioe.2005.11.006.

[10] M.B. Colovic, D.Z. Krstic, T.D. Lazarevic-Pasti, A.M. Bondzic, V.M. Vasic, Acetylcholinesterase inhibitors: pharmacology and toxicology, Current neuropharmacology, 11 (2013) 315-335, DOI.

[11] N. Tarannum, R. Khan, Cost-Effective Green Materials for the Removal of Pesticides from Aqueous Medium, in: M. Naushad, E. Lichtfouse (Eds.) Green Materials for Wastewater Treatment, Springer International Publishing, Cham, 2020, pp. 99-130, DOI: 10.1007/978-3-030-17724-9_5.

[12] Z. Chen, W. Wei, H. Chen, B.-J. Ni, Recent advances in waste-derived functional materials for wastewater remediation, Eco-Environment & Health, 1 (2022) 86-104, DOI: https://doi.org/10.1016/j.eehl.2022.05.001.

[13] https://sdgresources.relx.com/ accessed on 6/4/2024

[14] S. Babu, S. Singh Rathore, R. Singh, S. Kumar, V.K. Singh, S.K. Yadav, V. Yadav, R. Raj, D. Yadav, K. Shekhawat, O. Ali Wani, Exploring agricultural waste biomass for energy, food and feed production and pollution mitigation: A review, Bioresource Technology, 360 (2022) 127566, DOI: https://doi.org/10.1016/j.biortech.2022.127566.

[15] M.T. Kowalewska, A. Kołłajtis-Dołowy, Food, nutrient, and energy waste among school students, British Food Journal, 120 (2018) 1807-1831, DOI: 10.1108/BFJ-11-2017-0611.

[16] T. Gomiero, 2 - Soil and crop management to save food and enhance food security, in: C.M. Galanakis (Ed.) Saving Food, Academic Press, 2019, pp. 33-87, DOI: https://doi.org/10.1016/B978-0-12-815357-4.00002-X.
[17] H.M. Mahmudul, D. Akbar, M.G. Rasul, R. Narayanan, M. Mofijur, Estimation of the sustainable production of gaseous biofuels, generation of electricity, and reduction of greenhouse gas emissions using food waste in anaerobic digesters, Fuel, 310 (2022) 122346, DOI: https://doi.org/10.1016/j.fuel.2021.122346.
[18] T.M.W. Mak, X. Xiong, D.C.W. Tsang, I.K.M. Yu, C.S. Poon, Sustainable food waste management towards circular bioeconomy: Policy review, limitations and opportunities, Bioresource Technology, 297 (2020) 122497, DOI: https://doi.org/10.1016/j.biortech.2019.122497.
[19] L. Adami, M. Schiavon, From Circular Economy to Circular Ecology: A Review on the Solution of Environmental Problems through Circular Waste Management Approaches, in: Sustainability, 2021.
[20] Y.A. Hajam, R. Kumar, A. Kumar, Environmental waste management strategies and vermi transformation for sustainable development, Environmental Challenges, 13 (2023) 100747, DOI: https://doi.org/10.1016/j.envc.2023.100747.
[21] M. Kamil, K.M. Ramadan, O.I. Awad, T.K. Ibrahim, A. Inayat, X. Ma, Environmental impacts of biodiesel production from waste spent coffee grounds and its implementation in a compression ignition engine, Science of The Total Environment, 675 (2019) 13-30, DOI: https://doi.org/10.1016/j.scitotenv.2019.04.156.
[22] T.S. Andrade, J. Vakros, D. Mantzavinos, P. Lianos, Biochar obtained by carbonization of spent coffee grounds and its application in the construction of an energy storage device, Chemical Engineering Journal Advances, 4 (2020) 100061, DOI: https://doi.org/10.1016/j.ceja.2020.100061.
[23] A. Mukherjee, V.B. Borugadda, J.J. Dynes, C. Niu, A.K. Dalai, Carbon dioxide capture from flue gas in biochar produced from spent coffee grounds: Effect of surface chemistry and porous structure, Journal of Environmental Chemical Engineering, 9 (2021) 106049, DOI: https://doi.org/10.1016/j.jece.2021.106049.
[24] G. Dattatraya Saratale, R. Bhosale, S. Shobana, J.R. Banu, A. Pugazhendhi, E. Mahmoud, R. Sirohi, S. Kant Bhatia, A.E. Atabani, V. Mulone, J.-J. Yoon, H. Seung Shin, G. Kumar, A review on valorization of spent coffee grounds (SCG) towards biopolymers and biocatalysts production, Bioresource Technology, 314 (2020) 123800, DOI: https://doi.org/10.1016/j.biortech.2020.123800.
[25] H. Ahmed, R.S. Abolore, S. Jaiswal, A.K. Jaiswal, Toward Circular Economy: Potentials of Spent Coffee Grounds in Bioproducts and Chemical Production, Biomass, 4 (2024) 286-312, DOI.
[26] L. Nazari, C. Xu, M.B. Ray, Advanced Technologies (Biological and Thermochemical) for Waste-to-Energy Conversion, in: L. Nazari, C. Xu, M.B. Ray (Eds.) Advanced and Emerging Technologies for Resource Recovery from Wastes, Springer Singapore, Singapore, 2021, pp. 55-95, DOI: 10.1007/978-981-15-9267-6_3.
[27] K. Tekin, S. Karagöz, S. Bektaş, A review of hydrothermal biomass processing, Renewable and Sustainable Energy Reviews, 40 (2014) 673-687, DOI: https://doi.org/10.1016/j.rser.2014.07.216.
[28] A.A.A. Abuelnuor, M.A. Wahid, S.E. Hosseini, A. Saat, K.M. Saqr, H.H. Sait, M. Osman, Characteristics of biomass in flameless combustion: A review, Renewable and Sustainable Energy Reviews, 33 (2014) 363-370, DOI: https://doi.org/10.1016/j.rser.2014.01.079.
[29] T.Y.A. Fahmy, Y. Fahmy, F. Mobarak, M. El-Sakhawy, R.E. Abou-Zeid, Biomass pyrolysis: past, present, and future, Environment, Development and Sustainability, 22 (2020) 17-32, DOI: 10.1007/s10668-018-0200-5.
[30] P. Piersa, H. Unyay, S. Szufa, W. Lewandowska, R. Modrzewski, R. Ślężak, S. Ledakowicz, An Extensive Review and Comparison of Modern Biomass Torrefaction Reactors vs. Biomass Pyrolysis—Part 1, Energies, 15 (2022) 2227, DOI.

[31] K. Chaturvedi, A. Singhwane, M. Dhangar, M. Mili, N. Gorhae, A. Naik, N. Prashant, A.K. Srivastava, S. Verma, Bamboo for producing charcoal and biochar for versatile applications, Biomass Conversion and Biorefinery, (2023), DOI: 10.1007/s13399-022-03715-3.
[32] F. Ronsse, R.W. Nachenius, W. Prins, Chapter 11 - Carbonization of Biomass, in: A. Pandey, T. Bhaskar, M. Stöcker, R.K. Sukumaran (Eds.) Recent Advances in Thermo-Chemical Conversion of Biomass, Elsevier, Boston, 2015, pp. 293-324, DOI: https://doi.org/10.1016/B978-0-444-63289-0.00011-9.
[33] T.R. Krishna C. Doddapaneni, T. Kikas, Chapter 39 - Thermochemical and biochemical treatment strategies for resource recovery from agri-food industry wastes, in: R. Bhat (Ed.) Valorization of Agri-Food Wastes and By-Products, Academic Press, 2021, pp. 787-807, DOI: https://doi.org/10.1016/B978-0-12-824044-1.00007-6.
[34] T.A. Khan, A.S. Saud, S.S. Jamari, M.H.A. Rahim, J.-W. Park, H.-J. Kim, Hydrothermal carbonization of lignocellulosic biomass for carbon rich material preparation: A review, Biomass and Bioenergy, 130 (2019) 105384, DOI: https://doi.org/10.1016/j.biombioe.2019.105384.
[35] S. Anto, M.P. Sudhakar, T. Shan Ahamed, M.S. Samuel, T. Mathimani, K. Brindhadevi, A. Pugazhendhi, Activation strategies for biochar to use as an efficient catalyst in various applications, Fuel, 285 (2021) 119205, DOI: https://doi.org/10.1016/j.fuel.2020.119205.
[36] J. Yin, W. Zhang, N.A. Alhebshi, N. Salah, H.N. Alshareef, Synthesis Strategies of Porous Carbon for Supercapacitor Applications, Small Methods, 4 (2020) 1900853, DOI: https://doi.org/10.1002/smtd.201900853.
[37] Z. Guo, X. Han, C. Zhang, S. He, K. Liu, J. Hu, W. Yang, S. Jian, S. Jiang, G. Duan, Activation of biomass-derived porous carbon for supercapacitors: A review, Chinese Chemical Letters, 35 (2024) 109007, DOI: https://doi.org/10.1016/j.cclet.2023.109007.
[38] M. Hupian, M. Galamboš, E. Viglašová, O. Rosskopfová, V.V. Kusumkar, M. Daňo, Activated carbon treated with different chemical agents for pertechnetate adsorption, Journal of Radioanalytical and Nuclear Chemistry, 333 (2024) 1815-1829, DOI: 10.1007/s10967-024-09399-5.
[39] N.A.M. Barakat, O.M. Irfan, H.M. Moustafa, H(3)PO(4)/KOH Activation Agent for High Performance Rice Husk Activated Carbon Electrode in Acidic Media Supercapacitors, Molecules (Basel, Switzerland), 28 (2022), DOI: 10.3390/molecules28010296.
[40] A. Elmouwahidi, E. Bailón-García, A.F. Pérez-Cadenas, F.J. Maldonado-Hódar, F. Carrasco-Marín, Activated carbons from KOH and H3PO4-activation of olive residues and its application as supercapacitor electrodes, Electrochimica Acta, 229 (2017) 219-228, DOI: https://doi.org/10.1016/j.electacta.2017.01.152.
[41] S.G. Wabo, O. Klepel, Nitrogen release and pore formation through KOH activation of nitrogen-doped carbon materials: an evaluation of the literature, Carbon Letters, 31 (2021) 581-592, DOI: 10.1007/s42823-021-00252-3.
[42] Y. Gao, Q. Yue, B. Gao, A. Li, Insight into activated carbon from different kinds of chemical activating agents: A review, Science of The Total Environment, 746 (2020) 141094, DOI: https://doi.org/10.1016/j.scitotenv.2020.141094.
[43] I. Neme, G. Gonfa, C. Masi, Activated carbon from biomass precursors using phosphoric acid: A review, Heliyon, 8 (2022) e11940, DOI: https://doi.org/10.1016/j.heliyon.2022.e11940.
[44] N. Soltani, A. Bahrami, M.I. Pech-Canul, L.A. González, Review on the physicochemical treatments of rice husk for production of advanced materials, Chemical Engineering Journal, 264 (2015) 899-935, DOI: https://doi.org/10.1016/j.cej.2014.11.056.
[45] I.C. Yadav, N.L. Devi, Pesticides classification and its impact on human and environment, Environmental science and engineering, 6 (2017) 140-158, DOI.

[46] M.B. Colović, D.Z. Krstić, T.D. Lazarević-Pašti, A.M. Bondžić, V.M. Vasić, Acetylcholinesterase inhibitors: pharmacology and toxicology, Current neuropharmacology, 11 (2013) 315-335, DOI: 10.2174/1570159x11311030006.
[47] C. Pope, S. Karanth, J. Liu, Pharmacology and toxicology of cholinesterase inhibitors: uses and misuses of a common mechanism of action, Environmental Toxicology and Pharmacology, 19 (2005) 433-446, DOI: https://doi.org/10.1016/j.etap.2004.12.048.
[48] N. Bravo, M. Garí, J.O. Grimalt, Occupational and residential exposures to organophosphate and pyrethroid pesticides in a rural setting, Environmental Research, 214 (2022) 114186, DOI: https://doi.org/10.1016/j.envres.2022.114186.
[49] M. Stoytcheva, R. Zlatev, Organophosphorus pesticides analysis, Pesticides in the Modern World-Trends in Pesticides Analysis, In Tech, Croatia, (2011) 143-164, DOI.
[50] https://pubchem.ncbi.nlm.nih.gov/compound/Malathion
[51] S. Kalender, F.G. Uzun, D. Durak, F. Demir, Y. Kalender, Malathion-induced hepatotoxicity in rats: The effects of vitamins C and E, Food and Chemical Toxicology, 48 (2010) 633-638, DOI: https://doi.org/10.1016/j.fct.2009.11.044.
[52] D. Krstic, M. Colovic, K. Krinulovic, D. Djuric, V. Vasic, Inhibition of AChE by single and simultaneous exposure to malathion and its degradation products, General physiology and biophysics, 26 (2007) 247, DOI.
[53] P.D. Moore, C.G. Yedjou, P.B. Tchounwou, Malathion-induced oxidative stress, cytotoxicity, and genotoxicity in human liver carcinoma (HepG2) cells, Environmental toxicology, 25 (2010) 221-226, DOI: 10.1002/tox.20492.
[54] A. Mokarizadeh, M.R. Faryabi, M.A. Rezvanfar, M. Abdollahi, A comprehensive review of pesticides and the immune dysregulation: mechanisms, evidence and consequences, Toxicology mechanisms and methods, 25 (2015) 258-278, DOI.
[55] https://pubchem.ncbi.nlm.nih.gov/compound/Chlorpyrifos
[56] S.M. Dyer, M. Cattani, D.L. Pisaniello, F.M. Williams, J.W. Edwards, Peripheral cholinesterase inhibition by occupational chlorpyrifos exposure in Australian termiticide applicators, Toxicology, 169 (2001) 177-185, DOI: https://doi.org/10.1016/S0300-483X(01)00509-1.
[57] E.M. John, J.M. Shaike, Chlorpyrifos: pollution and remediation, Environmental Chemistry Letters, 13 (2015) 269-291, DOI: 10.1007/s10311-015-0513-7.
[58] D.J. Clegg, M. van Gemert, Determination of the reference dose for chlorpyrifos: proceedings of an expert panel, Journal of toxicology and environmental health. Part B, Critical reviews, 2 (1999) 211-255, DOI: 10.1080/109374099281179.
[59] A.T. Farag, A.M. El Okazy, A.F. El-Aswed, Developmental toxicity study of chlorpyrifos in rats, Reproductive Toxicology, 17 (2003) 203-208, DOI: https://doi.org/10.1016/S0890-6238(02)00121-1.
[60] S. Uniyal, R.K. Sharma, Technological advancement in electrochemical biosensor based detection of Organophosphate pesticide chlorpyrifos in the environment: A review of status and prospects, Biosensors and Bioelectronics, 116 (2018) 37-50, DOI: https://doi.org/10.1016/j.bios.2018.05.039.
[61] S. Sheikhi, R. Dehghanzadeh, H. Aslani, Advanced oxidation processes for chlorpyrifos removal from aqueous solution: a systematic review, Journal of environmental health science & engineering, 19 (2021) 1249-1262, DOI: 10.1007/s40201-021-00674-1.
[62] M. Xu, Q. Wang, Y. Hao, Removal of organic carbon from wastepaper pulp effluent by lab-scale solar photo-Fenton process, J Hazard Mater, 148 (2007) 103-109, DOI: 10.1016/j.jhazmat.2007.02.015.
[63] Z. Chishti, S. Hussain, K.R. Arshad, A. Khalid, M. Arshad, Microbial degradation of chlorpyrifos in liquid media and soil, Journal of environmental management, 114 (2013) 372-380, DOI: https://doi.org/10.1016/j.jenvman.2012.10.032.
[64] A.R. Kumari, G. Jeevan, M. Ashok, C.K. Rao, K. Vamsi, Malathion degradation by Bacillus spp. isolated from soil, IOSR J Pharm, 2 (2012) 37-42, DOI.

[65] N.A. Suciu, E. Capri, Adsorption of chlorpyrifos, penconazole and metalaxyl from aqueous solution by modified clays, Journal of Environmental Science and Health, Part B, 44 (2009) 525-532, DOI: 10.1080/03601230902997543.
[66] T. Lazarević-Pašti, V. Anićijević, M. Baljozović, D.V. Anićijević, S. Gutić, V. Vasić, N.V. Skorodumova, I.A. Pašti, The impact of the structure of graphene-based materials on the removal of organophosphorus pesticides from water, Environmental Science: Nano, 5 (2018) 1482-1494, DOI: 10.1039/C8EN00171E.
[67] M. Ponnuchamy, A. Kapoor, P. Senthil Kumar, D.-V.N. Vo, A. Balakrishnan, M. Mariam Jacob, P. Sivaraman, Sustainable adsorbents for the removal of pesticides from water: a review, Environmental Chemistry Letters, 19 (2021) 2425-2463, DOI: 10.1007/s10311-021-01183-1.
[68] A. Dąbrowski, Adsorption — from theory to practice, Advances in Colloid and Interface Science, 93 (2001) 135-224, DOI: https://doi.org/10.1016/S0001-8686(00)00082-8.
[69] Y. Artioli, Adsorption, in: S.E. Jørgensen, B.D. Fath (Eds.) Encyclopedia of Ecology, Academic Press, Oxford, 2008, pp. 60-65, DOI: https://doi.org/10.1016/B978-008045405-4.00252-4.
[70] M. Atif, H.Z. Haider, R. Bongiovanni, M. Fayyaz, T. Razzaq, S. Gul, Physisorption and chemisorption trends in surface modification of carbon black, Surfaces and Interfaces, 31 (2022) 102080, DOI: https://doi.org/10.1016/j.surfin.2022.102080.
[71] V. Krstić, Chapter 14 - Role of zeolite adsorbent in water treatment, in: B. Bhanvase, S. Sonawane, V. Pawade, A. Pandit (Eds.) Handbook of Nanomaterials for Wastewater Treatment, Elsevier, 2021, pp. 417-481, DOI: https://doi.org/10.1016/B978-0-12-821496-1.00024-6.
[72] T.A. Saleh, Chapter 3 - Kinetic models and thermodynamics of adsorption processes: classification, in: T.A. Saleh (Ed.) Interface Science and Technology, Elsevier, 2022, pp. 65-97, DOI: https://doi.org/10.1016/B978-0-12-849876-7.00003-8.
[73] M.A. Al-Ghouti, D.A. Da'ana, Guidelines for the use and interpretation of adsorption isotherm models: A review, J Hazard Mater, 393 (2020) 122383, DOI: https://doi.org/10.1016/j.jhazmat.2020.122383.
[74] J. Wang, X. Guo, Adsorption isotherm models: Classification, physical meaning, application and solving method, Chemosphere, 258 (2020) 127279, DOI: https://doi.org/10.1016/j.chemosphere.2020.127279.
[75] T. Chen, T. Da, Y. Ma, Reasonable calculation of the thermodynamic parameters from adsorption equilibrium constant, Journal of Molecular Liquids, 322 (2021) 114980, DOI: https://doi.org/10.1016/j.molliq.2020.114980.
[76] W. Zhang, H. Lin, Z. Lin, J. Yin, H. Lu, D. Liu, M. Zhao, 3 D Hierarchical Porous Carbon for Supercapacitors Prepared from Lignin through a Facile Template-Free Method, ChemSusChem, 8 (2015) 2114-2122, DOI: 10.1002/cssc.201403486.
[77] Z. Gao, Y. Zhang, N. Song, X. Li, Biomass-derived renewable carbon materials for electrochemical energy storage, Materials Research Letters, 5 (2017) 69-88, DOI: 10.1080/21663831.2016.1250834.
[78] J. Deng, M. Li, Y. Wang, Biomass-derived carbon: synthesis and applications in energy storage and conversion, Green Chemistry, 18 (2016) 4824-4854, DOI: 10.1039/C6GC01172A.
[79] C. Xu, M. Strømme, Sustainable Porous Carbon Materials Derived from Wood-Based Biopolymers for CO2 Capture, Nanomaterials, 9 (2019) 103, DOI.
[80] C.A. Takaya, K.R. Parmar, L.A. Fletcher, A.B. Ross, Biomass-Derived Carbonaceous Adsorbents for Trapping Ammonia, Agriculture, 9 (2019) 16, DOI.
[81] A. Xie, J. Dai, X. Chen, J. He, Z. Chang, Y. Yan, C. Li, Hierarchical porous carbon materials derived from a waste paper towel with ultrafast and ultrahigh performance for adsorption of tetracycline, RSC Advances, 6 (2016) 72985-72998, DOI: 10.1039/C6RA17286E.

[82] M.M. Jacob, M. Ponnuchamy, A. Kapoor, P. Sivaraman, Bagasse based biochar for the adsorptive removal of chlorpyrifos from contaminated water, Journal of Environmental Chemical Engineering, 8 (2020) 103904, DOI: https://doi.org/10.1016/j.jece.2020.103904.
[83] A. Celso Gonçalves, J. Zimmermann, D. Schwantes, C.R.T. Tarley, E. Conradi Junior, V. Henrique Dias de Oliveira, M.A. Campagnolo, G.L. Ziemer, Renewable Eco-Friendly Activated Biochar from Tobacco: Kinetic, Equilibrium and Thermodynamics Studies for Chlorpyrifos Removal, Separation Science and Technology, 57 (2022) 159-179, DOI: 10.1080/01496395.2021.1890776.
[84] P.T. Thuy, N.V. Anh, B. van der Bruggen, Evaluation of Two Low-Cost–High-Performance Adsorbent Materials in the Waste-to-Product Approach for the Removal of Pesticides from Drinking Water, CLEAN – Soil, Air, Water, 40 (2012) 246-253, DOI: https://doi.org/10.1002/clen.201100209.
[85] Đ.B. Katnić, S.J. Porobić, I. Vujčić, M.M. Kojić, T. Lazarević-Pašti, V. Milanković, M. Marinović-Cincović, D.Z. Živojinović, Irradiated fig pomace pyrochar as a promising and sustainable sterilized sorbent for water pollutant removal, Radiation Physics and Chemistry, 214 (2024) 111277, DOI: https://doi.org/10.1016/j.radphyschem.2023.111277.
[86] Đ. Katnić, S.J. Porobić, T. Lazarević-Pašti, M. Kojić, T. Tasić, M. Marinović-Cincović, D. Živojinović, Sterilized plum pomace biochar as a low-cost effective sorbent of environmental contaminants, Journal of Water Process Engineering, 56 (2023) 104487, DOI: https://doi.org/10.1016/j.jwpe.2023.104487.
[87] M.N. Ettish, G.S. El-Sayyad, M.A. Elsayed, O. Abuzalat, Preparation and characterization of new adsorbent from Cinnamon waste by physical activation for removal of Chlorpyrifos, Environmental Challenges, 5 (2021) 100208, DOI: https://doi.org/10.1016/j.envc.2021.100208.
[88] L. Veitía-de-Armas, H.E. Reynel-Ávila, A. Bonilla-Petriciolet, J. Jáuregui-Rincón, Green solvent-based lipid extraction from guava seeds and spent coffee grounds to produce biodiesel: Biomass valorization and esterification/transesterification route, Industrial Crops and Products, 214 (2024) 118535, DOI: https://doi.org/10.1016/j.indcrop.2024.118535.
[89] E. Fuente, J.A. Menéndez, M.A. Díez, D. Suárez, M.A. Montes-Morán, Infrared Spectroscopy of Carbon Materials: A Quantum Chemical Study of Model Compounds, The Journal of Physical Chemistry B, 107 (2003) 6350-6359, DOI: 10.1021/jp027482g.
[90] M. Naushad, A.A. Alqadami, Z.A. AlOthman, I.H. Alsohaimi, M.S. Algamdi, A.M. Aldawsari, Adsorption kinetics, isotherm and reusability studies for the removal of cationic dye from aqueous medium using arginine modified activated carbon, Journal of Molecular Liquids, 293 (2019) 111442, DOI: https://doi.org/10.1016/j.molliq.2019.111442.
[91] D. Pujol, C. Liu, J. Gominho, M.À. Olivella, N. Fiol, I. Villaescusa, H. Pereira, The chemical composition of exhausted coffee waste, Industrial Crops and Products, 50 (2013) 423-429, DOI: https://doi.org/10.1016/j.indcrop.2013.07.056.
[92] E.C. Silva Filho, L.S. Santos Júnior, M.M.F. Silva, M.G. Fonseca, S.A.A. Santana, C. Airoldi, Surface cellulose modification with 2-aminomethylpyridine for copper, cobalt, nickel and zinc removal from aqueous solution, Materials Research, 16 (2013) 79-84, DOI.
[93] A. Dandekar, R.T.K. Baker, M.A. Vannice, Characterization of activated carbon, graphitized carbon fibers and synthetic diamond powder using TPD and DRIFTS, Carbon, 36 (1998) 1821-1831, DOI: https://doi.org/10.1016/S0008-6223(98)00154-7.
[94] M. Biegun, A. Dymerska, X. Chen, E. Mijowska, Study of the Active Carbon from Used Coffee Grounds as the Active Material for a High-Temperature Stable Supercapacitor with Ionic-Liquid Electrolyte, in: Materials, 2020.
[95] R.R. Nair, M.M. Mondal, D. Weichgrebe, Biochar from co-pyrolysis of urban organic wastes—investigation of carbon sink potential using ATR-FTIR and TGA, Biomass Conversion and Biorefinery, 12 (2022) 4729-4743, DOI: 10.1007/s13399-020-01000-9.
[96] https://www.eps.rs/lat/snabdevanje/Stranice/cene.aspx accessed on 6/4/2024

Biography of the Author

Vedran Milanković was born on June 3, 1997, in Prijedor, Bosnia and Herzegovina, where he completed his primary and secondary education as an excellent student. He enrolled in undergraduate studies at the Faculty of Physical Chemistry, University of Belgrade, in the 2016/2017 academic year. He graduated on July 17, 2020, with an average grade of 9.22 and a grade of 10 for his thesis defense titled "Comparison of Electrochemical Sensors with Conventional and Bioanalytical Methods for Pesticide Detection" under the mentorship of Prof. Dr. Igor Pašti, a full professor at the University of Belgrade - Faculty of Physical Chemistry. The experimental parts of his thesis were conducted in the Laboratory for Physical Chemistry at the Vinča Institute of Nuclear Sciences, under the guidance of Dr. Tamara Lazarević-Pašti, a full research professor at the Vinča Institute of Nuclear Sciences. He enrolled in master's academic studies at the Faculty of Physical Chemistry, University of Belgrade, in 2020, and completed them in 2021 with an average grade of 10.00. His master's thesis titled "Carbon Materials Derived from Biomass as Adsorbents for Chlorpyrifos" was conducted under the mentorship of Prof. Dr. Igor Pašti, a full professor at the University of Belgrade - Faculty of Physical Chemistry, and Dr. Tamara Lazarević-Pašti, a full research professor at the Vinča Institute of Nuclear Sciences, and was defended on July 20, 2021, with a grade of 10. The experimental parts of his master's thesis were conducted in the Laboratory for Physical Chemistry at the Vinča Institute of Nuclear Sciences.

During his undergraduate and master's studies, he was a member of student organizations at the Faculty and University of Belgrade. From October 2018 to June 2019, he served as the Vice President for Science of the Student Parliament of the University of Belgrade. He was a member of the Senate of the University of Belgrade from June 2019 to October 2020. During his studies, he participated in science promotion projects "Researchers' Night" and "Science Around Us." He was the organizer of humanitarian actions "New Year's Gifts" and "Night of Humanity" at the Faculty of Physical Chemistry. From April 2019 to September 2021, he served as the president of the Center for Scientific Research Work of Students at the Faculty of Physical Chemistry, during which he completed a summer internship on the topic: "Analysis of the Impact of Different Heteropoly Acids on the Surface Functional Groups of Carbon Materials Using FTIR Spectroscopy" under the mentorship of Dr. Danica Bajuk Bogdanović, a full research professor at the University of Belgrade - Faculty of Physical Chemistry.

He enrolled in doctoral academic studies at the Faculty of Physical Chemistry, University of Belgrade, in the 2021/2022 academic year and passed all the exams prescribed by the curriculum with an average grade of 9.86. Since January 2022, he has been employed at the Vinča Institute of Nuclear Sciences, working on the topic "Chemical-Biological Approach to Characterizing Bioactive Compounds - Strategies for Improving Health and the Environment" until the end of 2023. From January 2024, he will be engaged in the topic "Development of Sustainable Integrated Processes for the Isolation of Various Compounds Using Innovative Solutions in Accordance with Green Chemistry Principles."

Vedran Milanković's scientific research is focused on environmental protection. Since November 1, 2021, he has been conducting research in the Laboratory for Physical Chemistry at the Vinča Institute of Nuclear Sciences as part of the experimental work in the field of water purification contaminated with pesticides, dyes, and antibiotics. In his work so far, he has been engaged in research tasks such as the synthesis and characterization of carbon materials, the examination of investigated pollutants, their toxicity, and methods for their removal from the environment through adsorption on carbon materials derived from biomass. Accordingly, his research belongs to the narrower scientific fields of Physical Chemistry - Environmental Control and Protection and Physical Chemistry - Materials.

Bibliography

1. Monographs, monographic studies, thematic collections, lexicographic, and cartographic publications of international significance (M10)

1.1. Monographic study/chapter in a book (M11) (Prominent monograph of international significance) – M13

1. **Milanković, V**., & Lazarević-Pašti, T. D. (2021). The Role of the Cholinergic System in Lung Diseases [Springer Singapore]. Targeting Cellular Signalling Pathways in Lung Diseases. https://doi.org/10.1007/978-981-33-6827-9_29

2. Articles published in international scientific journals of significance (M20)

2.1. Articles in a leading international journals of category M21a

1. Katnić, Đ. B., Porobić, S. J., Vujčić, I., Kojić, M. M., Lazarević-Pašti, T., **Milanković, V.**, Marinović-Cincović, M., & Živojinović, D. Z. (2024). Irradiated fig pomace pyrochar as a promising and sustainable sterilized sorbent for water pollutant removal [Elsevier Ltd]. Radiation Physics and Chemistry, 214, 111277–111277. https://doi.org/10.1016/j.radphyschem.2023.111277
2. **Milanković, V.**, Tasić, T., Brković, S. M., Potkonjak, N. I., Unterweger, C., Bajuk-Bogdanović, D. V., Pašti, I. A., & Lazarević-Pašti, T. (2024). Spent coffee grounds-derived carbon material as an effective adsorbent for removing multiple contaminants from wastewater: A comprehensive kinetic, isotherm, and thermodynamic study. Journal of Water Process Engineering, 63, 105507–105507. https://doi.org/10.1016/j.jwpe.2024.105507
3. Milenković, M., Lazarević-Pašti, T., **Milanković, V.**, Tasić, T., Pašti, I., Porobić-Katnić, S., & Marinović-Cincović, M. (2024). Towards greener water remediation: Ca-impregnated pyro-hydrochar of spent mushroom substrate for enhanced adsorption of acridine red and methylene blue. Journal of Water Process Engineering, 60, 105204–105204. https://doi.org/10.1016/j.jwpe.2024.105204

2.2. Articles in leading international journals of category M21

1. Lazarević-Pašti, T., Tasić, T., **Milanković, V.**, & Potkonjak, N. I. (2023). Molecularly Imprinted Plasmonic-Based Sensors for Environmental Contaminants—Current State and Future Perspectives. Chemosensors, 11(1), 35–35. https://doi.org/10.3390/chemosensors11010035
2. Anićijević, V. J., Tasić, T., **Milanković, V.**, Breitenbach, S., Unterweger, C., Fürst, C., Bajuk-Bogdanović, D., Pašti, I. A., & Lazarević-Pašti, T. (2023). How Well Do Our Adsorbents Actually Perform?—The Case of Dimethoate Removal Using Viscose Fiber-Derived Carbons. International Journal of Environmental Research and Public Health, 20(5), 4553–4553. https://doi.org/10.3390/ijerph20054553

1. **Milanković, V.**, Tasić, T., Pejčić, M., Pašti, I., & Lazarević-Pašti, T. (2023). Spent Coffee Grounds as an Adsorbent for Malathion and Chlorpyrifos—Kinetics, Thermodynamics, and Eco-Neurotoxicity. Foods, 12(12), 2397–2397. https://doi.org/10.3390/foods12122397
2. Tasić, T., **Milanković, V.**, Batalović, K., Breitenbach, S., Unterweger, C., Fürst, C., Pašti, I., & Lazarević-Pašti, T. (2023). Application of Viscose-Based Porous Carbon Fibers in Food Processing—Malathion and Chlorpyrifos Removal. Foods, 12(12), 2362–2362. https://doi.org/10.3390/foods12122362
3. **Milanković, V.**, Tasić, T., Leskovac, A., Petrović, S., Mitić, M., Lazarević-Pašti, T., Novković, M., & Potkonjak, N. (2024). Metals on the Menu—Analyzing the Presence, Importance, and Consequences. Foods, 13(12), 1890–1890. https://doi.org/10.3390/foods13121890

2.3. Articles in an international journal of category M22

1. Lazarević-Pašti, T., Jocić, A., **Milanković, V.**, Tasić, T., Batalović, K., Breitenbach, S., Unterweger, C., Fuerst, C., & Pašti, I. (2023). Investigating the Adsorption Kinetics of Dimethoate, Malathion and Chlorpyrifos on Cellulose-Derived Activated Carbons: Understanding the Influence of Physicochemical Properties. C-Journal of Carbon Research, 9(4), 103–103. https://doi.org/10.3390/c9040103
2. Tasić, T., **Milanković, V.**, Unterweger, C., Furst, C., Breitenbach, S., Pašti, I., & Lazarević-Pašti, T. (2024). Highly Porous Cellulose-Based Carbon Fibers as Effective Adsorbents for Chlorpyrifos Removal: Insights and Applications. C, 10(3), 58–58. https://doi.org/10.3390/c10030058

3. Proceedings of international scientific conferences (M30)

3.1. Papers presented at internationally significant conferences published as a whole – M33

1. **Milanković, V.**, Breitenbach, S., Unterweger, C., Fürst, C., & Lazarević-Pašti, T. (2021). Viscose-Based Activated Carbon Material for Chlorpyrifos Remediation. 7th Workshop Specific Methods for Food Safety and Quality. Belgrade : Vinča Institute of Nuclear Sciences - National Institute of the Republic of Serbia.
2. Anićijević, V. J., Kokanov, K., Tasić, T., **Milanković, V.**, & Lazarević-Pašti, T. (2022). Waste-derived carbon material for malathion adsorption. 10th International Scientific Conference on Defensive Technologies - OTEH 2022. Belgrade : Military Technical Institute.
3. **Milanković, V.,** Tasić, T., Mitrović, S., Brković, S., Perović, I., & Lazarević-Pašti, T. (2022). Spent Coffee Grounds as an Adsorbent for Malathion and Malaoxon. Physical Chemistry 2022 - 16th International Conference on Fundamental and Applied Aspects of Physical Chemistry : Proceedings.
4. Tasić, T., **Milanković, V.**, Kokunešoski, M., Šaponjić, A., Valenta Šobot, A., Grce, A., & Lazarević-Pašti, T. (2022). Wood-Waste-Derived Activated Porous Carbon Material for Pesticide Removal From Water. PHYSICAL CHEMISTRY 2022 : 16th International Conference on Fundamental and Applied Aspects of Physical Chemistry : Book of Abstracts. Belgrade : Society of Physical Chemists of Serbia.
5. Kokanov, K., Tasić, T., **Milanković, V**., Potkonjak, N., & Lazarević-Pašti, T. (2022). Malathion Remediation in Water by Biowaste-Based Carbon Material. 16th International Conference on Fundamental and Applied Aspects of Physical Chemistry.

6. **Milanković, V**., Tasić, T., Brković, S., & Lazarević-Pašti, T. (2023). Remediation of Organophosphorous Pesticides Using Spent Coffee Grounds – Kinetics and Neurotoxicity. 1st International EUROSA Conference : Proceedings. Novi Sad : University of Novi Sad, Faculty of Technical Sciences.
7. Tasić, T., **Milanković, V.**, Breitenbach, S., Unterweger, C., Furst, C., Pašti, I., & Lazarević-Pašti, T. (2023). Kinetics of malathion removal using carbon material derived from viscose fibers. 1st International EUROSA Conference : Proceedings. Novi Sad : University of Novi Sad, Faculty of Technical Sciences.

3.2. Paper presented at an internationally significant conference published as an abstract – M34

1. **Milanković, V.**, & Lazarević-Pašti, T. (2021). Carbon material derived from viscose as adsorbent for chlorpyrifos. Nineteenth Young Researchers Conference - Materials Science and Engineering. Belgrade : Institute of Technical Sciences of SASA.
2. **Milanković, V**., & Lazarević-Pašti, T. (2021). Biomass Carbon Material for Removal of Chlorpyrifos from Water Samples. 1st DIFENEW International Student Conference. Novi Sad : Faculty of Technical Sciences.
3. Tasić, T., **Milanković, V.,** Kokanov, K., & Lazarević-Pašti, T. (2022). Biowaste-based carbon material for wastewater treatment. 2nd DIFENEW International Student Conference - DISC2022. Novi Sad : Faculty of Technical Sciences.
4. **Milanković, V**., Tasić, T., Brković, S., & Lazarević-Pašti, T. (2023). Effect of temperature for chlorpyrifos adsorption onto carbon material derived from spent coffee grounds. DISC2023 : 3rd DIFENEW International Student Conference : Abstract Book. Novi Sad : Faculty of Technical Sciences.
5. Tasić, T., **Milanković, V.**, & Lazarević-Pašti, T. (2023). Cellulose-derived carbon materials: A study of isotherms in malathion removal. DISC2023 : 3rd International Student Conference : Abstract Book. Novi Sad : Faculty of Technical Sciences.
6. Tasić, T., **Milanković, V.**, & Lazarević-Pašti, T. (2023). Activated porous carbon materials derived from viscose fibers for chlorpyrifos removal from water. ISC 2023 : 8th International Student Conference on Technical Sciences : Book of Abstracts. University of Belgrade : Technical Faculty in Bor.
7. **Milanković, V**., Tasić, T., & Lazarević-Pašti, T. (2023). Removal of chlorpyrifos and malathion using spent coffee grounds – isotherm study. ISC 2023 : 8th International Student Conference on Technical Sciences : Book of Abstracts. University of Belgrade : Technical Faculty in Bor.
8. **Milanković, V**., Tasić, T., Brković, S., Pašti, I., & Lazarević-Pašti, T. (2023). The impact of thermal treatment on spent coffee grounds for chlorpyrifos removal from water. 21st Young Researchers' Conference Materials Sciences and Engineering : Program and the Book of Abstracts. Belgrade : Institute of Technical Sciences of SASA.
9. Tasić, T., **Milanković, V.**, Pašti, I., & Lazarević-Pašti, T. (2023). Applying carbon materials derived from cellulose for the removal of malathion and chlorpyrifos in food processing. 21st Young Researchers' Conference Materials Sciences and Engineering : Program and the Book of Abstracts. Belgrade : Institute of Technical Sciences of SASA.
10. **Milanković, V.**, Tasić, T., & Lazarević-Pašti, T. (2022). Non-Treated Biowaste Material as Adsorbent for Malathion. 2nd DIFENEW International Student Conference - DISC2022. Novi Sad : Faculty of Technical Sciences.

Изјава о ауторству

Име и презиме аутора: Ведран Миланковић

број индекса: 2021/0302

Изјављујем

да је докторска дисертација под насловом

„Нови угљенични материјали добијени термохемијском конверзијом биоотпада као адсорбенси за уклањање малатиона и хлорпирифоса из воде“

- резултат сопственог истраживачког рада,
- да предложена дисертација у целини ни у деловима није била предложена за добијање било које дипломе према студијским програмима других високошколских установа,
- да су резултати коректно наведени и
- да нисам кршио/ла ауторска права и користио интелектуалну својину других лица.

Потпис докторанда

У Београду, 04.07.2024. _____

Изјава о истоветности штампане и електронске верзије докторског рада

Име и презиме аутора: Ведран Миланковић

Број индекса: 2021/0302

Студијски програм: Физика хемија

Наслов рада: „Нови угљенични материјали добијени термохемијском конверзијом биоотпада као адсорбенси за уклањање малатиона и хлорпирифоса из воде“

Ментори: проф. др Игор Пашти, др Тамара Лазаревић-Пашти

Изјављујем да је штампана верзија мог докторског рада истоветна електронској верзији коју сам предао за објављивање на порталу **Дигиталног репозиторијума Универзитета у Београду.**

Дозвољавам да се објаве моји лични подаци везани за добијање академског звања доктора наука, као што су име и презиме, година и место рођења и датум одбране рада.

Ови лични подаци могу се објавити на мрежним страницама дигиталне библиотеке, у електронском каталогу и у публикацијама Универзитета у Београду.

Потпис докторанда

У Београду, 04.07.2024. _____

Изјава о коришћењу

Овлашћујем Универзитетску библиотеку „Светозар Марковић“ да у Дигитални репозиторијум Универзитета у Београду унесе моју докторску дисертацију под насловом:

„Нови угљенични материјали добијени термохемијском конверзијом биоотпада као адсорбенси за уклањање малатиона и хлорпирифоса из воде“

која је моје ауторско дело.

Дисертацију са свим прилозима предао сам у електронском формату погодном за трајно архивирање.

Моју докторску дисертацију похрањену у Дигитални репозиторијум Универзитета у Београду могу да користе сви који поштују одредбе садржане у одабраном типу лиценце Креативне заједнице (Creative Commons) за коју сам се одлучио.

1. Ауторство

2. Ауторство - некомерцијално

3. Ауторство – некомерцијално – без прераде

4. Ауторство – некомерцијално – делити под истим условима

5. Ауторство – без прераде

6. Ауторство – делити под истим условима

Потпис докторанда

У Београду, 04.07.2024. _____

1. Ауторство - Дозвољавате умножавање, дистрибуцију и јавно саопштавање дела, и прераде, ако се наведе име аутора на начин одређен од стране аутора или даваоца лиценце, чак и у комерцијалне сврхе. Ово је најслободнија од свих лиценци.

2. Ауторство – некомерцијално. Дозвољавате умножавање, дистрибуцију и јавно саопштавање дела, и прераде, ако се наведе име аутора на начин одређен од стране аутора или даваоца лиценце. Ова лиценца не дозвољава комерцијалну употребу дела.

3. Ауторство - некомерцијално – без прераде. Дозвољавате умножавање, дистрибуцију и јавно саопштавање дела, без промена, преобликовања или употребе дела у свом делу, ако се наведе име аутора на начин одређен од стране аутора или даваоца лиценце. Ова лиценца не дозвољава комерцијалну употребу дела. У односу на све остале лиценце, овом лиценцом се ограничава највећи обим права коришћења дела.

4. Ауторство - некомерцијално – делити под истим условима. Дозвољавате умножавање, дистрибуцију и јавно саопштавање дела, и прераде, ако се наведе име аутора на начин одређен од стране аутора или даваоца лиценце и ако се прерада дистрибуира под истом или сличном лиценцом. Ова лиценца не дозвољава комерцијалну употребу дела и прерада.

5. Ауторство – без прераде. Дозвољавате умножавање, дистрибуцију и јавно саопштавање дела, без промена, преобликовања или употребе дела у свом делу, ако се наведе име аутора на начин одређен од стране аутора или даваоца лиценце. Ова лиценца дозвољава комерцијалну употребу дела.

6. Ауторство - делити под истим условима. Дозвољавате умножавање, дистрибуцију и јавно саопштавање дела, и прераде, ако се наведе име аутора на начин одређен од стране аутора или даваоца лиценце и ако се прерада дистрибуира под истом или сличном лиценцом. Ова лиценца дозвољава комерцијалну употребу дела и прерада. Слична је софтверским лиценцама, односно лиценцама отвореног кода.